PEOPLES DEMOCRATIC REPUBLIC

OF ALGERIA

MINISTRY OF HIGHER EDUCATION AND SCIENTIFIC RESEARCH

UNIVERSITY SAAD DAHLEB BLIDA 1

INSTITUTE OF AERONAUTICS AND SPACE STUDIES

Aeronautical Construction Department

Graduation Project

to obtain the Master's degree in **Aeronautics**

Aeronautical Construction

Aircraft Propulsion

The Impact Of Control Surfaces On Transonic Flow Mechanism And Aerodynamic Performances

Presented by :

MIMOUNI LILYA

Guided by :

Dr. RENANE Rachid

Mme. MECHRI Yamina

IAES

2021 - 2022

REPUBLIQUE ALGERIENNE DEMOCRATIQUE ET POPULAIRE

MINISTERE DE L'ENSEIGNEMENT SUPERIEUR ET DE LA RECHERCHE SCIENTIFIQUE

UNIVERSITE SAAD DAHLEB BLIDA 1

INSTITUT D'AERONAUTIQUE ET DES ETUDES SPATIALES

Département de Construction Aeronautique

Projet de fin d'études

pour obtenir le diplôme de Master en **Aéronautique**

Spécialité : construction Aeronautique

Option : propultion Avion

L'impact des surfaces de contrôle sur le mécanisme d'écoulement transsonique et les performances aérodynamiques

Présenté par :

MIMOUNI LILYA

Dirigé par :

Dr. RENANE Rachid

Mme. MECHRI Yamina

IAES

2021 - 2022

ملخص

تعرض هذه الدراسة نتائج عمليات المحاكاة للنظام العابر للصوت للتدفقات القابلة للانضغاط على الجنيحات باستخدام نهج الحجم المحدود ، كما تم إجراؤه في البرنامج التجاري CFD FLUENT. يتم تحديد المجالات الحسابية عن طريق إنشاء شبكات منظمة وغير منظمة للعديد من الظواهر الفيزيائية التي توفرها المعلمات البناءة ، مثل ارتفاع الطبقة الأولى من الخلايا المجاورة للجدار ، جنبًا إلى جنب مع دراسة استقلالية نماذج الاضطراب والتحقق من صحتها ، بالإضافة إلى يتم استخدام مجال السوائل للتحقق من جودة وملاءمة هذه الشبكات لمحاكاة جميع الحالات.
تستخدم نماذج الاضطراب الثلاثة ، Spalart-Allmaras ، و k-، و k-SST للتنبؤ بسلوك التدفق (عدد Mach الحرج ، وموجة الصدمة ، ...) والخصائص الديناميكية الهوائية (Cl، Cd ، .. .) من NACA0012 التقليدية ، والجنيحات فوق الحرجة OAT15A و RAE2822 بدون أسطح تحكم ، ولفعالية أسطح التحكم في الطيران ، حالة الجنيح NACA0012مع الجنيح ، والجناح الجنيح OAT15A مع الجنيح في زوايا مختلفة من الانحراف ، والجنيح OAT15A مع spoiler عند $\delta_{sp} = 30°$ يتم محاكاة ومقارنة النتائج التجريبية المتاحة.يتم أيضًا التحقيق في تباين المعاملات الديناميكية الهوائية لعمليات المحاكاة ثلاثية الأبعاد لجناح ONERA M6 SWEPT WING ، وهو جناح من جناح انسيابي NACA0012 عند $\delta_A = 0°,10°,-10°$، لجناح OAT15A الجناح الجنيحي عند $\delta_A = 10°$.

الكلمات المفتاحية: موجة الصدمة، الطبقة الحدية,التدفق العابر لسرعة الصوت ، المرونة الحركية.

Résumé

Cette étude présente les résultats de simulations pour le régime transsonique des écoulements compressibles sur les profils aérodynamiques en utilisant l'approche du volume fini, tel que réalisé dans le logiciel commercial CFD FLUENT. Les domaines de calcul sont discrétisés en générant des maillages structurés et non structurés pour divers phénomènes physiques donnés par des paramètres constructifs, tels que la hauteur de la première couche de cellules pret de la paroi, avec une étude de sensibilté de maillage et de validation des modèles de turbulence, ainsi que le volume de control utilisé pour valider la qualité de ces maillages pour les simulations de tous les cas.

Trois modèles de turbulence, le Spalart-Allmaras, le $k-\varepsilon$, et le $k-\omega\ SST$ sont utilisés pour prédire le comportement de l'écoulement (nombre de Mach critique, onde de choc,...) et les propriétés aérodynamiques (Cl, Cd,...) du profil conventionnel NACA0012 conventionnel, et les profils supercritiques OAT15A et RAE2822 sans surface de control, et pour l'efficacité des ces suraces, le cas d'un profil aérodynamique NACA0012 avec aileron, et OAT15A avec aileron à différents angles de déflection, et le profil OAT15A avec Spoiler à $\delta_{sp} = 30°$ sont simulés et comparés aux résultats expérimentaux disponibles. L'influence de l'angle d'attaque variable par rapport à l'angle de déflection de l'aileron au profil aérodynamique OAT15A est indiquée.

La variation des coefficients aérodynamiques pour les simulations 3D est également étudiée pour l'aile ONERA M6, l'aile du profil aérodynamique NACA0012 à $\delta_A = 0°,\ -10°$, et l'aile de profil OAT15A à $\delta_A = 10°$.

Mots clés : Régime transsonique, Surfaces de contrôle du bord de fuite, Performances aérodynamiques, Modèles de turbulence.

Abstract

This study presents the results of simulations for the transonic regime of compressible flows over airfoils using the finite volume approach, as performed in the commercial software CFD FLUENT. Computational domains are discretized by generating structured and unstructured meshes for various physical phenomena given by constructive parameters, such as the height of the first layer of cells next to the wall, along with a study of independence and validation of turbulence models, as well as the fluid domain is utilized to validate the quality and suitability of these meshes for the simulations of all the cases.

Three turbulence models, the Spalart-Allmaras, the $k-\varepsilon$, and the $k-\omega\,SST$ models are used to predict the flow behavior (critical Mach number, shock wave,...) and aerodynamic properties (Cl, Cd,...) of conventional NACA0012, and supercritical airfoils OAT15A and RAE2822 without control surfaces, and for the effectiveness of the flight control surfaces, the case of a NACA0012 airfoil with aileron, and OAT15A airfoil with aileron at different angles of deflection, and OAT15A airfoil with the spoiler at $\delta_{sp} = 30°$ are simulated and compared to the available experimental results. The influence of varying angle of attack to specific angle of deflection of the aileron attached to OAT15A airfoil is provided.

The variation of the aerodynamic coefficients for 3D simulations is also investigated for the ONERA M6 SWEPT WING, A wing of NACA0012 airfoil at $\delta_A = 0°,\ -10°$, and for the Wing of OAT15A airfoil at $\delta_A = 10°$.

Keywords: Transonic regime, Trailing edge control surfaces, Aerodynamic performances, Turbulence Models.

Aknowldgment

The completion of this undertaking could not have been possible without the participation and assistance of so many people whose names may not all be enumerated. Their contributions are sincerely appreciated and gratefully acknowledged. However, I would like to take this opportunity to express my deep appreciation, particularly to my supervisors **Dr. RACHID RENANE** and **Dr. MECHRI YAMINA**, for their understanding spirit during our case presentation, their patience, and especially for their advice, availability, and kindness. May they find here the testimony of my deepest gratitude. Along with all hard-working and respected members of the jury, thank you for accepting to evaluate this work and for all the reviews. I would also like to thank all the teachers who contributed to my education over the years and for their endless support.

From the professor's efforts to both parents and siblings, classmates of Aircraft Propulsion, class of 2017/2022, and circle of friends who extended their support while working on this project. Above all, I am thankful to God for honoring me with his grace and guiding me on the right path, especially for the strength, courage, patience, wisdom, time, and guidance in the accomplishment of this Thesis.

THANK YOU!

Dedication

April the first 2015, was the day I lost the person that I wished he witnessed my graduation. On that day, a life was taken, but a determination and ambition to succeed were born inside of me to make my father MIMOUNI ATHEMANE proud, I promised myself that a bachelor's degree is not my last achievement. After nearly five years of studies in IAES Blida, I have to say " Learn as much as you can while you are young since life becomes too busy later". I still can remember my first day applying for IAES, with my mother beside me, nursing me with affection and love, for that reason my humble effort is wholeheartedly and proudly dedicated to those who inspire me, to my loved ones who never gave up on me to complete my Master's degree.

Father & Mother

My sisters SANAA, IKRAM, DALIDA, and My brother Mohammed Amine

The little angels, my nephews Abdel Rahmane, Louey, and Kinda

My best friends Aziez Maroua and Meriem, Hachemi Houda, and Zitouni Malika

Last but not least, I'd want to thank myself for surviving a life more closely adventure. Therefore, I would say that all of my experiences would ultimately become one part of my body, and they will make me stronger. At the same time, I could not have overcome all of my challenges without the constant support of my family and friends. Thank you so much for all of your continuous encouragement in both good and difficult times.

TABLES OF CONTENTS

ملخص 3

RESUME 3

ABSTRACT 4

AKNOWLDGMENT 5

DEDICATION 6

LIST OF TABLES 10

LIST OF FIGURES 11

NOMENCLATURE 16

ABBREVIATION 19

EQUATIONS 21

GENERAL INTRODUCTION 1

CHAPTER I : 5

I.1 Introduction 6

I.2 Explanation of transonic flow around a wing profile 6

I.3 Shock Boundary Layer Interaction SBLI in transonic flows 9

I.3.1. Turbulence characteristics 9

I.3.2. Boundary layer 12

I.3.2. Shock Boundary Layer Interaction 15

I.4 Flow Control 17

I.5 Control surfaces: 18

I.5.1. Historical perspective of control surfaces 18

I.5.2 Types of Control Surfaces: 19

I.6 Literature review 29

I.6.1. Wind tunnel studies 29

I.6.2. Flow control and transonic regime 32

CHAPTER II : 63
II.1 Fundamental equations of instantaneous compressible fluids 64
II.2 Reynolds-Averaged Navier-Stokes equations (RANS) 66
II.3 Turbulence Modeling 69
II.3.1 Introduction 69
II.3.2. Turbulence Models 70
II.4 Wall Treatments 75
II.4.1. Standard Wall Functions 75
II.4.2. Enhanced wall functions 79
II.5 Conclusion 80
CHAPTER III : 81
III.1 Introduction 82
III.2 CFD with ANSYS Fluent 83
III.2.1. Geometry 83
III.2.2. Meshing: 84
III.2.3. Setting up Solver: 87
III.2.4. Methods and Control 90
III.2.5. Calculation 92
III.3 Conclusion 94
CHAPTER IV : 98
IV.1 Computer system characteristics and presentation of Ansys workbench 99
IV.1.1. Ansys 2021 R2 99
IV.2 Convergence criterion for the solutions 100
IV.3 Numerical simulation on airfoils without control surface 101
IV.3.1. Fluid Domain Sensitivity 101
IV.3.2. Mesh Independence 103
IV.3.3. Turbulence Models Independence: 106
IV.4 Validation of 3D simulation case 113
IV.4.1. ONERA M6 Wing 113
IV.5 Numerical simulation on OAT15A Airfoil with Spoiler at 30° 118
IV.6 Comparative Numerical Studies 119
IV.6.1. NACA0012 Airfoil & OAT15A Airfoil without control surface: 119

IV.6.2. NACA0012 airfoil without control surface at an angle of attack 0° & 1.5° 121
IV.6.3. NACA0012 airfoil without control surface & NACA0012 Airfoil with Aileron at $\boldsymbol{\delta A = 0°}$ 121
IV.6.4. Aileron Deflection Effects On Airfoils 124
IV.6.5. Angle Of Attack Effect On OAT15A airfoil with Aileron at different deflection angles 126
IV.6.7. Flow description over OAT15A airfoil attached to Spoiler at $\boldsymbol{\delta Sp = 30°}$ ... 127
IV.7 Aspect Ratio Impact on Three different Wings 130
IV.7.1. Wing of NACA0012 airfoil 130
IV.7.2. Wing of OAT15A airfoil: 136
IV.7.3. ONERA M6 Wing: 138
IV.8 Conclusion: 139
CONCLUSION 140
APPENDEXES 144
REFERENCES 154

LIST OF TABLES

Table 1.Upstream flow parameters used in RANS simulations for the supercritical wing profile OAT15A [57]. 48
Table 2.RANS Turbulence Model Descriptions and Usage [85]....72
Table 3.Near-wall treatment in FLUENT (FLUENT, 2005a) [88] 77
Table 4.Solver parameters used in this study 94
Table 5.Characteristics of the used computer system....99
Table 6.The free-stream conditions for the three cases of RAE2822....101
Table 7.Details of the fluid domin used for the study around a RAE2822 airfoil..102
Table 8.The free-stream conditions for the three cases of NACA0012 104
Table 9.The effect of mesh refinement on lift and drag coefficients 105
Table 10.The conditions for the three cases of OAT15A airfoil 107
Table 11.The lift and drag coefficients on the OAT15A airfoil of the three cases computed with different turbulence models. 107
Table 12.The free-stream conditions for the three cases of RAE2822....109
Table 13.The aerodynamic coefficients of the numerical findings and the available experimental data....109
Table 14.The aerodynamic coefficients of the numerical findings for the chosen cases [102]....111
Table 15.ONERA M6 wing geometry. 114
Table 16.The free-stream conditions for ONERA M6 Wing....114
Table 17.Mesh metrics for the first and second grid around ONERA M6 wing ...114
Table 18.The lift and drag coefficients on the OAT15A airfoil attached to Spoiler at 30°computed with different turbulence models to compare with the experimental [76]. 118
Table 19.OAT15A Airfoil Cordinates. 150
Table 20.OAT15A Airfoil Cordinates. 151
Table 21.RAE2822 Airfoil Cordinates....152
Table 22.NACA0012 Airfoil Cordinates. 153

LIST OF FIGURES

Figure I-1 Mach Number and Flow Regimes [6] 6
Figure I-3 The appearance of shock waves on conventional vs. Supercritical airfoils [8] 7
Figure I-2 Transonic Flow around an airfoil and the appearance of shock wave **[7]** 7
Figure I-4 Schematic of the variation of drag coefficient for an airfoil as a function of freestream Mach number at subsonic and transonic speeds [9] 8
Figure I-5 Boundary layer over an airfoil surface [1] 12
Figure I-6 Schlieren photographs[1] [3] 14
Figure I-7 Different layers and flow regimes over an airfoil [4] 14
Figure I-8 Shock and BL separation on Classical vs. Supercritical airfoil operating near Mach 1 [10] 15
Figure I-9 Aircraft control surfaces and their functions [14] 19
Figure I-10 Aileron at different positions [15] 20
Figure I-11 Aircraft Elevator [16] 20
Figure I-12 McDonnell Douglas DC-10 Rudder [18] 21
Figure I-13 Secondary control surfaces [19] 21
Figure I-14 Speed Brakes on aircraft wing [21] 23
Figure I-15 The slot and slat on a wing profile [23] 23
Figure I-16 Leading-edge Droop & Krueger flaps [25] 24
Figure I-17 The different positions of Krueger flap [25] 25
Figure I-18 Types of the trailing edge flaps [14] 25
Figure I-19 Triple slotted flap [14] 26
Figure I-20 Types of Tabs [14] 27
Figure I-21 The pattern of airflow before and after vortex generators [14] 28
Figure I-22 Results are taken from Caldwell, Frank W., and Elisha Noel Fales. Wind tunnel studies [28]. 29
Figure I-23 John Stack, Langley Research Center scientist, was Presented the Collier Trophy in 1947, awarded for his conception of transonic research airplanes. His research contributed to the X-1 breaking the sound barrier on October 14, 1947. (NASA Photo No. LMAL 32
Figure I-26 Concept of crossflow separation control [49] 42

Figure I-27 OAT15A supercritical profile in the S3Ch transonic wind tunnel 43
Figure I-28 Variation of C_l with AoA for different Reynolds numbers for the airfoil without and with GF [52]. 44
Figure I-29 RAE2822 airfoil A)Pressure Variation across Normal Shock (M=0.8) B)Pressure Variation across Oblique Shock (M=1.2) [53]. 45
Figure I-30 Cp contour with shock formation [54].....46
Figure I-31 A) ..... RAE2822 Pressure Contour 47
Figure I-32 (a)Taylor's University subsonic wind tunnel (b) NACA0012 wing model (c) Mesh of the fluid domain [61]. 49
Figure I-33 (a) Pressure distribution with streamlines (b) Delta wing with attached sting [62]. 50
Figure I-34 Aerodynamic circuit sketch of the ETW facility [63]..... **Erreur ! Signet non défini.**
Figure I-35 Surface oil flow visualization for flow over the static VG placed at a skew angle of 27°. Flow is left-to-right. The primary flow features present on the surface are labeled. The measurement domain selected for SPIV measurement is also shown [79]. 60
Figure II-1 Near-wall treatment in FLUENT (FLUENT, 2005a) [88].....76
Figure III-1 ANSYS Fluent 21 R2 workbench steps.....83
Figure III-2 RAE2822 airfoil A) Unstructured mesh B) Structured mesh.....84
Figure III-3 ANSYS Fluent Launcher 2021 R2 87
Figure III-4 Setting Up The Solver 87
Figure III-5 Setting Up The Physics.....88
Figure III-6 Defining fluid and its properties.....88
Figure III-7 Defining solid and its properties 89
Figure III-8 « Pressure Far-Field » boundary condition 89
Figure III-9 « Wall » boundary condition. 90
Figure III-10 reference values.....90
Figure III-11 Simulation Methods and Control 91
Figure III-12 Report Definitions.....91
Figure III-13 Simulation Monitors and Convergence Conditions.....92
Figure III-14 Solution Initialization 92
Figure III-15 Run Calculation.....93
Figure IV-1 ANSYS 2021 R2 Workbench used for the study simulations.....99
Figure IV-2 Fluent residuals graph to check convergence 100
Figure IV-3 Pressure Coefficient Distribution over RAE2822 airfoil with different fluid domains for Case 1 in comparison with experimental measurements.....102
Figure IV-4 Mesh convergence analysis around the wing profile NACA0012 for Pressure Coefficient Distribution comparison with experimental mesurments **[102]** using K-w SST For A) Case1 B) Case2 C) Case3 104
Figure IV-5 Wall Y Plus values in function of poistion (x/c) 106
Figure IV-6 Pressure Coefficient Distribution Over OAT15A using Different Turbulence Models in comparison with experimental measurements [50] For A) Case1 B) Case 2 C) Case 3.....108

Figure IV-7 Pressure Coefficient Distribution Over RAE2822 using Different Turbulence Models in comparison with experimental results For A) Case1 [56] B) Case2 [104] C) Case3 [105].....110
Figure IV-8 Geometric layout of the ONERA M6 wing [106].....113
Figure IV-9 Fluent Orthogonal Quality mesh metrics spectrum [107].....115
Figure IV-10 Fluent Skewness mesh metrics spectrum [107].....115
Figure IV-11 Pressure Coefficient Distribution over Onera M6 Wing at 6 sections compared to experimental [106] for mesh independence study using the Spalart-allmaras turbulence model.....116
Figure IV-12 Pressure Coefficient Distribution over Onera M6 Wing sections using different turbulence models in comparison with experimental results [106].....117
Fillola (2006) **[76]** investigates experiments performed in the T2 tunnel of ONERA Toulouse on a supercritical airfoil OAT15A with spoilers deflected. It analyzes results at $Mach = 0.73$, $AOA = 1.5°$, and $\delta sp = 30°$, focusing on the recirculation zone behind the spoiler. The pressure curves seen behind the spoiler indicate a pressure plateau in this region. In this section, the independence of turbulence models is investigated and compared to the results published in reference **[76]** as shown in **Figure IV-13** 118
Figure IV-14 Pressure Coefficient Distribution over OAT15A Airfoil with the spoiler at an angle of deflection 30° using different turbulence models in comparison with experimental results of Fillola (2006) [76].....118
A comparison between NACA 0012 and OAT15A airfoils has been made, by comparing the pressure coefficient distribution and pressure contour at $Mach = 0.73$, $\propto = 1.5$, and $Re = 3.5 \times 106$ using 0.15m chord length, the results are given in **Figure IV-6** and **Figure IV-15** respectively.....119
Figure IV-16 Pressure Coefficient Distribution Over NACA0012 in comparison with that of OAT15A at M= 0.73, AOA= 1.5, and R_e= 3.5× 〖10〗^6.....119
Figure IV-17 Pressure Contour Over NACA0012 airfoil in comparison with that of OAT15A airfoil without control surface at M= 0.73, AOA= 1.5, and R_e= 3.5× 〖10〗^6.....120
In order to capture the supersonic pocket over the NACA0012 airfoil without a control surface in a transonic regime, Pressure contours were plotted over that airfoil at AOA of 0° and 1.5°as shown in **Figure IV-18**.....121
Figure IV-19 Pressure Contour Over NACA0012 without control surface at AOA of 0° and 1.5° under freestream conditions of M= 0.73 and R_e=3.5× 〖10〗^6.....121
Figure IV-20 Pressure Coefficient Distribution Over NACA0012 with aileron in comparison with experimental results [108] at M= 0.75, AOA= 5, and δ_A= 0°..122
Figure IV-21 A) Pressure Contour B) Mach Number Contour over NACA0012 Airfoil with aileron at δ_A= 0°, Mach = 0.75, ∝= 5.....122
Figure IV-22 Pressure Coefficient Distribution Over NACA0012 without aileron compared to that of NACA0012 with aileron at δ_A= 0°, M= 0.73, AOA= 1.5....123
Figure IV-23 Pressure Contour Over NACA0012 without aileron at M= 0.73, AOA= 1.5, and $Re = 3.5 \times 106$**.**.....124

Figure IV-24 Pressure Contour Over OAT15A with aileron at δ_A=-20 ,M= 0.73, AOA= 1.5, and R_e= 3.5×〖10〗^6. 124
Figure IV-24 Pressure Contour Over OAT15A with aileron at δ_A=+20 ,M= 0.73, AOA= 1.5, and R_e= 3.5×〖10〗^6. 125
Figure IV-25 Lift and Drag Coefficients variation over OAT15A airfoil with aileron in function of angle of deflection at M=0.73, and R_e= 3.5×〖10〗^6. 125
Figure IV-26 Lift and Drag Coefficients variation over OAT15A airfoil with aileron in function of angle of Attack at M= 0.73 and δ_A=(_-^+)3°, 〖δ〗_A=6°, 〖δ〗_A=20°.....126
Figure IV-27 Drag Polar at M= 0.73, diffirent angles of attack over OAT15A airfoil with aileron for δ_A=(_-^+)3°, 〖δ〗_A=6°, 〖δ〗_A=20°.....127
Figure IV-28 Pressure Contour over OAT15A Airfoil with Spoiler at δ_Sp= 30°, Mach = 0.73, ∝= 1.5, and R_e= 3.5×〖10〗^6 128
Figure IV-29 Mach number Contour over OAT15A Airfoil with Spoiler at δ_Sp= 30°, Mach = 0.73, ∝= 1.5, and R_e= 3.5×〖10〗^6.....128
Figure IV-30 Velocity Vectors over OAT15A Airfoil with Spoiler at $\delta Sp = 30°$**,** $Mach = 0.73$**,** $\propto = 1.5$**, and** $Re = 3.5 \times 106$**.** 129
The 3D wing studied has a NACA0012 profile and is equipped with an aileron at a deflection angle of zero under the parameters M=0.75 and AOA=5, the results of pressure coefficient distribution at those conditions are presented in Figure N and **Figure IV-31**.....130
Figure IV-32 Pressure Coefficient Distribution over the Wing of NACA0012 airfoil with aileron at 0%, 25%, and 50% of wing span using the Spalart-Almaras turbulence model at $\delta A = 0°$, M=0.75, and AOA=5°.....130
Figure IV-33 3D Illustration of Pressure Coefficient Distribution over the Wing of NACA0012 airfoil equipped with aileron of 0° deflection angle at 0%, 25%, and 50% of wing span using the Spalart-Almaras turbulence model at M=0.75 and AOA=5°.....131
Figure IV-34 Pressure Contour over the Wing of NACA0012 airfoil with aileron using the Spalart-Almaras turbulence model at $\delta A = 0°$**, M=0.75, and AOA=5°.** 131
Figure IV-35 Mach Number Contour over the Wing of NACA0012 airfoil with aileron at 25% and 50% of wing span using the Spalart-Almaras turbulence model at $\delta A = 0°$**, M=0.75, and AOA=5°.** 132
Figure IV-36 Pressure Contour over the Wing of NACA0012 airfoil with aileron using the Spalart-Almaras turbulence model at $\delta A = 0°$**, M=0.73, and AOA=1.5°.** 132
Figure IV-37 Pressure Coefficient Distribution over the Wing of NACA0012 airfoil with aileron at 0%, 25%, and 50% of wing span using the Spalart-Almaras turbulence model at $\delta A = 0°$**, M=0.73, and AOA=1.5°.**.....133
Figure IV-39 Mach Number Contour over the Wing of NACA0012 airfoil with aileron at 25% and 50% of wing span using the Spalart-Almaras turbulence model at $\delta A = 0°$**, M=0.73, and AOA=1.5°.** 134

Figure IV-38 Pressure Contour Over the Wing of NACA0012 airfoil with aileron at 25% and 50% of wing span using the Spalart-Almaras turbulence model at $\delta A = -10°$**, M=0.73, and AOA=1.5°.**.....134
Figure IV-40 Mach number Contour Over the Wing of NACA0012 airfoil with aileron at 0%, 25%, and 50% of wing span using the Spalart-Almaras turbulence model at δ_A= -10°, M=0.73, and AOA=1.5°. 135
Figure IV-41 2D and 3D Illustration of Pressure Coefficient Distribution over the Wing of OAT15A airfoil equipped with aileron 10° of deflection angle at 2 sections of wing span using the Spalart-Almaras turbulence model at M=0.73 and AOA=1.5°. 136
Figure IV-42 Pressure Contour Over the Wing of OAT15A airfoil with aileron at 2 sections of wing span using the Spalart-Almaras turbulence model at $\delta A = 10°$**, M=0.73, and AOA=1.5°** 137
Figure IV-43 Mach number Contour Over the Wing of OAT15A airfoil with aileron at 2 sections of wing span using the Spalart-Almaras turbulence model at $\delta A = 10°$**, M=0.73, and AOA=1.5°** 137
Figure IV-44 Pressure Coefficient Distribution over Onera M6 Wing at 6 sections using the Spalart-allmaras turbulence model. 138

Nomenclature

$\boldsymbol{R_e}$	Reynolds number	
$\boldsymbol{R_{ec}}$	Critical Reynolds number	
$\mathbf{M}$	Mach Number	
$\mathbf{M_{cr}}$	Critical Mach number	
$\mathbf{M}_\infty$	Freestream Mach Number	
$\boldsymbol{C_d}$	Drag Coefficient	
$\boldsymbol{C_l}$	Lift Coefficient	
$\boldsymbol{C_p}$	Pressure Coefficient	
$\boldsymbol{\tau_{ij}}$	Viscous stress tensor	
$\boldsymbol{\rho}$	The fluid density	$[\boldsymbol{K_g/m^3}]$
$\boldsymbol{u}$	The velocity	$[\boldsymbol{m/s}]$
$\mathbf{U}_\infty$	Freestream velocity	$[\boldsymbol{m/s}]$
$\mathbf{L}$	Characteristic length dimension	$[\boldsymbol{m}]$
$\boldsymbol{\mu}$	The fluid dynamic viscosity	$[\boldsymbol{K_g/m.s}]$
$\boldsymbol{\mu_0}$	The fluid dynamic viscosity at the reference temperature $\boldsymbol{T_0}$	$[\boldsymbol{K_g/m.s}]$
$\boldsymbol{\nu}$	Kinematic viscosity	$[\boldsymbol{m^2/s}]$
$\boldsymbol{\delta}$	Boundary layer thickness	$[\boldsymbol{m}]$
$\mathbf{a}$	Sound velocity	$[\boldsymbol{m/s}]$
$\mathbf{P}$	Pressure	$[\boldsymbol{K_g/m.s}]$
$\mathbf{T}$	Tempeture	$[\boldsymbol{K}]$
$\boldsymbol{t}$	Time	$[\boldsymbol{s}]$
$\boldsymbol{r}$	The particular ideal gas constant	$[\boldsymbol{J/mol.k}]$
$\boldsymbol{\alpha}$	Angle Of Attack	Deg°
$\boldsymbol{\beta}$	Deflection Angle	Deg°

γ	Inclination Angle	Deg°
c	Profile Chord	$[m]$
u_j	j component of the velocity vector	
δ_{ij}	The the Kronecker tensor	
τ_{ij}	The viscous stress tensor	
x_j	Cartesian coordinates in the **j** direction	
q_j	The heat flow in the **j** direction	
E	The total energy per unit mass	
γ	The particular ideal gas constant	
C_p	The specific heats at constant pressure	
C_v	The specific heats at constant volume	
K	The thermal conductivity	
P_r	Prandtl number	
e	Internal energy	
h	Enthalpy	
$-\overline{\rho}\overline{u_i'' u_j''}$	Reynolds stress	
μ_t	The turbulent viscosity	
k	The turbulent energy	
Γ_t	The turbulent diffusivity	
Pr_t	The turbulent Prandtl number	
ε	The turbulent energy dissipation ratio	
G_k	The generation of kinetic energy as a result of the velocity gradient	
G_b	The production of **k** as a result of volume force detachment	
Y_M	The contribution of fluctuating expansion in the compressible turbulence for (ε)	

S_k, S_ε The source terms

Pr_k, Pr_ε Prandtl's turbulent number for k and ε

S_{ij} The strain tensor

S The medium tensor module of the stress ratio

τ_ω The shear stress at the wall

E, κ Von Karman constants

$\tilde{u}_p$ The average velocity of the fluid at point **P** located at a distance y_p from the wall

k_p The turbulent kinetic energy at point **P**

δ_A Aileron angle of deflection

δ_{Sp} Spoiler angle of deflection

ABBREVIATION

SBLI	Shock Boundary Layer Interaction.
SWBLI	Shock Wave/Boundary-Layer Interactions
ATAT	Advanced Technology Airfoil Test.
TTBW	Transonic Truss-Braced Wing.
VCCTEF	Variable Camber Continuous Trailing Edge Flap
NACA	National Advisory Committee for Aeronautics.
ONERA	Office National d'Etudes et de Recherches Aérospatiales.
AOA	Angle Of Attack.
LE	Leading Edge.
TE	Trailing Edge.
2D/3D	Two/Three Dimensional Space.
CFJ Airfoil	Co-Flow Jet Airfoil.
PIV	Particle Image Velocimetry.
RMS	Root Mean Square.
AFC	Active Flow Control.
ACT	Active Control Technology.
VG	Vortex Generators.
DVG	Dynamic Vortex Generators.
SVG	Static Vortex Generators.
IBV	Inboard Vortex.
MBV	Mid-Vortex.
FRAP	Fast Response Aerodynamic Pressure Probe.
GF	Gurney Flap.
V/STOL	Vertical Take-Off and Landing aircraft.
PANS	Partially Averaged Navier-Stokes.

FANSE	Favre- Averaged Navier-Stokes Equations
URANS	Unsteady Reynolds Averaged Navier-Stokes.
RANS	Reynolds-Averaged Navier-Stokes Equations.
CFD	Computational Fluid Dynamics.
DNS	Direct Numerical Simulation
LES	Large Eddy Simulation

EQUATIONS

Equation I.1 The ratio of flow velocity **V** to sound velocity **a.**

Equation I.2 Reynolds number as a function of fhe fluid dynamic viscosity $\boldsymbol{\mu}$**.**

Equation I.3 Reynolds number as a function of the kinematic viscosity $\boldsymbol{\nu}$**.**

Equation I.4 Reynolds number based on the boundary layer thickness$\boldsymbol{\delta}$**.**

Equation II.1 The continuity equation.

Equation II.1 The continuity equation.

Equation II.2 The conservation of momentum equation.

Equation II.3 The conservation of energy equation.

Equation II.4 The total energy per unit mass.

Equation II.5 Equation of state of an ideal gas.

Equation II.6 The viscous stress tensor $\boldsymbol{\tau_{ij}}$ formula.

Equation II.7 The heat flow $\boldsymbol{q_j}$ per unit area as a function of the temperature formula.

Equation II.8 Prandtl number.

Equation II.9 The heat flow as a function of Prandtl number.

Equation II.10 Sutherland law of the dynamic viscosity for the temperature range studied.

Equation II.11 Instantaneous quantity of flow.

Equation II.12 Components of averaged velocities in turbulent regime.

Equation II.13 The quantities of the fluid according to the derivation of Favre-averaged Navier-Stokes equations.

Equation II.14 The continuity equation with the averaged components.

Equation II.15 The momentum equation with the averaged components.

Equation II.16 The Reynolds stress formula.

Equation II.17 The turbulent energy formula.

Equation II.18 Favre-averaged Navier-Stokes equations.

Equation II.19 The energy equation with the averaged and fluctuating components.

Equation II.20 The fluctuating enthalpy formula.

Equation II.21 The turbulent energy dissipation ratio for the $\boldsymbol{k-\varepsilon}$ model.

Equation II.22 The turbulent energy dissipation ratio expression as in the Balwin-Lomax model.

Equation II.23 The averaged state equation.

Equation II.24 The transport equation as a function of $\boldsymbol{G_k}$, $\boldsymbol{G_b}$, $\boldsymbol{Y_M}$, $\boldsymbol{S_k}$.

Equation II.25 The transport equation as a function of $\boldsymbol{C_{\varepsilon 1}}, \boldsymbol{C_{\varepsilon 2}}, \boldsymbol{C_{\varepsilon 3}}$, $\boldsymbol{G_b}$, $\boldsymbol{S_\varepsilon}$.

Equation II.26 The turbulent viscosity formula.

Equation II.27 The generation of turbulent kinetic energy expression $\boldsymbol{G_k}$.

Equation II.28 The generation of turbulent kinetic energy $\boldsymbol{G_k}$ expression using the Boussinesq hypothesis.

Equation II.29 The medium tensor module of the stress ratio **S** as a function of the strain tensor $\boldsymbol{S_{ij}}$.

Equation II.30 The strain tensor formula $\boldsymbol{S_{ij}}$.

Equation II.31 The generation of turbulence due to pressure forces expression.

Equation II.32 The generation of turbulence due to pressure forces in an ideal gas case.

Equation II.33 The formula of $\boldsymbol{Y_M}$ dilation dissipation.

Equation II.34 The formula of Mach number and the speed of sound According to **S. Sarkar et al.**.

Equation II.35 The law of the wall for the temperature.

Equation II.36 The law of the wall for the temperature based on linear and Logarithmic law

Equation II.37 The production of turbulent kinetic energy according to Launder and Spalding.

Equation II.38 The dissipation rate according to Launder and Spalding.

Equation II.39 The Y plus expression.

Equation II.40 The velocity profile expression.

Equation II.41 The velocity profile in the viscous sublayer.

Equation II.42 The logarithmic velocity profile in the outer layer.

Equation II.43 Boundry condition for calculated k equation.

Equation II.44 $\boldsymbol{u^*}$ formula based on $\boldsymbol{y^*}$condition.

Equation II.45 $\boldsymbol{u^*}$ and $\boldsymbol{y^*}$final expressions as a function of average velocity at point P.

Equation II.46 Reynolds number dependent on **y** ($\boldsymbol{Re_y}$) expression.

Equation III.1 The static pressure formula.

Equation III.2 Upstream air temperature.

General Introduction

Over the course of human history, scientists have learned to harness the power of the atmosphere to travel long distances and accomplish remarkable feats, and aerodynamics has made a significant contribution to the construction of the airplanes we use today to achieve more targets. For this reason, aerodynamic is one of the most important crucial branches of aeronautic engineering since it is the scientific discipline that enables us to comprehend flow characteristics and examine their motion around a moving body through space, allowing for improvements in flying performance by predicting the forces and moments exerted by fluid/solid contact.

In the world of aerodynamics, the body of an aircraft is made up of many different parts, each performing a specific function, and the wing has the greatest effectiveness and impact at transonic and supersonic flight speeds, where the wing configuration has a major impact on aerodynamic performance and how well the aircraft handles air pressure during a flight, and it's the most concerning part of the study since it's subject to two aerodynamic forces: the drag force of the air, known as drag, and the supporting force, known as lift. For these forces to be generated, the flow must remain in contact with the wing, which is the case at small angles of attack. The boundary layer breaks when the critical angle of incidence reaches or exceeds the viscosity of the air, resulting in a severe loss of lift. Also known as wing stall, it is affected by the angle of incidence.

During flight, the aircraft moves through a region where the air molecules are distributed around the aircraft, when the aircraft flies by at low speed, it is observed that the density of the air remains constant. However, at higher speeds, close to and faster than the speed of sound, the behaviour of air becomes most complicated, and some of the aircraft's energy goes into compressing the air and locally changing its density and its other properties. The density change is nearly equal to the velocity change, and compressibility effects cannot be ignored. This compressibility effect changes the amount of resulting force on the aircraft since aerodynamic force depends on air density.

As speed increases near and above the speed of sound, at a Mach number slightly higher than the critical Mach and at a certain value, a shock wave appears at the front of the leading edge and affects both the lift and drag of the aircraft.

In order to solve this problem, the engineers were interested in flow control since it serves industrial objectives such as improving flight safety, and maneuverability, increasing the range of movement and reducing fuel consumption. Therefore, they carefully focused on the shape and size of the wing, to locate the position of the occurrence of the shock wave on the profile, to avoid the sudden loss of lift, and achieve a balance between lift and drag produced, capable of operating at higher speeds.

The operation and control of an aircraft are provided by wing controls known as spoilers and ailerons during multiple phases of flight. These control surfaces are moveable surfaces that allow developers to modify the airflow around the profile. Therefore, to accurately predict the aerodynamic behavior of an aircraft, aerodynamic models capable of characterizing the influence of various deflections of moving surfaces on the overall forces of the aircraft are required. However, the variety of aerodynamic phenomena to be modeled presents a real challenge for aerodynamicists who can no longer rely on wind tunnel tests to answer the many questions involved in the development of an aircraft, then Computational Fluid Dynamics, or **CFD** for short, began in the early 1970s. At that time it became an abbreviation for the combination of physics and numerical mathematics, which was closely associated with the development of computer technology. This progress over the last few decades enabled the validations of a mathematical model that allowed a reliable approach for more complicated cases, and various numerical approaches made it possible to identify the effects of moving surface deflections using more effective calculation codes such as FLUENT, XFOIL, and ANSYS.STARCCM+ etc..

The simulation of transonic flows based on the solution of the non-linear potential equation was among the first applications of CFD approaches. In the early 1980s, it became possible to solve two-dimensional (2-D) and then three-dimensional (3-D) Euler equations. Due to the obvious rapidly increasing speed of

supercomputers and the development of a variety of numerical acceleration techniques such as multigrid, it was possible to simulate inviscid flows through complete airplane configurations or within turbomachines.

In the mid-1980s, the focus shifted to much more complex simulations of viscous flows based on the Navier-Stokes equations. Simultaneously, several turbulence models with different degrees of numerical accuracy were developed, with Direct Numerical Simulation **(DNS)** and Large Eddy Simulation **(LES)** leading the list in turbulence modeling.

- **Work strategy**

This work consists of five chapters. The first chapter contains a bibliographical synthesis of movable control surface efficiency and a general overview of the physics and behaviour of transonic flows around a wing. The functioning and application of aircraft ailerons and spoilers, including the main physical phenomena involved, are discussed and supported by a comprehensive review of previous studies on the subject.

In the second chapter, we will apply a set of equations and mathematical modeling of the topic under study, specifically the Averaged-Navier stocks equations based on the Reynolds decomposition (RANS). These equations will be supplemented with the problem's initial conditions.

The third chapter goes into great depth on the presentation of the computational code, containing a brief explanation of the **CFD** which stands for computational fluid dynamics, which is used for the numerical resolution, followed by the inputs and parameters of our simulation.

The last two chapters are devoted to the validation and presentation of numerical results from the simulation of transonic flow around a classic profile NACA0012, supercritical OAT15A, and RAE2822. A NACA0012 with aileron, then around a 3D wing having NACA0012 as the base profile.

Finally, the work is completed with a general conclusion indicating the subject's interest and some future perspectives are suggested.

CHAPTER

THEORETICAL BACKGROUND & LITERATURE REVIEW

I

CHAPTER CONTENT

I.1 General information on flows around profiles…….

I.2 Explanation of transonic flow around a wing profile……....

I.3 SBLI in transonic flows……..

I.4 Flow control…….

I.5 Control surfaces……..

I.6 Literature review…….

OUTLINE

This chapter investigates the physics and behavior of transonic flow over an airfoil and a wing. It is one of the most difficult flows that aircraft designers and engineers have to deal with. This section of the research also provides background on the design and use of control surfaces, which are used to adjust the amount of air flowing over the wing. It also contains a literature review, which provides a description, summary, and assessment of important publications and other numerical results obtained on this issue, which is supported by scientific journal articles, books, reports, Web sites, etc.

I.1 Introduction

The differentiation between various aerodynamic flows is mostly dependent on the Mach number, which is a non-dimensional portion that indicates the ratio of flow velocity **V** to sound velocity **a**.

$$\mathbf{M} = \frac{\mathbf{V}}{\mathbf{a}} \qquad \text{I.1}$$

Therefore, by employing the Mach number, we can not only measure the flow rate but also reveal a lot about its physical properties. The Mach number has also been used to distinguish between the compressible and incompressible fluid flow, as an approximation that simplifies the understanding of its behaviour. For example, gas moving at a Mach number less than three-tenths may be considered incompressible or of constant density.

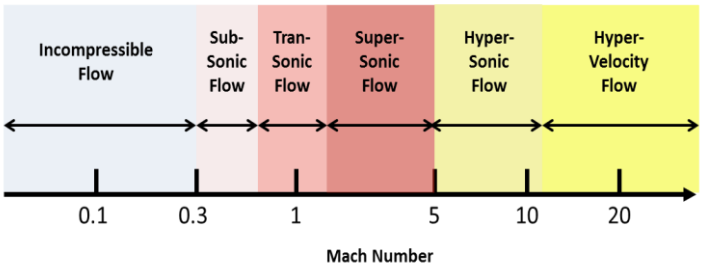

Figure 0-1 Mach Number and Flow Regimes [6]

When the Mach number of a flow is changed, its physical composition changes dramatically, allowing us to classify the following flight regimes:

- **Subsonic if** $M < 1$
- **Transonic if** $0,7 < M < 1,2$
- **Sonic if** $\mathbf{M} = 1$
- **Supersonic if** $1 < M < 5$
- **Hypersonic if** $M > 5$

I.2 Explanation of transonic flow around a wing profile

The transonic regime, as stated in the previous overview, has infinite upstream Mach values in the range of **0.7** to **1.2**, and the most common description of this flow is the presence of a supersonic "pocket" fully inserted into a subsonic flow.

For a more specific definition, the boundaries of the transonic regime are the interval between the critical Mach number when the supersonic regime appears somewhere on the surface for the first time and the highest Mach number when the flow is mainly supersonic. Between these two intervals, the flow is a combination of subsonic and supersonic regimes.

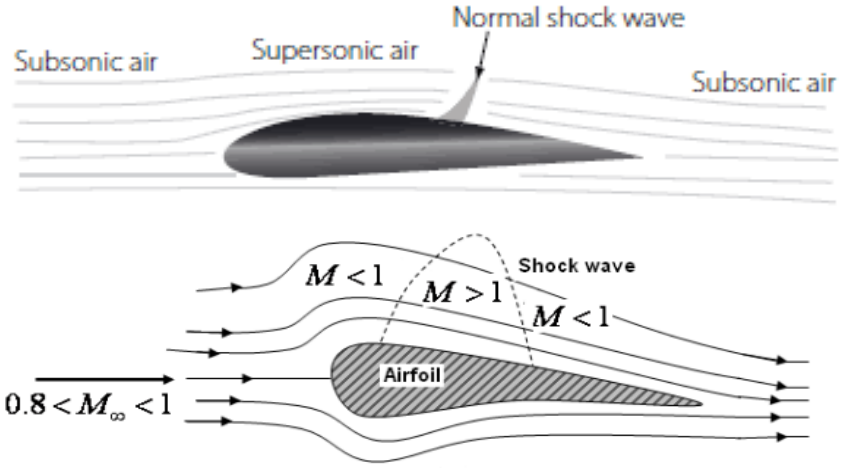

Figure 0-3 Transonic Flow around an airfoil and the appearance of shock wave **[7]**

The subsonic flow over the airfoil occurs when the drag coefficient of an airfoil as a function of Mach number remains relatively constant over a wide range of Mach numbers, the entire flow is still subsonic, but as the freestream Mach number increases, so does the flow Mach number on the top surface of the airfoil, until the sonic flow is first achieved somewhere on the airfoil surface at the profile's maximum thickness, where the local velocity equals the speed of sound and the freestream Mach number takes a critical value, denoted by M_{cr} in **Fig.I.2**

As the M_{∞} value is increased above the Critical Mach numberM_{cr}, a limited zone of supersonic flow forms on the top and possibly bottom surfaces of the airfoil (This relates to point b in **Fig.I.2).**

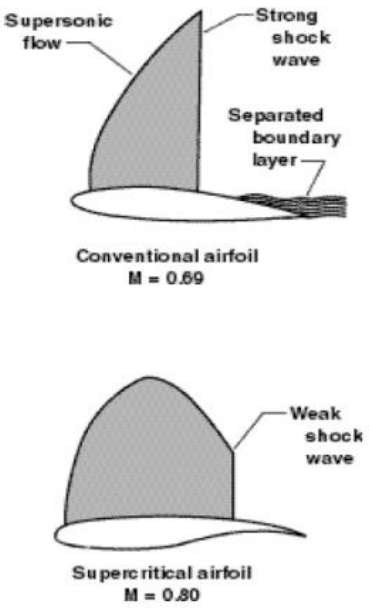

Figure 0-2 The appearance of shock waves on conventional vs. Supercritical airfoils [8]

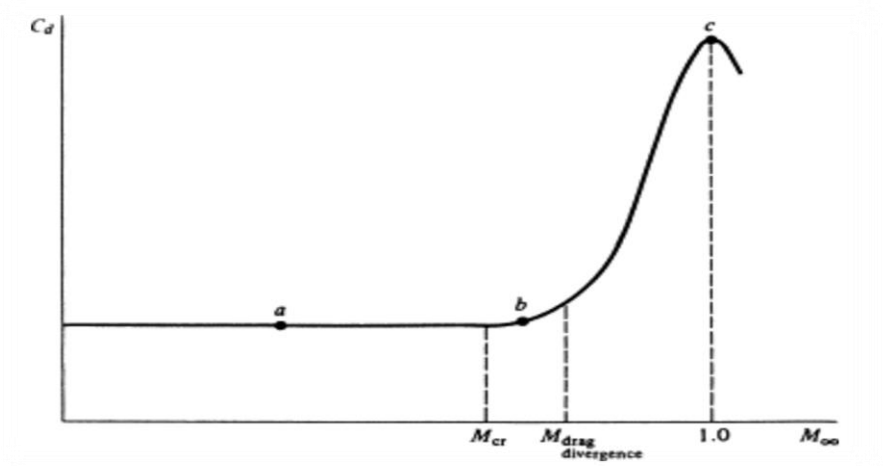

Figure 0-4 Schematic of the variation of drag coefficient for an airfoil as a function of freestream Mach number at subsonic and transonic speeds [9]

This supersonic pocket is bounded by a sonic line, and a shock wave closes it, creating a destructive wave drag. As the freestream Mach number continues to increase, the sonic line approaches the leading edge and the shock wave moves back towards the trailing edge.

The drag coefficient rapidly increases, immediately after the production of a shockwave that affects both the lift and drag of the aircraft, the freestream Mach number at which this major drag increase starts, is defined as the drag-divergence Mach number, which is also presented in **Fig.I.4**

The major increase in drag near a freestream Mach number of 1 was once thought to be so severe that airplanes would never fly faster than sound. This myth of the “sound barrier” was supported by theoretical results, which shows $\boldsymbol{C_d}$ going to infinity as $\boldsymbol{M_\infty}$ goes to 1.

However, the linear theory that produces this result is not valid near Mach 1.

In reality, the drag coefficient will peak at some finite value around Mach 1, as long as the airplane has excess thrust from the engines to overcome this peak drag, the aircraft can easily fly into the supersonic regime **[9]**.

I.3 Shock Boundary Layer Interaction SBLI in transonic flows

I.3.1. Turbulence characteristics

One of the very first things we learn in fluid mechanics is the difference between the laminar and turbulent flow. And for good reason, these two flow regimes behave in very different ways. A laminar regime that is even flow, characterized by its smoothness and the motion is horizontal with a minimal amount of mixing between layers. As we increase the flow velocity we begin to see some bursts of random motion.

This is the start of the transition between the laminar and turbulent regimes, if we continue increasing the velocity we end up with a fully turbulent flow that contains swirling regions called eddies.

The chaotic motion and eddies result in significant mixing of the fluid, If we record the velocity at a single point in steady laminar flow, there will be no random velocity fluctuations, and that is why this flow type is fairly easy to analyse.

For turbulent flow regime, it is much more complicated because of its chaotic nature, analysis of turbulent flow is very complex, so we think of the velocity as being made up of a time-averaged component, and a fluctuating component. The larger the fluctuating component, the more turbulent the flow.

Since the laminar and turbulent flows are so different and need to be analysed in different ways, the prediction of which flow regime is likely to be produced by a particular set of flow conditions is needed and we can do this using a parameter that was defined by Osborne Reynolds in 1883.

Reynolds performed extensive testing to identify the parameters which affect the flow regime and came up with this non-dimensional parameter, which we call Reynolds number. It is very useful because it compares non-linear convection terms to viscous dissipation terms to predict if flow will be laminar or turbulent using the relative importance of the inertial forces and the viscous forces.

$$\boldsymbol{R}_{\mathrm{e}} = \frac{\boldsymbol{\rho u L}}{\boldsymbol{\mu}} = \frac{\boldsymbol{INERTIAL\ FORCES}}{\boldsymbol{VISCOUS\ FORCES}} \qquad \textbf{I.2}$$

- Where:
  - $\boldsymbol{\rho}$ The fluid density,
  - $\boldsymbol{u}$ The velocity,
  - **L** Characteristic length dimension,
  - $\boldsymbol{\mu}$ The fluid dynamic viscosity.

- The equation is sometimes written as a function of the kinematic viscosity $\boldsymbol{\nu}$ instead, which is just the dynamic viscosity divided by the fluid density.

$$\boldsymbol{R}_{\mathrm{e}} = \frac{\boldsymbol{uL}}{\boldsymbol{\nu}} \qquad \textbf{I.3}$$

- The characteristic length **L** depend on the analysed type of flow, for example:
  - A flow past a cylinder it will be the cylinder diameter.
  - A flow past an aerofoil it will be the chord length.
  - A flow through a pipe it will be the pipe diameter.

Inertial forces are related to the momentum of the fluid, and so are essentially the forces that cause the fluid to move and the viscous forces are the frictional shear forces that develop between layers of the fluid due to its viscosity. If viscous forces dominate, flow is more likely to be laminar because the frictional force within the fluid will dampen out any initial turbulent disturbances and random motion.

That is how it is used to predict flow regimes. If inertial forces dominate, flow is more likely to be turbulent. But if viscous forces dominate, it's more likely to be laminar.

As the Reynolds number increases, a change in flow topology is observed which corresponds to the transition zone, so smaller values of the Reynolds number indicate that flow will be laminar. The critical Reynolds number at which the transition to the turbulent regime occurs takes different values depending on the type of flow we are dealing with.

- For a flow through a pipe, the transitional flow range is between 2000 and 4000, and under very controlled conditions in a lab, the onset of turbulence can be delayed until much larger Reynolds numbers.
- For a flow between infinite planes, the critical Reynolds number is $\boldsymbol{R_{ec} = 1000}$.
- For a boundary layer above a flat plate, we use the Reynolds number based on the boundary layer thickness$\boldsymbol{\delta}$. The boundary layer expands for $\boldsymbol{R_e < 520}$

$$\boldsymbol{R_e = \frac{U\delta}{\nu}} \qquad \textbf{I.3}$$

- Based on Blasius profile in $\boldsymbol{\delta = x\sqrt{x}}$ There is a transition zone for $\boldsymbol{< R_{e\delta} < 2000}$; in which the unstable waves in a viscous boundary layer constitute the first stage resulting from the linear instability of a laminar flow that leads to the Laminar/Turbulent transition. The calculations of Tollmien and Schlichting showed that unstable waves appear when the Reynolds number is high enough resulting in the development and deformation of the wave into three-dimensional vortices until it creates a turbulent spot.

- **The following features identify turbulence:**

✓ Unpredictable, and highly sensitive to boundary conditions.
✓ Flow has a variety of spatial scales (vortex sizes).
✓ The spatial distribution of fluctuations is disordered, chaotic, and unstable.
✓ Very wide range of wavelengths: vortices of varying diameters are found (for an aircraft: from a few microns to a few hundred meters, for atmospheric turbulence: from a few millimeters to a few thousand kilometers).
✓ Noise: turbulent flows are loud due to acoustic sources caused by pressure variations in the fluid, which can be uncomfortable in some cases.

- **Turbulence can have both beneficial and harmful effects:**

✓ **Advantages:** Increasing the mixture improves combustion by reducing temperature.
✓ **Disadvantages:** The effects of boundary layer separation, frequently has a significant impact on aerodynamic performance and aircraft manoeuvrability.

➢ **The following physical phenomena are damaging to aerodynamics:**

- ✓ Large disturbances in pressure distributions resulting an increase in drag,
- ✓ Stall appearance and strong stress on the profile,
- ✓ A considerable decrease in the lift,
- ✓ Increased noise pollution due to vorticity in the separated zone interacting with the wall.

I.3.2. Boundary layer

I.3.2.1. Conception

The conception of the boundary layer has improved the understanding of viscous flows, allowing the precise calculation of the forces and flow around aerodynamic bodies. When a fluid flows around an aircraft wing, a boundary layer forms on the wing's upper and lower surfaces. Near the leading edge, the limit layer is laminar for low viscosity fluid flows where the non-slip condition is not satisfied, and it is, the speeds on the wall are not null but have finite values. The viscosity must be considered to satisfy the non-slip condition. This enables the speed to shift from a finite value near the wall to a zero value right on the wall.For high Reynolds numbers, this transition happens in a thin layer along the wall, which was named the friction layer or boundary layer by the German scientist Ludwig Prandtl in 1904.

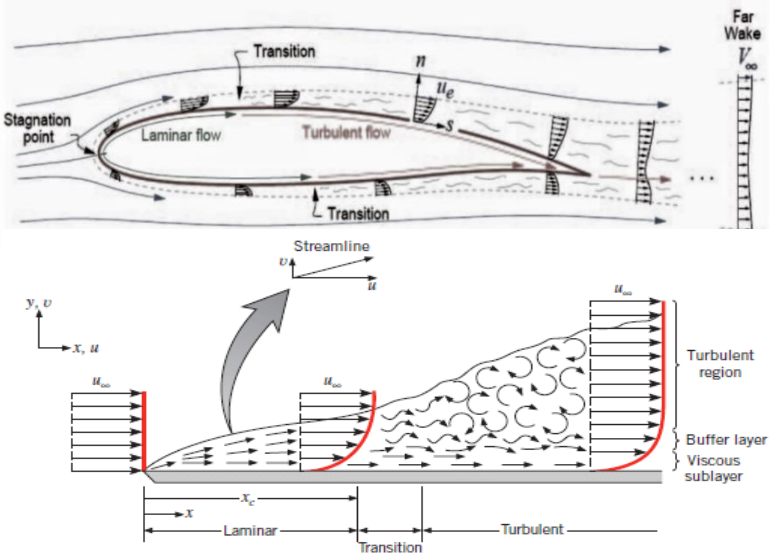

Figure 0-5 Boundary layer over an airfoil surface [1]

To summarize, the boundary layer is the thin zone of flow close to the surface where flow is slowed due to friction between a solid surface and the fluid, and its thickness is where fluid particles have an average velocity $\mathbf{U_x \leq 0,99U_\infty}$, according to x, as $\mathbf{U_\infty}$ represents freestream velocity.

The higher the Reynolds number, the lower the viscosity and the thinner the boundary layer. Despite the fact that the boundary layer occupies only a small part of the flow field, its influence on drag and heat transfer to the body is significant, so we know that when the Reynolds number is large, inertial forces dominate and the flow is turbulent. But even in turbulent flow, viscous forces in the boundary layers that occur on solid walls can be significant. Due to the non-slip condition, the shear stresses are large and close to a wall. This means that in a turbulent boundary layer there remains a very thin region near the wall where viscous forces dominate and the flow is essentially laminar, called the laminar or viscous sublayer. Its thickness decreases with increasing Reynolds number.

Above the laminar sublayer, there is the buffer layer, where both viscous and turbulent effects are significant. And above the buffer layer, the turbulent effects are dominant.

If the roughness of a surface is contained entirely within the thickness of the laminar sublayer, the surface is said to be hydraulically smooth, because the roughness has no effect on the turbulent flow above the sublayer.

Depending on the external pressure gradient, the boundary layer can remain attached, forming a huge recirculation zone that extends across the entire surface of the profile. If the kinetic energy is adequate to compensate for the pressure gradient's tendency to pull the particles upwards, the boundary layer can be connected to the profile closer downstream and before the trailing edge, which is less damaging to the aerodynamic performance.

I.3.2.2. The separation of the boundary layer

The pressure distribution of the external flow can have an influence on the formation of the boundary layer either positively or negatively, since the position of the Laminar/Turbulent transition is heavily dependent on it. If the pressure increases in the flow direction, as may occur in the region behind the profile, the boundary layer may separate from the wall and if we track a fluid molecule as it flows along with the profile. It moves due to inertial forces and viscous forces (friction) that already delay its speed. Moreover, it must proceed along with the flow while counteracting the increasing pressure, which tends to slow the flow even more. While maintaining its movement, the fluid particles can completely collapse and stop.

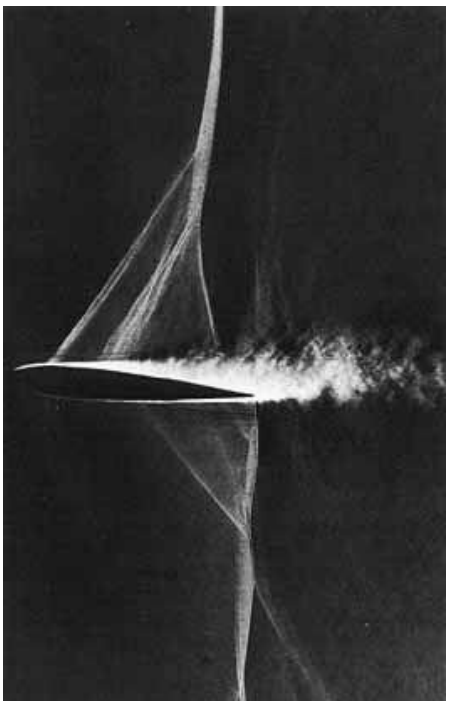

Figure 0-6 Schlieren photographs[1] [3]

When that happens, the fluid element will then move in the other direction, that is, upstream, due to the opposing pressure gradient. This reverse flow phenomenon causes the boundary layer to separate from the profile wall.

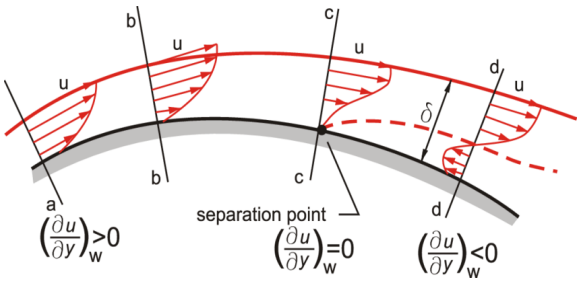

Figure 0-7 Different layers and flow regimes over an airfoil [4]

The detachment of flow from the surface that happens when the boundary layer travels far enough against an adverse pressure gradient is known as flow separation and the separation point is located where the condition "the gradient of the velocity normal to the wall equals zero" is satisfied.

[1] **Schlieren photograph** of transonic flow over an airfoil. The nearly vertical shock wave is followed by boundary layer separation that adversely affects lift, drag, and other flight parameters **[5]**.

I.3.2. Shock Boundary Layer Interaction

When a shock wave interacts with a boundary layer, damage can result. Unfortunately, in practice, SBLI occurs in transonic and supersonic flows, and studying these interactions is extremely difficult. Transonic interactions are distinguished from other SBLI by the presence of subsonic flow behind the shock wave and are mostly observed at Mach values less than 1.5.

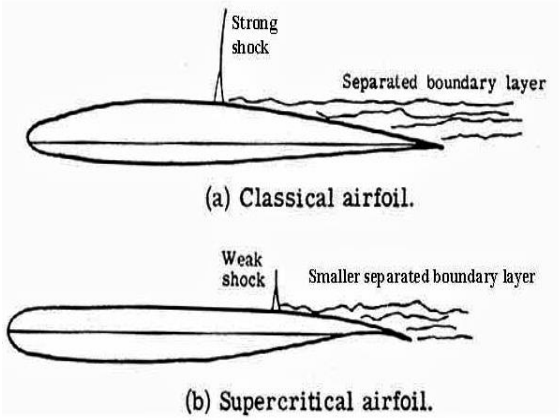

Figure 0-8 Shock and BL separation on Classical vs. Supercritical airfoil operating near Mach 1 [10]

The steady subsonic flow does not support the waves (**e**.**g**. shock waves or **Prandtl-Meyer** relaxation) and any change in flow conditions is progressive compared to supersonic flows. This imposes constraints on the shock structure in the interaction region since downstream flow conditions can anticipate and affect the force, shape, and position of the shock wave that causes the SBLI interaction **[11].**

A physical explanation for wave reflection is that there is a potential pressure shift at the limit between supersonic and subsonic regions. The pressure in the external subsonic region is determined by the global flow field and influenced by all directions. In the supersonic region, pressure can only move downstream (along the waves), resulting in a pressure

imbalance at the border, which is resolved by producing waves that are reflections of the incoming waves. The compression waves that return to the profile surface are demonstrated as compression waves unless are canceled by other formed waves from the surface's convex curvature. The compression waves are unable to reach the sonic line. In practice, the supersonic compression waves merge to create a shock wave that ends the supersonic flow **[12]**.

In a typical transonic **SBLI**, this shock wave interacts with the boundary layer at the wing's surface. The size of the supersonic region on the transonic profiles defines the position of the shock wave and its intensity.

In general, the greater the supersonic region, the higher the Mach number of the flow shortly before the shock wave.

As a result, the impact of the **SBLI** on a typical profile depends on the geometry of the profile, the freestream Mach number, and the angle of incidence. For example, thicker and more strongly curved profiles, higher freestream Mach numbers, and larger angles of attack all lead to stronger shock waves. If the shocks are severe enough, a local or complete separation can occur. A small separation bubble under the shock wave does not usually result in a large loss of performance while trailing edge separations cause additional drag and loss of lift (affecting the position and intensity of the shock). Once the flow is completely separated between the point of impact and the trailing edge, a stall occurs with significant effects on lift and drag. This accelerates the shock wave and reduces the supersonic region.

Figure (a) shows a conventional airfoil operating at Mach 1 with shocks and a separated boundary layer.

Figure (b) shows the supercritical airfoil at the same Mach number. The airfoil's top surface is flattened, which delays the creation and intensity of the shocks to a point closer to the trailing edge. Additionally, the shock-induced separation is greatly reduced.

I.4 Flow Control

Historically, flow control was intended to develop the flow into a more desirable pattern and to provide major gains in aerodynamic performance, making it an appealing technology for future aircraft development. It has been utilized to minimize noise, enhance lift, and reduce drag of an aerodynamic body by retarding the laminar/turbulent transition and boundary layer separation. A specific control technique is chosen based on the nature of the flow and the control objective to be achieved. The simplest way to explain this is to think of aerodynamic flow control as a practice of manipulating the flow field through a control surface or some sort of interaction to produce more desirable performance characteristics from an aerodynamic geometry.

This process requires a small forced modification in moving fluid that serves an ideally large engineering benefit, it is achieved by the use of active and passive methods. Passive flow control technologies, which include geometric shaping, the use of vortex generators, and the installation of longitudinal grooves or riblets on airfoil surfaces, require no auxiliary power and no control loop.

Active flow control techniques are those that necessitate the expenditure of energy, such as steady suction or blowing unsteady suction or blowing, and the employment of **synthetic jets**[1]. This can provide relaxed stability and flutter suppression, as well as a reduction of vibration levels.

AFC is divided into two categories: predetermined techniques and interactive methods.

- Predetermined methods include the injection of steady or unsteady energy inputs without consideration for the flow field's state. For example, jet vectoring with various types of actuators and form drag reduction using oscillatory blowing.

- The interactive methods enable to operate based on the state of the flow; the input to say an actuator is continually changed is based on sensors. As the interactive method can be a feed-forward (open) or feedback (closed) **[13].**

[1]**Synthetic jet** is a type of jet flow that comprises the surrounding fluid. The formation of such a jet is when the flow moves back and forth through a small opening. In simpler terms, a Jet flow is a fluid flow in which one fluid mixes with a surrounding medium. Any jet flow device comprises a diaphragm or a membrane that moves up and down hundreds of times per second sucking the surrounding fluid into say a chamber and expelling it.

I.5 Control surfaces:

I.5.1. Historical perspective of control surfaces

Transonic jet aircraft fly at speed of 0.8 to 0.9 Mach number. At these speeds, compressibility effects start to appear somewhere above the wing. The critical Mach number is the freestream Mach value at which local sonic velocities develop and usually it is preferable to increase the critical Mach number to delay the formation of shockwaves. This can be done either by sweeping the wings but the high sweep is not recommended in passenger aircraft, as there is a loss in the lift in subsonic speed and difficulties during construction.

In the development of an aircraft, current attempts in commercial aircraft design approaches are primarily focused on cost reduction, so engineers placed a high priority on the control surfaces and the precise prediction of their aerodynamic properties.

Many aircraft use control surfaces to provide the different flying functions such as pitch, roll, and yaw. The structure of the control surfaces is similar to that of the stabilizers, although the moveable surfaces are typically lighter. Some designers benefit from the new advances in composite technology, which allow for the use of carbon fiber and other forms of fiberglass since it has the potential to allow for the construction of stronger and lighter control surfaces, resulting in improved aerodynamic efficiency and greater performance.

The numerical analysis of flight control surfaces is used to get an early understanding of aircraft aerodynamics. This enables improved wing design, which leads to lower aerodynamic drag and fuel consumption. It can also be used to validate initial design assumptions and provide a foundation for further investigations, such as the ability to predict the aerodynamic performance of aircraft control surfaces early in the design process, which is a significant breakthrough in the field of aircraft design and will enhance flight safety.

I.5.2 Types of Control Surfaces:

Control Surfaces are categorized into two types:

- **Primary control surfaces** include the ailerons, rudder, and elevator.
- **Secondary control surfaces** such as tabs, flaps, spoilers, and slats.

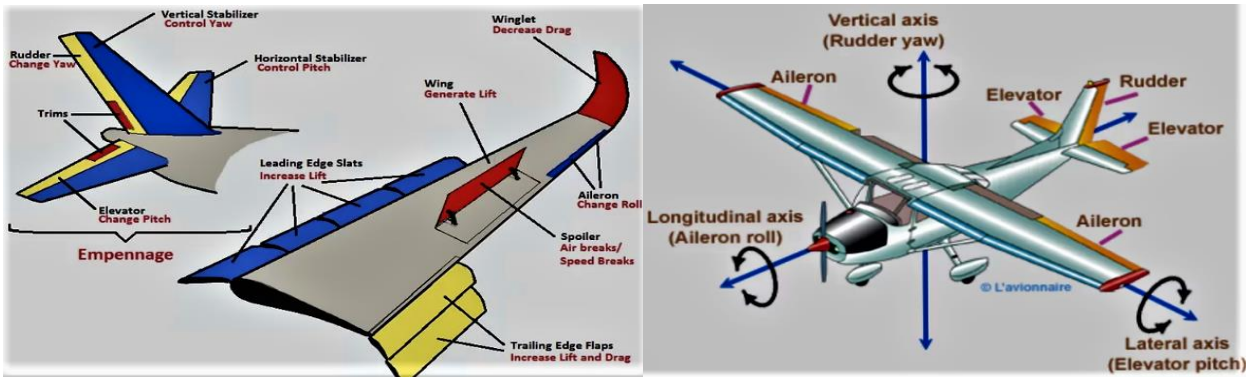

Figure 0-9 Aircraft control surfaces and their functions [14]

I.5.2.1. Primary & secondary control surfaces

1. Aileron:

Ailerons are fundamental flight control surfaces that govern the movement of an aircraft along its longitudinal axis by providing lateral (roll) control. Ailerons are typically located towards the wing tip on the trailing edge.

When the flaps are stretched beyond a certain point, the outboard ailerons activate. When the flaps are retracted, the outboard aileron control system is

"locked out" and the wing maintains its basic shape. Thus, only the inboard ailerons are required for control during cruising operations at relatively high speeds. During landing or other slow-flying activities, the outboard ailerons are active

The shape of the ailerons influences how far the ailerons move above or below the neutral setting, (The neutral setting lines the ailerons with the shape of the wing.) Ailerons on certain aircraft operate symmetrically, meaning they move up and down in the same amount and on other aircraft work asymmetrically, meaning that the upward-moving aileron moves further than the downward-moving aileron. In some aircraft designs, this asymmetrical action is used to reduce the amount of rudder pressure required during turning.

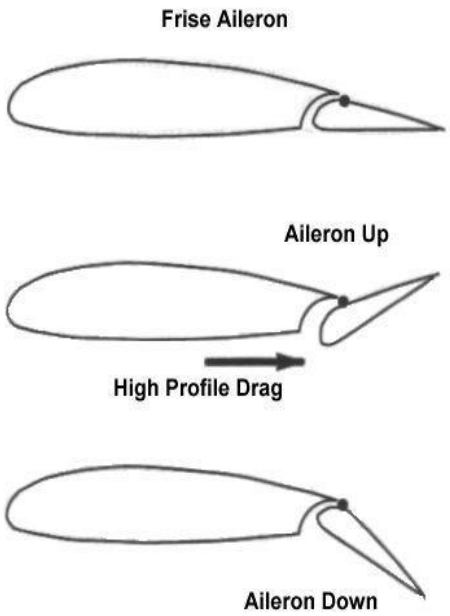

Figure 0-10 Aileron at different positions [15]

2. Elevators:

Elevators are the control surfaces that govern the movement (pitch) around the lateral axis. They are frequently linked to hinges on the horizontal stabilizer's rear spar. The construction of an elevator is similar to that of other control surfaces, and its design might be unbalanced or balanced aerodynamically and/or statically.

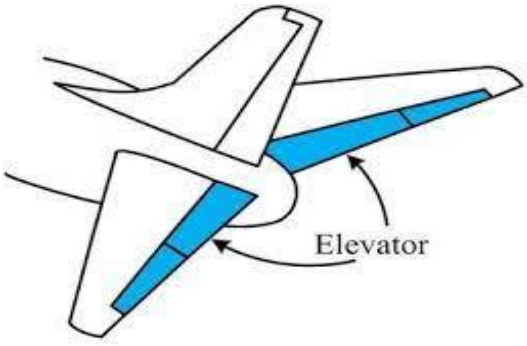

Figure 0-11 Aircraft Elevator [16]

3. Rudder:

The rudder controls the movement of the airplane about its vertical axis (Yaw). The basic structural and operational design of transport aircraft differs. Some are single structural units that are controlled by one or more systems. Others are built with two operational parts controlled by separate operating systems. A rudder is made up of two segments: upper and lower, and each part has a front and aft section. The aft rudder parts are hinged to the forward sections and are attached to the vertical stabilizer structure by pushrods [17].

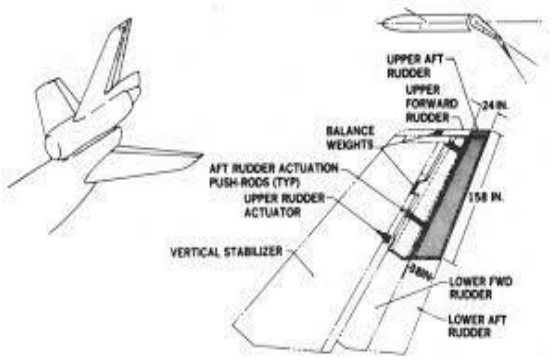

Figure 0-12 McDonnell Douglas DC-10 Rudder [18]

- ## Secondary control surfaces:

Secondary flight controls, also defined as auxiliary flight controls, have been designed to allow aircraft to operate across a wide speed range and with varying weight distributions.

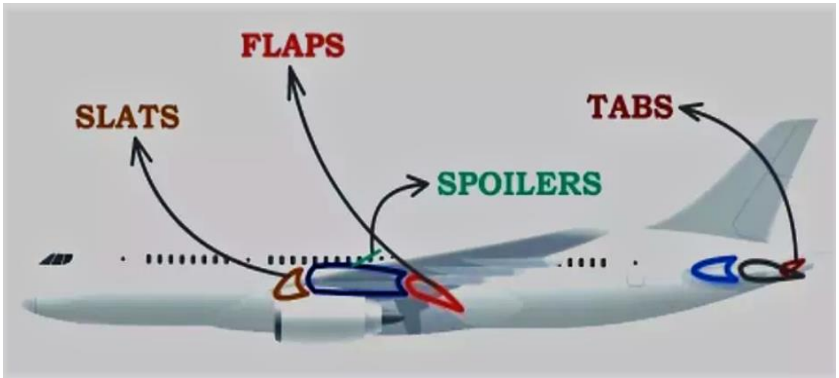

Figure 0-13 Secondary control surfaces [19]

The number of secondary control surfaces on a certain aircraft is determined by the kind of operation and flying speeds for which the aircraft is intended.

Some of these surfaces, such as **tabs**, allow the flight controls movement. Other surfaces, known as **high-lift** devices, include **flaps**, **slats**, and **slots**. These allow the aircraft wing's lift and drag characteristics to be modified, allowing for slow speed flight for take-off and landing and high-speed flight for cruising. The third type of surface is utilized to minimize lift and produce drag. **Spoilers** and speed brakes are included in this category.

1. Spoilers

In some aircraft designs, spoilers are the principal flight control for roll and are sometimes known as "lift dumpers," which intend to "spoil" and lower the amount of lift generated by the wing. The size of the spoiler varies according to how much lift is to be "spoiled" and are found on the top surface of wings and come in two basic shapes. The most common type on jet transport is a flat panel spoiler that is hinged at the forward edge and lies flush with the surface of the wing. When the spoilers are activated, they rise vertically from the wing, reducing lift. The spoiler is a multifunctional flight control surface with three main functions:

- **On-flight:** air braking for speed reduction, Roll control (to augment the ailerons in turning).
- **On-ground:** Air braking, during lift dumping. Ground spoilers are used only when the aircraft is on the ground and function in conjunction with flight spoilers to reduce wing lift during landing. They also increase the airplane's aerodynamic drag after landing to help it slow down.

Depending on the aircraft type, spoilers can be controlled manually by the pilot, or automatically by an automatic flight control system. However, the prediction of spoiler aerodynamic characteristics is still difficult. Consequently, the design and development of spoilers depend primarily on extensive wind tunnel testing. In order to efficiently develop theoretical methods that can aid in the design process a fundamental understanding of the spoiler flow field is required. A further stimulus to acquire a basic understanding of the spoiler flow field is the current/future interest in spoilers for active control technology (**ACT**) applications (e.g. flutter suppression, direct force control, gust load alleviation, etc…), effective

implementation is heavily dependent on the prediction accuracy of spoiler aerodynamic characteristics **[20]**.

2. Speed brakes

Some aircraft designs, specifically gliders and sailplanes, may lack a clear distinction between a spoiler and a dive brake since one control surface may perform both functions, i.e., decrease lift and increase drag.

Speed brakes, sometimes known as dive brakes, are massive drag panels used to help control the speed of an airplane.

Figure 0-14 Speed Brakes on aircraft wing [21]

They can be found on either the fuselage or the wings. If the structure is on the fuselage, the speed brake is located on the top or bottom of the structure increasing the aerodynamic drag of the aircraft and, as a result, rapidly decreasing its speed. When using speed brakes in pairs, one is situated on either side of the fuselage and they are also deployed symmetrically from the top and bottom of the wing surface to regulate the aircraft's speed as well as to function as spoilers to reduce the lift of the wings if they are situated on the wings **[22]**.

3. Slats & Slots

Slats are similar to slots in that they open and close. In fact, slots are frequently referred to as slats, despite the fact that they are technically a "fixed slat."

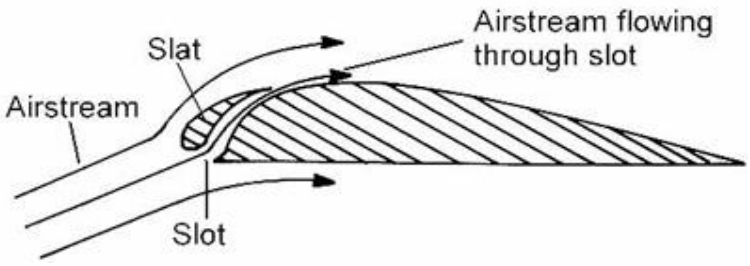

Figure 0-15 The slot and slat on a wing profile [23]

Slats are aerodynamic surfaces on the leading edge of the fixed-wing aircraft that glides down and forward, opening a gap behind it and increasing the camber of the leading edge. When deployed, it allows the wing to operate at a higher angle of attack. A higher coefficient of lift is produced because of the angle of attack and speed. They are one of several high-lift devices used on aircraft, including flap systems that run down the trailing edge of the wing, so by using it an aircraft can fly at slower speeds, or take off and land at shorter distances.

A leading-edge **slot** is a fixed aerodynamic feature of certain aircraft wings that reduces stall speed and promotes good low-speed handling. It is a spanwise opening in each wing that allows air to flow from below to above the wing. As a result, they may fly at a greater angle and speed, lowering the stall speed.

4. Flaps

The simple or camber flap operates in the same way as an aileron or other control surface. Flaps are a type of high lift device that consists of a hinged panel or panels located on the wing's trailing edge. They increase the camber and, in most cases, the chord and surface area of the wing when extended, resulting in an increase in both lift, drag, and a decrease in stall speed.

Flaps, like slots, can increase lift, but the main difference is that slots only extend the lift to higher values of the maximum lift coefficient when the angle of attack of the main section of the airfoil is greater than the normal stalling angle, whereas the high-lift type of flap increases the lift coefficient available across the entire range of angles of attack **[24].**

➢ Types of flaps

1. Leading-edge flaps

Flaps are often seen on the trailing edge of a wing, although they can also be found on the leading edge. They are only used in aircraft that require a lot of lift to land. At high angles of attack, a leading edge flap reduces the strength of the pressure peak over the wing, allowing the wing to operate at greater angles than would be possible without the flaps.

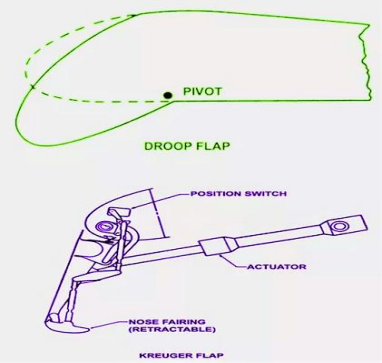

Figure 0-16 Leading-edge Droop & Krueger flaps [25]

1.1. Droop snoot

To provide a wing flap, build the wing with a leading-edge that can be drooped.

1.2. The Krueger flap

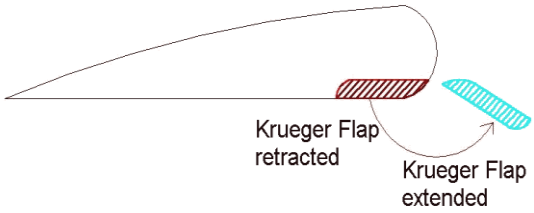

Figure 0-17 The different positions of Krueger flap [25]

Another technique for providing a leading edge flap is to create an extended surface known as the Krueger flap, which fits smoothly into the bottom half of the leading edge. When the flap is needed, the surface extends forward and downward.

2. Trailing edge flap

The trailing edge flap is simply a small auxiliary airfoil near the rear of the main airfoil that may be deflected around a specified line where it is hinged. This deflection changes the geometry of the wing, affecting its aerodynamic properties. Only a downward deflection is generally achievable if it was a high-lift flap design, but the deflection is variable.

In the case of a flap designed as a control surface, deflection in both senses is achievable, although the range of deflection is generally much less.

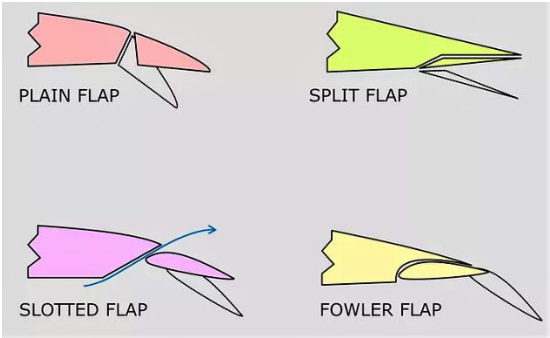

Figure 0-18 Types of the trailing edge flaps [14]

- General overview of the many forms of trailing edge flaps:

2.1. Camber flap (Plain flap)

The camber flap works by deflecting the trailing edge of the wing downward to adjust its camber. As a result, both lift and drag are increased and when it is lowered far enough, it creates an efficient air brake.

The plain flap can be hinged to the wing on the lower side or on the midway between the lower and upper surfaces.

2.2. Split flap

When folded, the split-flap forms the bottom surface of the wing's trailing edge. When expanded, the flap glides downward and has a similar effect as the pain flap. Plain and split flaps can be attached to the wing with three or more independent hinges, or they can be connected at the bottom with a continuous piano hinge.

2.3. Slotted flap

A slotted flap is identical to a simple flap, except that when the flap is expanded, a space forms between the wing and the flap. The leading edge of the flap is constructed such that air entering the gap flows easily through it, helping in maintaining the airflow on the surface, and by that the wing's lift is enhanced.

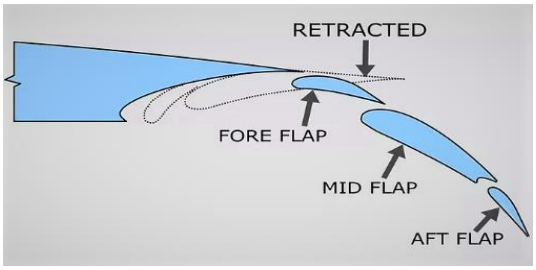

Figure 0-19 Triple slotted flap [14]

2.4. Flower flap:

The flower flap and others with similar operations are designed to significantly expand the wing area, the impact of the Flower flap when extended is to greatly decrease the aircraft's stalling speed by the rise in wing area and change in wing chamber.

- The combination of both Split flap and Fowler flap is called "Zap flap".

2.5. Jet flap:

Some aircraft designs use a combination of the fowler and slotted flaps to significantly enhance the plane's lift and drag. The jet flap is made of a high-speed jet of air pushed out through a thin gap in the wing's trailing edge. It separates the upper and lower surface flows and has an influence on the flow over the wing when it is directed significantly downwards **[26]**.

2.6. Tabs:

Tabs are small supplementary flight control surfaces inserted in the primary surfaces' trailing edges. These are used to minimize the pilot's efforts to keep the aircraft in a fixed attitude by "loading" the control surface in the appropriate position. They can also help the pilot restore a control surface to its neutral or trimmed center position.

Trim tabs are fixed or controllable small additional flight-control surfaces fitted into the trailing edges of primary control surfaces.

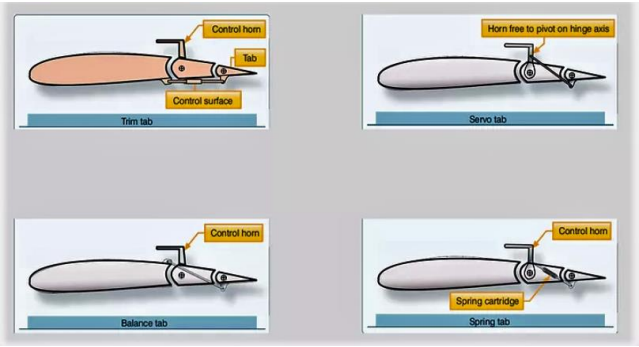

Figure 0-20 Types of Tabs [14]

A fixed trim tab is a piece of sheet metal that is twisted in the appropriate direction on the ground to minimize the pilot's required force for certain flight conditions. They are common on light aircraft and are used to modify the rudders and ailerons.

Controllable tabs are adjusted within the cockpit using control wheels, knobs, or cranks, and an indicator is provided to indicate the position of the tab. Most aircraft have controllable trim tabs. Normally, these tabs are operated manually, electrically, or hydraulically.

When the trim-control system is activated, the trim tab deflects in the opposite direction of the desired movement of the control surface. The air tries to push the trim tab back flush with the control surface when it is deflected into the

airstream. The entire control surface is moved since the control mechanism prevents the tab from being placed back flush.

3. Vortex Generators:

At present, there are different kinds of surface modifications to delay the flow separation in order to improve the aerodynamic efficiency of the aircraft, including vortex generators to modify the surface of aircraft wings.

A vortex generator is an aerodynamic surface, consisting of a small vane that creates a vortex. The effect of vortices produces turbulence, which delays the boundary layer separation resulting in a decrease in pressure drag and increasing the lift at high angles of attack. They are typically rectangular or triangular and taller than the boundary layer running in spanwise lines near the thickest part of the wing **[27].**

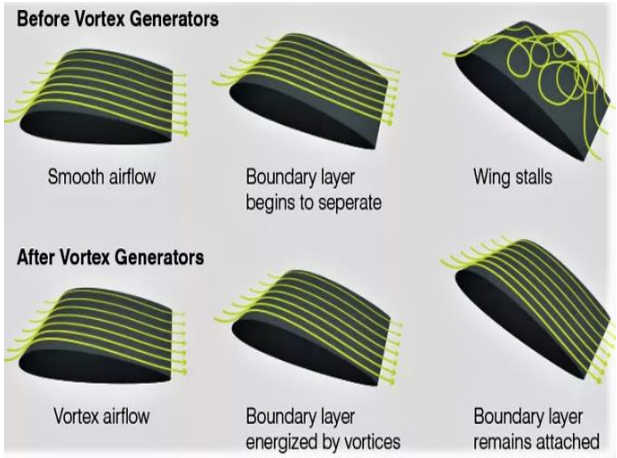

Figure 0-21 The pattern of airflow before and after vortex generators [14]

I.6 Literature review

This part discusses past experimental and numerical research, and it is divided into categories beginning with "Wind tunnel studies," next "Flow control and transonic regime," then "Wings and Airfoils," and finally "Control surfaces" to establish a strong bibliographic basis for my work.

I.6.1. Wind tunnel studies

January 1, 1920, by Caldwell, Frank W., and Elisha Noel Fales [28]: A significant deal of study and experimental work has been done, with some

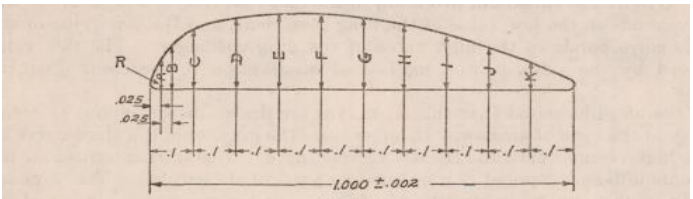

FIG. 35.

Max. thickness.	A	B	C	D	E	F	G	H	I	J	K	R
0.08	0.032	0.047	0.063	0.076	0.080	0.079	0.076	0.069	0.059	0.044	0.028	0.008
.10	.041	.059	.079	.095	.100	.099	.095	.087	.074	.056	.035	.010
.12	.049	.070	.094	.114	.120	.118	.114	.104	.088	.067	.042	.012
.14	.057	.082	.110	.133	.140	.138	.133	.121	.103	.078	.049	.014
.16	.065	.094	.126	.152	.160	.158	.152	.139	.118	.089	.056	.016
.18	.073	.106	.142	.171	.180	.178	.171	.156	.133	.100	.063	.018
.20	.082	.118	.158	.190	.200	.198	.190	.174	.148	.112	.070	.020

Figure 0-22 Results are taken from Caldwell, Frank W., and Elisha Noel Fales. Wind tunnel studies [28].

success, in an attempt to establish airplane and propeller design on an experimental basis. However, one can only be affected by the apparent lack of data available to demonstrate flow phenomena upon a rational basis, With this goal in mind, the authors set out to create a wind tunnel unlike any other, particularly in terms of high power and flow speed. This paper **[28]** details the Mccook Field wind tunnel and the results of trials undertaken to assess the wind tunnel's efficiency.

F. W. Caldwell and E. N. Fales adopted six model tests on propeller aerofoils which were of 6 inches in length, 1-inch chord, and 0.1 to 0.2 camber. The cross-sectional shape, as shown in the figure **I.22**

The most important conclusion to be derived from the testing is that we have more than one air flow regime to deal with in aerofoil research, and that these regimes are divided by discontinuities. The features often associated with a

functional aerofoil in aeronautical engineering do not apply outside of the restricted range of cambers, speeds, and angles used in flight. Beyond this range, the flow around the aerofoil no longer provides the conventional lift and drag results, but instead becomes comparable to the flow around an irregularly shaped body. The efficient lift of an aerofoil is just one of numerous unique aerodynamic phenomena caused by air flow through a solid surface.

When the speed of air flowing past aerofoil increases there is first a regime of relatively low-lift effect, then at higher speeds an efficient lift effect such as applies in flight, then at still higher speeds a drop back to a second low-lift effect. As the angle or camber increases the high-lift regime becomes discontinuous and is succeeded by the low-lift regime, the transition point is spoken of in conventional graphs as the "critical, or stalling, angle," or the "burble point." **[28].**

May 16, 1947, by Fullmer, and Felicien F. [29]: An investigation was made in the Langley two-dimensional low-turbulence pressure tunnel to determine the characteristics of leading-edge flaps used as high-lift devices. The investigation conducted a Reynolds number of $\mathbf{6 \times 10^6}$ included teste of two 10-percent-chord Leading-edge flaps, one was designed to slide forward along the upper surface of a NACA641-0012 airfoil, while the other was hinged near the leading edge on the bottom surface, with and without a 20% chord trailing-edge split flap. The section lift characteristics for a range of flap deflections are shown, as well as the pitching moment characteristics and lift characteristics with leading-edge roughness for the best flap arrangements. The maximum section lift-coefficient increments for the optimum upper- and lower-surface leading-edge flap configurations on the plain airfoil were 0.43 and 0.12, respectively, according to the results. The corresponding angle of attack increases for maximum section lift coefficients were 4.0° and 1.4°, respectively. The optimum upper and lower-surface leading-edge flaps generated increments of 0.81 and 0.43 when the airfoil was coupled with a 20-percent-chord trailing-edge split flap deflected 60°.

The corresponding increments in the angle of attack for the maximum section lift coefficients were 6.9° and 3.9°. The highest maximum section lift coefficient, 2.98 at an angle of attack of 16.2°, was obtained when the upper-surface leading-edge flap was used in combination with the trailing-edge split flap. The deflection

of either type of leading-edge flap resulted in a forward movement of the aerodynamic center at high angles of attack. The lower surface leading-edge flap installation was less sensitive to Leading-edge roughness than the upper-surface leading-edge flap arrangement. With the trailing-edge flap, the maximum section lift coefficient for the upper surface of the leading-edge flap in the rough condition, however, was about the same as the maximum lift coefficient obtained for the lower-surface leading-edge flap in the smooth condition **[29].**

November 5, 1951, by Sleeman Jr, William C., Paul L. Klevatt, and Edward L [30]: The purpose of this research was to look into the possibilities and limitations of transonic testing of reasonably large lifting wings in a rectangular slotted tunnel. The transonic aerodynamic properties of unswept and 45° sweptback wings are compared in the Langley high-speed 7-by-10-foot tunnel and the Langley Internal Aerodynamics Section's 4.5-by-6.25-inch slotted tunnel. To study the impacts of relative model size in the slotted tunnel, two geometrically comparable wings with sizes equal to 32% and 12% of the tunnel cross-sectional area were studied for both sweep angles. In the testing, two-slot regions with 1/5 and 1/8 of the horizontal borders open were employed.

It was found that tunnel choking was eliminated and blockage effects for the wings tested were alleviated by the slotted test section throughout the Mach number range and lift range investigated. The overall transonic aerodynamic characteristics of the four wings tested in the-open slotted tunnel, neglecting all tunnel boundary corrections, were consistent with 7- by 10-foot tunnel results throughout the Mach number range investigated. The amount of slot open area showed a substantial effect at subsonic Mach numbers on lift-curve slopes, while effects of the relative size of the model predominated at supersonic Mach numbers. Jet boundary interference effects in the slotted tunnel, as indicated by subsonic lift-curve slopes and pitching-moment characteristics near a Mach number of unity increased appreciably with model size for the sweptback wings **[30]**.

December 1987 by Ladson, Charles L., and S. Acquilla Hill [31]: A complete test program that is known as Advanced Technology Airfoil Test program was carried out in the Langley Research Center's 0.3-meter transonic

cryogenic tunnel to determine the static aerodynamic properties of a variety of two-dimensional airfoils at transonic speeds and flight equivalent Reynolds numbers. The Langley Aircraft Energy Efficiency Project Office and the Transonic Aerodynamics Division supported the (**ATAT**) tests on a NACA 0012 airfoil to obtain aerodynamic data as a part of the program which covered a Mach number range of 0.30 to 0.82 and a Reynolds number range of $\mathbf{3 \times 10^6}$ to $\mathbf{45 \times 10^6}$. To produce these test conditions, the stagnation pressure varied between 1.2 and 6.0 atmospheres, while the stagnation temperature was changed between 300 K and 90 K.

I.6.2. Flow control and transonic regime

Airplane aerodynamics, from the time of the Wright Flyer to the beginning of World War II, assumed that changes in air density were negligible as the air flowed over the airplane. This assumption, called incompressible flow, was reasonable for the 350 mph or slower flight speeds of airplanes during that era. Theoretically, it was a tremendous advantage to assume constant density, and physically the low-speed aerodynamic flows usually exhibited smooth variations with no sudden changes or surprises. All this changed when flight speeds began to speed up close to the speed of sound. The aerodynamic theory had to account for changes in the air density in the flow field around the airplane, and physically the flow field sometimes acted erratically, and frequently surprised and greatly challenged aerodynamicists. Aerodynanticists in the 1930s simply threw these phenomena into one pot and called them generically "compressibility problems." **[32].**

Figure 0-23 John Stack, Langley Research Center scientist, was Presented the Collier Trophy in 1947, awarded for his conception of transonic research airplanes. His research contributed to the X-1 breaking the sound barrier on October 14, 1947. (NASA Photo No. LMAL

On **October 14, 1947**, As the Bell X-I approached Mach one, a region of the aerodynamic flow above the wing became locally supersonic. This is because the airflow increases its velocity as it moves over the top of the wing, therefore there is always a section of the flow over the wing where the local velocity is greater than the airplane's velocity. As the X-1 approached Mach 0.87, a pocket of locally supersonic flow developed over the top of the wing. This supersonic pocket was ended on the downstream by a normal shock, which was practically perpendicular to the flow. This shock formation was the cause that made flight at Mach one such a terrifying prospect at the time.

Bryan, G. H 1918-1919 [33]*:* working for the Committee at the Royal Aeronautical Establishment in 1918 and 1919, conducted a theoretical analysis of subsonic and supersonic flows on a circular cylinder (a simple geometric shape chosen for convenience). He demonstrated that compressibility pushed adjacent streamlines further apart in a subsonic flow. His study was difficult and complex, a foreshadowing of things to come, and provided few useful data. However, it highlighted the British's concern about the impact of compressibility on propeller performance **[33].**

January 22, 1947, by Mathews, Charles W., and Jim Rogers Thompson [34]: Drag measurements at transonic speeds on rectangular and swept-back 45° airfoils are provided. These airfoils, placed on cylindrical test bodies, are part of a series being tested in free drops from high altitudes to assess the influence of fundamental airfoil parameter change on airfoil drag characteristics at transonic speeds. These rectangular and swept-back airfoils had the same span, airfoil section **(NACA 65-009)**, and chord perpendicular to the leading edge. The studies were performed to evaluate the drag of rectangular and sweptback airfoils at a larger aspect ratio than had previously been used in an identical comparison. At a Mach number of 1, the drag of the swept-back airfoil was less than 0.15 that of the rectangular airfoil and less than 0.30 that of the rectangular airfoil at a Mach number of 1.17.

A comparison of these swept-back airfoils to similar airfoils with lower aspect ratios previously studied using the same method showed that in the observed speed range, decreasing aspect ratios resulted in greater drag. However, in the

highest part of the examined speed range, the drag coefficient of the high-aspect-ratio swept-back airfoils approached that of the lower-aspect-ratio swept-back airfoils A similar comparison for the rectangular airfoils showed that delay in the drag rise and a reduction in drag at supercritical speeds can be realIzed through a reduction in aspect ratio. These results confirm those reported in **NACA ACR No. L5J16 [34]**.

January 1, 1958, by Chapman, Dean R., Donald M. Kuehn, and Howard K. Larson [35]: The report shows the results of an experimental and theoretical study on flow separation related to steps, bases, compression corners, curved surfaces, shock-wave boundary-layer reflections, and leading-edge separation configurations. Pressure-distribution measurements, shadowgraph studies, high-speed motion images, and oil-film investigations all proved successful. The maximum measurement range included Mach values ranging from 0.4 to 3.6 and length Reynolds numbers ranging from 4000 to 5 million

S Corrsin 1961 [36] demonstrated that the direct numerical simulation of high-Reynolds-number flows places an overwhelming demand on computer memory and speed. [See Chapman (1979) for a comprehensive study of the grid requirements for computational aerodynamics.] In direct simulations the number of spatial grid points is determined by two constraints: first, the size of the computational domain must be large enough to accommodate the largest turbulence scales (or the scale of the apparatus), and second, the grid spacing must be sufficiently fine to resolve the dissipation length scale**.**

October 21, 1977, by Tijdeman and Hendrik [37]: The authors present exploratory wind tunnel tests in high-subsonic and transonic flow on a conventional airfoil with an oscillating flap and a supercritical airfoil oscillating in pitch. The experimental data are analyzed with a focus on the typical features of transonic flow, particularly the interaction between the steady and unsteady flow fields, the periodic motion of the shock waves, and their contribution to the total unsteady air loads. The behavior of the supercritical airfoil in its "shock-free" design condition is given special consideration. Furthermore, it is examined to what extent linearization of the unsteady transonic flow issue is possible when the unstable field is seen as a small perturbation superimposed on a given mean

steady-flow field. Finally, the current state of unstable transonic flow theory is discussed, and current test results are utilized to assess several recently developed computation techniques.

Rogallo, R. S., Parviz Moin 1984 [38]: In this study, the Navier-Stokes equations govern computational models of turbulence in incompressible Newtonian fluids. The governing equations are examined, and turbulence numerical modeling demands considerations of these equations, initial and boundary conditions, numerical resolution, and techniques. It details some of the various options and the outcomes that emerge from them, as well as direct and large-eddy simulations. The resolution requirements and numerical methodologies of spatial representation, formulation of initial and boundary conditions, and time progression are all taken into account. The visual and discussion results of simulations of homogeneous turbulence in uniform shear, the evolution of a turbulent mixing layer, and turbulent channel flow are shown.

November 17, 1987, by Raghunathan, S [39]: This paper reviews theoretical and experimental research on passive control shock-boundary layer. In **1983**, the first paper in this field was published. Since then, there have been researching programs in the United States, Germany, and the United Kingdom to better comprehend the notion of passive shock wave boundary layer control and to anticipate the effect of such a control on the aerodynamic forces on an aerofoil. This review demonstrates how passive control in transonic flow may reduce drag, improve lift, and minimize unstable pressures on an airfoil.

Stanewsky, E., Délery, J., Fulker, J., Geissler, W. 1997 [40]: ONERA, the University of Karlsruhe, and Cambridge University conducted fundamental studies on transonic shock wave boundary layer interaction under passive control circumstances, with each institution focusing on a different part of the topic. Extensive tests, together with a theoretical analysis of the data, have enabled the definition of certain fundamental physical processes involved in the control mechanism. The research done by the universities of Karlsruhe and Cambridge has allowed for the development of more precise transpiration rules that take into consideration the precise properties of the perforated plates. ONERA obtained detailed information on turbulence behavior. Thus, it is clear that the blowing in the

first part of the control region causes a rapid thickening of the boundary layer, with the resulting increase in displacement thickness being felt as a ramp by the outer inviscid flow, with the formation of a lambda shock pattern replacing the single normal shock of the interaction without control. As a result, the wave drag is significantly reduced. The combined blowing-suction effect and hole roughness, on the other hand, generate an increase in friction drag, which can exceed the improvement in wave drag.

The same conclusions hold valid for interactions in 2D and 3D. The influence of the porous plate shape on shock control efficacy appears to be quite weak. Turbulence typically rises as a result of control, which may be linked to the blowing action's increased instability of the boundary layer. Numerical simulations of the interactions in two- and three-dimensional flows reveal significant flaws in the fundamental turbulence models, which frequently provide unsatisfactory results even in the reference solid wall case. Despite these limitations, Navier-Stokes computations using relatively basic algebraic turbulence models can be useful in investigating flow physics, testing new physical models, and running comparative investigations of alternative control systems.

ADAM JOSEPH WELLS 2005 [41]: This thesis study successfully illustrated how the CFJ airfoil moved from CFD modeling to wind tunnel testing. It proved the CFJ airfoil's high-performance capability. In terms of maximum lift and stall margin, the smaller injection slot airfoil outperformed the larger injection slot airfoil. It was also demonstrated that the larger injection slot airfoil excelled over the smaller injection slot airfoil in terms of lift for a given angle of attack and drag reduction. The PIV data gave evidence of how the stagnation point position changes as mass flow rates fluctuate.

When the stagnation point moves, the lift and drag properties change. The PIV data collected was utilized to create velocity profiles of the CFJ airfoil and compare them to those of a conventional airfoil. The information was also utilized to compare the velocity profiles of two distinct CFJ airfoils employed in wind tunnel experiments.

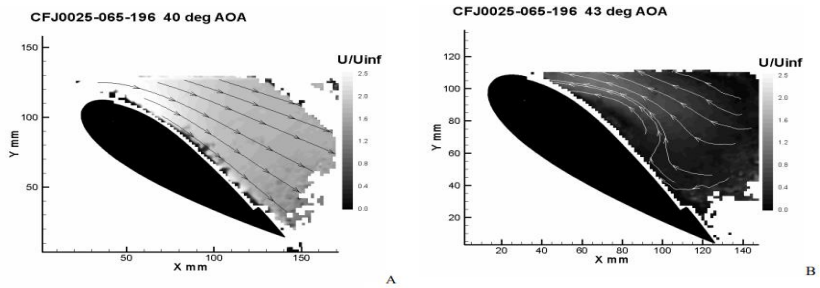

Figure 0-24 PIV image of flow over CFJ0025-065-196 A) 40 deg

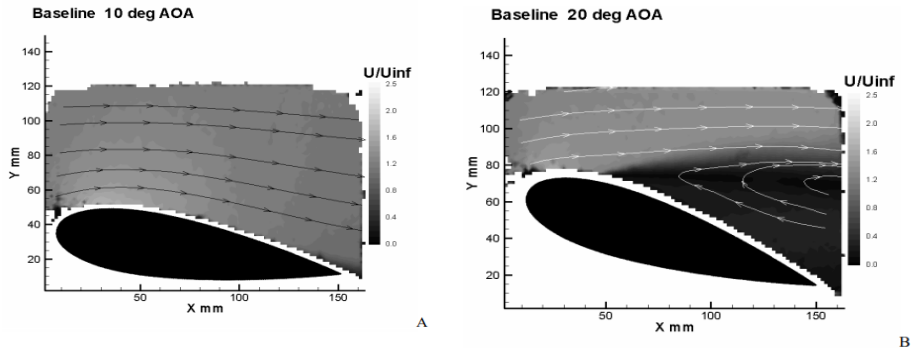

Figure 0-25 PIV image of flow over baseline airfoil A) 10 deg and B) 20 deg [41].

November 2006, by K. Richter, S. Koch, H. Rosemann DLR AS-HK and Bunsenstr [42]: A new high Reynolds number design approach for transonic airfoils with an application in the outer part of a modern transport aircraft wing was researched and tested. Unlike traditional low Reynolds number design approaches, this method takes use of complete aerodynamic performance and controls the boundary layer characteristics. Three airfoils with very similar aerodynamic performance but differing boundary layer developments on the top surface were developed for transonic free flight situations. RANS calculations were used to examine and evaluate the performance and boundary layer properties of the airfoils.

April 2016 [43]: Three airfoils with very similar aerodynamic performance but differing boundary layer developments on the top surface were developed for transonic free flight situations. RANS calculations were used to examine and evaluate the performance and boundary layer properties of the airfoils.

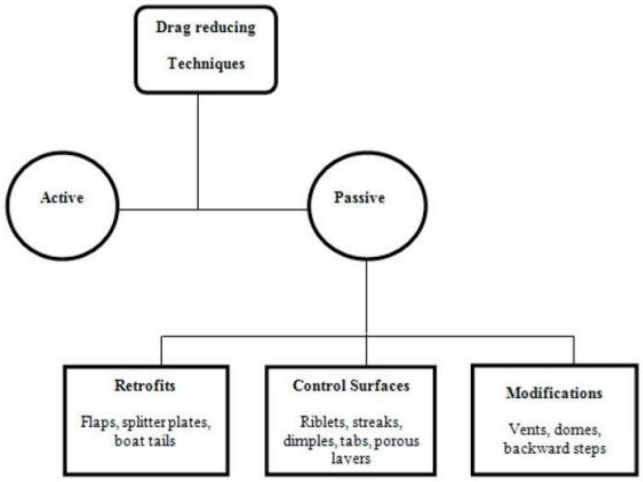

Figure 0-26 Classification of passive flow control techniques [43]

This paper's content focuses on flow control, its importance, and an in-depth examination of flow control technologies. It also covers the development of flow control techniques during the last few decades. The authors also investigated drag, drag reduction, turbulence, and turbulence control. To simulate the flow in CFD software, a detailed understanding of the turbulence models used in computer science is required. Simulating multi-physical medium models is difficult, thus academics have developed novel models, such as the Penalization approach, to address such issues. Active approaches will outperform passive methods in terms of drag reduction and control. However, due to problems in sensor technology and algorithm development, active flow control has limitations. Passive approaches are simple to use and do not require any external energy.

I.8.2. Wings and Airfoils:

Gorrell, Edgar S. & Martin, H. S. 1917 [44]: The NACA Technical Report No. 18 titled *"Aerofoils and Aerofoil Structural Combinations"* was published in 1917. The authors claim that mathematical theory has yet to be applied to airfoil design. At that time, much of the effort was trial and error. Multiple brass airfoil models

with spans of 18 inches and chords of 3 inches were tested in a wide tunnel. The report summarizes the findings of wind tunnel studies on cambered aerofoils and biplane body-wing combinations. Aerodynamic parameters such as drag, lift-drift ratio, and stability derivatives are provided.

L. J. BRIGGS and H. L. DRYDEN 1927 [45]: This paper offers an elaboration of an analysis of the aerodynamic properties of particular airfoils described in N. A. C. A. Technical Report No. 207. The work was done at the request and with the financial support of the National Advisory Committee for Aeronautics. The Chemical Warfare Service kindly provided a big compressor facility at Edgewood Arsenal for the trials. Through a more comprehensive and methodical set of testing, the conclusions given in Report No. 207 were confirmed and expanded to greater speeds. Air flow near the surface of the airfoils was also observed, and dramatic variations in lift coefficients were found to be connected with an abrupt breaking away of the flow from the top surface.

The studies were performed on 1-inch chord models, and a comparison with previous measurements on 3-inch chord models demonstrates that the sudden change in the lift coefficient is attributable to compressibility instead of a change in the Reynolds Number. However, the Reynolds Number has a significant impact on the drag coefficient. The pressure distribution measurements provide data on the load distribution at high speeds to the propeller designer, as well as a better image of the air-flow changes.

The NACA started looking for techniques to improve the maximum lift of an airfoil in the late **1930s**. They introduced the NACA five-digit airfoil series, as well as airfoils such as the 23012, which are used on aircraft such as the Beechcraft Bonanza. The camber and thickness was represented in the first and last two digits, and the second digit indicated twentieths of a chord rather than tenths. The middle digit represented either a straight mean camber line or a curved mean camber line.

FIGURE I.27. A technician readies the recording instrumentation of a P-51D Mustang modified for wing-flow transonic research. The test model (an XS-1 shape with a swept horizontal tail) is at midspan, with mechanical linkages connecting it to the instrumentation installed within the modified gun bay. NASA Image L-46802 [46]

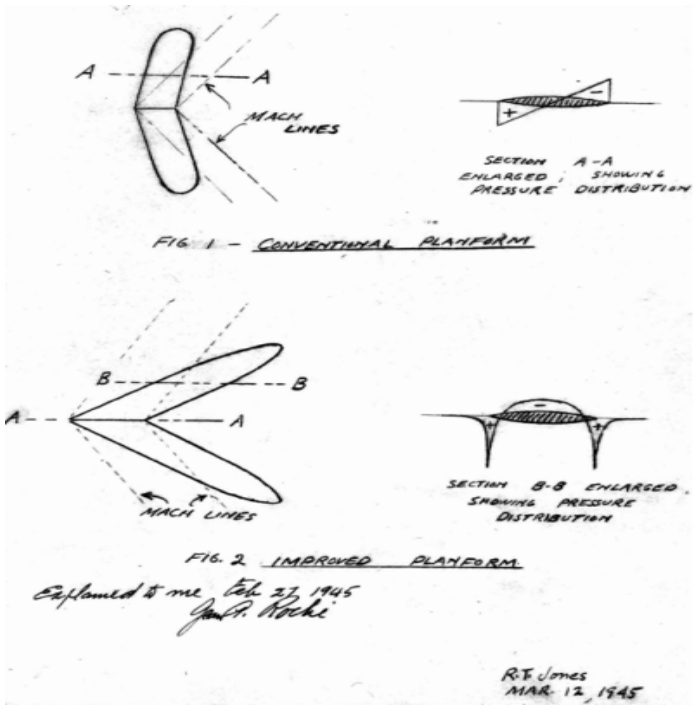

Figure 0-28. Jones's initial conception of the swept wing, noting his briefing to AAF Representative Jean Roché in late February 1945. Robert T. Jones biographical file, NASA History Division, Washington, DC [46]

May 1, 1947, by Furlong, G. Chester, and James E. Fitzpatrick [47]

The present paper contains the results of tests made with a wing of NACA 230-series airfoil sections in Langley 19-foot pressure tunnel · The tests were conducted at tunnel pressures of 14.7 and 33 pounds per square inch absolute. These tunnel pressures gave Mach number ranges of 0.10 to 0.35 and 0.08 to 0.27

The corresponding Reynolds number ranges were from 1.53×10^6 to 4.53×10^6 and from 2.45×10^6 to 7.88×10^6, respectively. The tests included force tests and chordwipressure-distribution measurements at six spanwise stations. Wings with full-span, partial-span, or split flaps deflected 60 degrees and without flaps were tested. All flap designs had their pressure distribution measured chordwise. Peak values of maximum lift coefficient were attained at relatively low free-stream Mach numbers and were nearly totally reliant on Reynolds Number before reaching the critical Mach number. By raising the Mach number or deflecting the flaps, the lift coefficient increased, however, the critical pressure coefficient was attained at lower free-stream Mach numbers.

February 25, 1952, by McDevitt, John B [48]: The transonic similarity principles were used to connect experimental data for a set of 22 rectangular wings with symmetrical NACA 63A-series sections, aspect ratios ranging from 1/2 to 6, and thicknesses ranging from 2 to 10%. The data were collected using the transonic bump technique over a Mach number range of 0.40 to 1.10, which corresponds to a Reynolds number range of 1.25 to 2.05 million. The results indicate that by employing transonic similarity parameters in forms consistent with the Prandtl-Glauert rule of linearized theory, it is possible to match experimental data throughout the subsonic, transonic, and moderate supersonic regimes. The many families of fundamental data curves for different aspect ratios and thickness ratios have been summarized in single presentations involving just one geometric variable - the product of the aspect ratio and the l/3 power of the thickness ratio.

March 1988, by Wood, N. J., and L. Roberts [49]

For modest blowing requirements, preliminary results show that coflowing, tangential leading-edge mass injection can extend the zone of stable, controlled vortical flow across the top surface of a delta wing by roughly 30 deg angle of attack. Maximum normal force coefficients were increased by roughly 30%, and considerable rolling moments were created at angles of attack ranging from 35 to 60 degree.

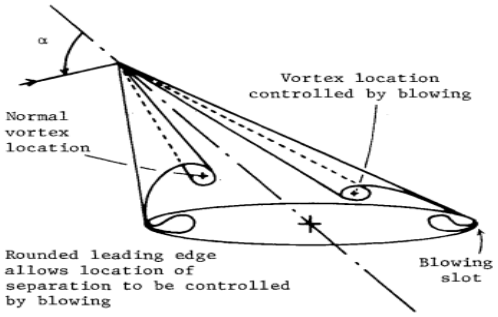

Figure 0-24 Concept of crossflow separation control [49]

The concept shown a dissociation of the two lift components, linear and nonlinear. This implies that such a method might be a feasible option for modifying normal force without changing attitude, producing control moments at extremely high angles of attack (both steady and transient), and raising the L/D of very narrow cone-like bodies at modest angles of attack. The decoupling of the lift components was proven to be dependent on the crossflow blowing momentum coefficient, implying that operation at speeds greater than Mach 1 should be conceivable.

September 9, 2009 (1985–1994) by Jacquin, Laurent, et al [50]

Flow unsteadiness caused by shock-induced separation across a supercritical transonic profile (the ONERA OAT15A profile) has been carefully investigated experimentally in order to offer well-documented test cases for validating advanced predictive algorithms. The statistics also give additional information that may be used to further understand the phenomena. The research was carried out in a transonic wind tunnel equipped with adaptable walls for a variety of upstream Mach numbers and angles of incidence in order to properly

quantify the conditions that lead to a transonic buffet. Surface flow visualization, high-speed schlieren videography, and steady and unsteady surface pressure measurements were used to analyze the flow. The pressure measurements have provided a precise characterization of the buffet start conditions as a function of the flow upstream Mach number and profile incidence.

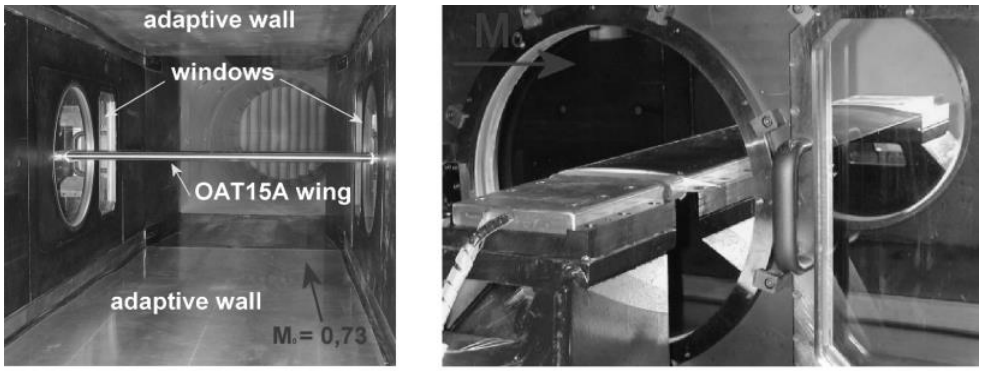

a) General view **b) Close up of model fixation**

Figure 0-25 OAT15A supercritical profile in the S3Ch transonic wind tunnel

The study was carried out in the continuous closed-circuit transonic S3Ch wind tunnel of the ONERA-Meudon Center. This facility is powered by a 3500 kW two-stage motor-ventilator group and has a test section size of $\mathbf{0.78} \times \mathbf{0.78} \times \mathbf{2.2}$ m. The Mach number domain extends from 0.3 to 1.2, the stagnation pressure being the atmospheric pressure, and the stagnation temperature comprised between 290 and 310 K. The model is an OAT15A profile with a relative thickness of 12.3%, a chord length $c = 230\,mm$, a span of 780 mm (which gives an aspect ratio $AR = 3.4$), and a thick trailing edge of 0.5% of the chord length.

January 11, 2012, by Huang, JingBo, et al [51] Throughout this paper, IDDES, one of the most advanced RANS/LES hybrid methods, is used to numerically simulate extremely unsteady shock wave buffet induced by strong shock wave/boundary-layer interactions (SWBLI) on the upper surface of an OAT15A supercritical airfoil at a Mach number of 0.73 and angle of attack of 3.5 degrees.

The results indicate that conventional URANS approaches are incapable of accurately predicting the buffet phenomena on the wing surface, IDDES, which includes additional flow physics, anticipated the buffeting phenomenon. Some

complicated flow phenomena are expected and shown, including shock wave oscillations in the streamwise direction, a powerful shear layer separated from the shock wave owing to SWBLI, and plenty of small-scale structures broken down by shear layer instability and in the wake. Root Mean Square (RMS) of fluctuating pressure coefficients and the streamwise range of shock wave oscillation are in good agreement with the experimental results. Then, to reduce the shock wave buffet, two vortex generators (VG) with an inclination angle of 30 degrees to the main flow directions are positioned in front of the shock wave zone on the upper surface.

The results indicate that VGs may greatly suppress shock wave buffet, that the RMS level of pressure in the buffet zone is successfully reduced, and that the averaged shock wave position is noticeably shifted downstream, resulting in higher overall lift.

August 26, 2015, by Jain, Shubham, Nekkanti Sitaram, and Sriram Krishnaswamy [52]: The study presents steady-state, two-dimensional computational experiments done on the NACA 0012 airfoil to examine the influence of Reynolds number fluctuation on the aerodynamics of the airfoil without and with a Gurney flap of the height of 3 % chord. The computations are carried out using the RANS-based one-equation Spalart-Allmaras model.

At all Reynolds numbers and angles of attack, both lift and drag coefficients increase with Gurney flap compared to those without.

The following major conclusions are taken:

- Reynolds number plays a very major role in the airfoil aerodynamics for the NACA0012 airfoil without and with Gurney flap. Lift decreases and drag increases when Reynolds number is decreased.
- For the airfoil with GF, the Reynolds number has adverse effects on lift coefficient, while drag coefficient of the airfoil with GF has some beneficial effects compared to the airfoil without GF.

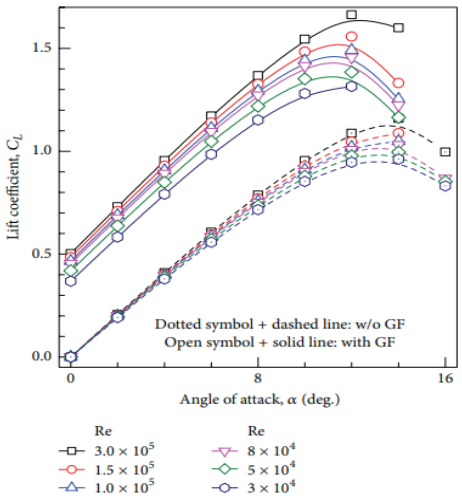

Figure 0-26 Variation of C_l with AoA for different Reynolds numbers for the airfoil without and with GF [52].

- For high Reynolds number above critical range, decrease in C_l and increase in C_d are negligible.
- As the Reynolds number is decreased below the critical Reynolds number range, C_l decreases and C_d increases at a very steep rate and the performance degrades rapidly.
- For lower Reynolds numbers, the two vortices behind the Gurney flap vanish. The Gurney flap seems to increase the effective camber of the airfoil, causing negative zero-lift angle and reduced stall angle.

September 9, 2015, by Kumar, K. Harish, C. K. Kumar, and T. Naveen Kumar [53]: The primary purpose of the article is to simulate and analyze the RAE 2822 supercritical airfoil with and without wedge profiles, as well as to investigate aerodynamic parameters such as lift and drag coefficients at various Mach numbers. The research also concentrated on the computation at various angles of attack and the free stream.

"The airfoil with wedge profile is more stable and contributes to better performance for operation at an angle less than 10 degrees up to Mach 1 and up to stall angle beyond Mach 1. This Shows that Supercritical airfoil with wedge profile is more stable and gives good performance characteristics at transonic Mach regime**" [53].**

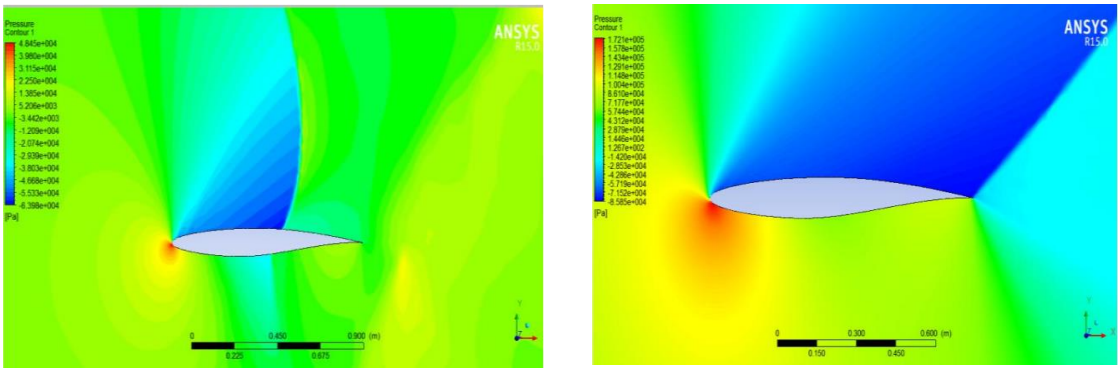

Figure 0-27 RAE2822 airfoil A)Pressure Variation across Normal Shock (M=0.8) B)Pressure Variation across Oblique Shock (M=1.2) [53].

- The Lift Coefficient is increasing with an increase in the angle of attack and decreases with an increase in Mach speed due to a rise in drag coefficient in the transonic region. This is in agreement with the airfoil theory.

- The Maximum Lift obtained in the Transonic airfoil with wedge profile is relatively less but is more stable at 15 degrees angle of attack which is near to the stall point.
- The Pressure, Velocity, Temperature & Turbulence Kinetic Energy Contours are found to be appropriate for corresponding Mach inputs and angles of attack.
- The ratio of Lift to Drag coefficient determines the airfoil performance which follows the same trend for both the foils.
- The Plots with respect to the angle of the attack show that the foil with wedge performs better up to an angle of attack of 10 degrees and drops on further increase in the angle of attack. This trend is continued upto Mach 1.
- The trend after Mach 1 shows that the foil with wedge gives better performance at all angles of attack.

July 1, 2017, by Sohail, Muhammad Umer, and Asad Islam [54]:

The study shows acceptable computational findings for the Transonic ONERA wing. The outcome is in good agreement with the experimental data. The good validation of the CFD result of the Cp distribution with experimental data is highly encouraging.

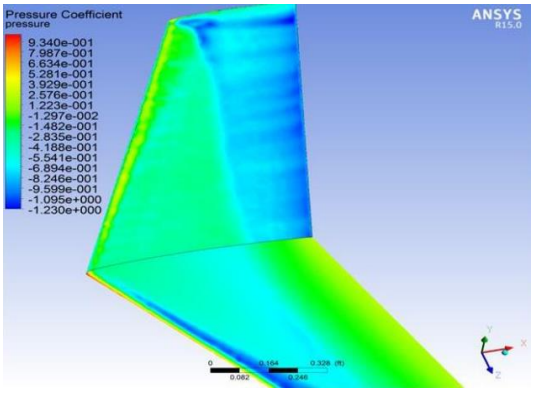

Figure 0-28 Cp contour with shock formation [54]

The ONERA M-6 wing is the ultimate validation case for peripheral flows in CFD. Because of its simple geometry linked with transonic flow complexities (i.e. local supersonic flow, shocks, and turbulent boundary layer separation). Transonic flow has been examined over the sweeping wing ONERA M-6. Computational analysis is used to determine the position of shock waves and the supersonic area on the wing. Since its approval as a validation example in several CFD research articles, it has effectively formed a standard for CFD codes. The Spallart Allmaras turbulence model was used to perform a 3D flow simulation on the ONERA M6 wing in Fluent. At an AOA of 3.06 degrees, with a

Reynolds number of 11.72×10^6 and a Mach of 0.8395, the flow was modeled as transonic and compressible. The resulting CFD findings will be evaluated against experimental data for the 1/5th spanwise location of the wing.

May 5, 2018 by D Koti, A Khan [55]

A grid independence analysis is conducted for the RAE 2822 airfoil at Mach 0.725 and Reynolds number 6.5 million. A study of three different grid sizes reveals that the results do not vary as the grid size is increased. The pressure coefficient plot over the airfoil surface for all three grids is identical. The lift and drag coefficient values for the three grids are also compared, revealing relatively low error. A comparison of pressure coefficient plots with experimental values (from reference **[56]**) indicates that the numerical results match the experimental data well, despite the fact that the shock location is predicted upstream of the experimental results.

The Pressure contour and Mach number contour clearly show the formation of a normal shock on the upper surface of the airfoil. The Mach number contour also shows the formation of local supersonic flow over the upper surface of the airfoil indicating the freestream Mach number to be over the critical Mach number. The velocity contour shows the thickening of the boundary layer aft of the shock wave indicating that any increase in flow conditions will lead to boundary layer separation **[55]**.

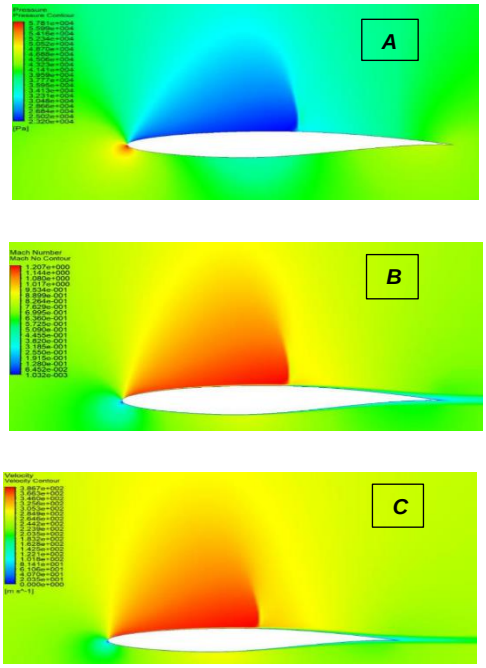

Figure 0-29 A) RAE2822 Pressure Contour

Table 1.Upstream flow parameters used in RANS simulations for the supercritical wing profile OAT15A [57].

Experimental	Turbulence closure	$T_{t\infty}$(K)	$P_{t\infty}$(Pa)
$M_{\infty\, exp} = 0.73$ $AOA_{exp} = 1.50°$ $Re_X = 3 \times 10^6$	RANS GLVY-RSM RANS LS $K-\varepsilon$	300 300	10^5 10^5
$M_{\infty\, exp} = 0.73$ $AOA_{exp} = 3°$ $Re_X = 3 \times 10^6$	RANS GLVY-RSM RANS LS $K-\varepsilon$	300 300	10^5 10^5
$M_{\infty\, exp} = 0.75$ $AOA_{exp} = 3°$ $Re_X = 3 \times 10^6$	RANS GLVY-RSM RANS LS $K-\varepsilon$	300 300	 10^5 10^5

June 28 by Valentin Bonnife [57]: This Ph.D. continues the work of Gerolymos and Vallet **[58]** on the creation of a sub-mesh model with the 7 transport equations and a second-order statistical closure. The objective is to employ Gerloymos-Lo-Vallet-Younis's **[59]** development of the second-order statistical closure to build a sub-mesh model with a control parameter that regulates the quantity of turbulent kinetic energy.

The suggested RANS/LES hybrid approach is based on Girimaji's **[60]** Partially Averaged Navier-Stokes method (PANS). It is incorporated to replicate the experiment performed at the Office National Etude et de Recherche Aérospatial (Onera) of the transonic Buffeting on the **OAT15A** wing profile or the shock-wave boundary layer interaction causes a self-sustaining motion on the top side of the airfoil under certain inflow circumstances. Reynolds Averaged Navier-Stokes cannot predict averaged fields because the large unsteadiness is nondeterministic, necessitating an LES method. According to the results, the proposed approach takes into consideration shock-wave motion.

September 19, 2018, by Eftekhari S and Al-Obaidi ASM [61]

Eftekhari S and Al-Obaidi ASM examined the aerodynamic properties of a NACA0012 wing shape at low Reynolds numbers and angles of attack ranging from 0° to 90° using numerical models, and the results are corroborated by Taylor's University subsonic wind tunnel measurements shown in **FIGURE I.35**. Further tests are carried out at low Reynold's numbers of 1×10^5, 2×10^5, and 3×10^5. The study's findings reveal a similar pattern for the lift and drag coefficients for all of the analyzed Reynolds numbers.

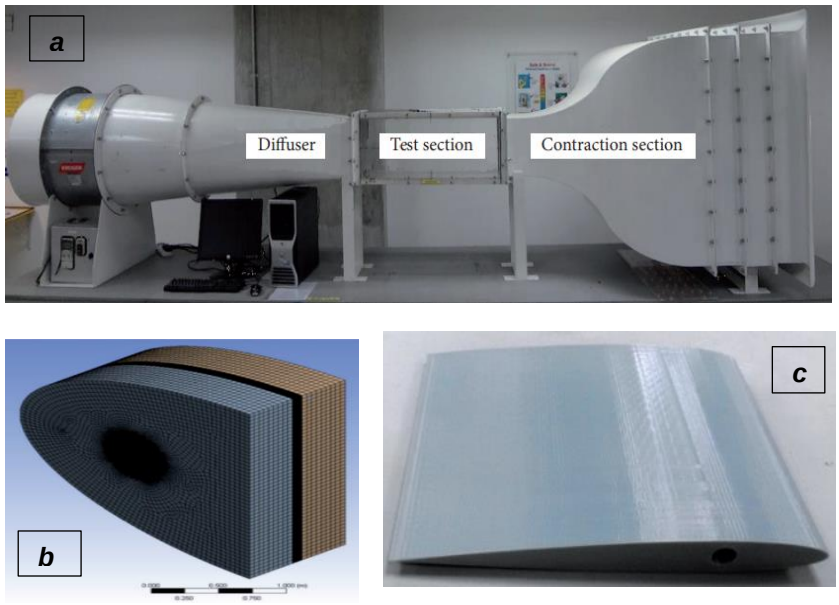

Figure 0-30 (a)Taylor's University subsonic wind tunnel (b) NACA0012 wing model (c) Mesh of the fluid domain [61].

The lift coefficient effect increases with angle of attack until it reaches its maximum at 32°, which is the stall angle. It is determined that as the angle of attack increases, the lift coefficient decreases until it reaches its minimum value of 90°. The drag force acting on the airfoil rises as the angle of attack increases, and the increase in drag force results in a transition from laminar to turbulent flow.

The drag force acting on the airfoil rises as the angle of attack increases, and the increase in drag force results in a transition from laminar to turbulent flow. As the turbulence increases, the flow begins to split from the airfoil surface due to turbulence-generated eddies.

As a result, the lift force provided by the wing is reduced while the drag force increases, resulting in poor wing performance.

July, 2020 by Arpit Aggarwal, Ralf Hartmann, Stefan Langer, and Tobias Leicht [62]:

This work conducts several experiments to explore the turbulent flow field and the spectral analysis of velocity component variations in the vortex-dominated flow field. Two vortices are formed above the wing in this configuration: the first in the front part of the wing, the Inboard Vortex (IBV), and the second on the third leading-edge region, the Mid-Vortex (MBV). Experiments using a Fast Response Aerodynamic Pressure Probe (FRAP) are carried out in this study to evaluate the spectral properties of velocity field variations for a triple delta wing design.

The flow field pattern is examined using Particle Image Velocimetry (PIV) data that shows the spatial distribution of turbulent kinetic energy. The focus of the spectrum study is to evaluate instability mechanisms linked to vortical flow shear layer and vortex bursting. The flow field findings for three distinct cross sections are shown at $\propto = [16°, 24°, 32°]$. There is a vortex development of inboard vortex (IBV) and midboard vortex (MBV) at $\propto = 16°$. (MBV).

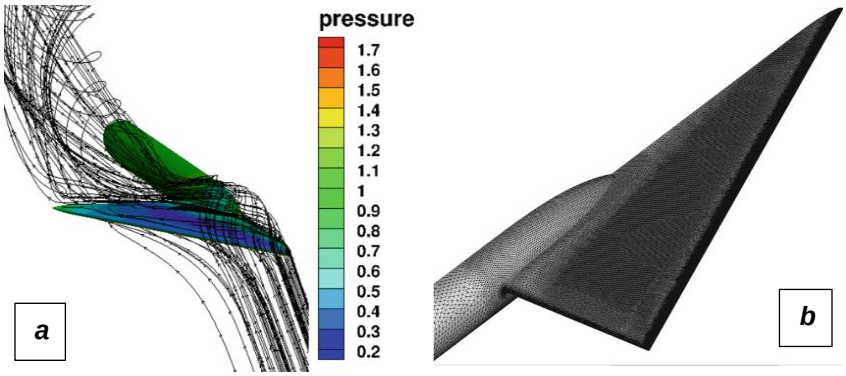

Figure 0-31 (a) Pressure distribution with streamlines (b) Delta wing with attached sting [62].

Figure a) Pressure distribution with streamlines (b) Delta wing with attached sting [62].

July 1, 2021, by Yuanjing Wang, Dawei Liu, Xin Xu, and Guoshuai Li [63]:

The effects of the Reynolds number on the aerodynamic properties of a transport aircraft are carefully investigated using cryogenic wind tunnel testing and CFD technologies. The ETW wind tunnel data reveal that in wind tunnel testing, the aeroelastic deformation of the supercritical wing has a significant impact on aerodynamic properties in the presence of a shock wave, which may even exceed the effect of the Reynolds number. Furthermore, the transition zone can increase the stability and repeatability of wind tunnel data and, to some degree, simulate in-flight transition position; nevertheless, it cannot model boundary layer thickness and evolution on the supercritical wing surface.

The wing deformation effect is adjusted in this work using in-house developed CFD software confirmed by wind tunnel data, and the transition zone is removed when the test Reynolds number exceeds15×10^6.

When the ETW wind tunnel test data and numerical CFD results are combined, it is possible to conclude that the Reynolds number has a small effect on the aerodynamic characteristics of the supercritical wing when the shock wave is absent, but dramatic Reynolds number effects can be found when the shock wave is present.

August 2021 by Dr. Vinayaka N, Akshaya C, Praveena BA, Praveen Kumar UB, Marulasiddeshi HB [64]:

This research focuses on the influence of turbulence intensity on airfoils in the transonic regime at varied attack angles (AoA). A supercritical airfoil is computationally examined at 2% and 10% turbulence intensity, Mach 0.8 and Mach 0.9 at 0° and 5° AoA. To solve the issue numerically, the Computational Fluid Dynamics approach is applied to the SC20412 airfoil to understand the airfoil's behavior at the flow regime of transonic at different boundary conditions to predict the airfoil's and shock waves' behavior. The conclusion obtained from this case study is presented below.

- The airfoil becomes inactive at Mach 0.9 due to its decreased C_L.
- As the turbulence intensity increase, the normal shock wave formed on the upper surface moves away from the LE.
- Formation of shock wave on both surfaces of airfoil leads to increase in drag and decrease in lift.
- The position of shock wave on surfaces of airfoil depends on Mach number, AoA, and turbulence intensity.
- Flow separation is observed as the AoA is increased. There was no flow separation at Mach 0.9, 50 AoA.

March 2022 by Bing Han, Min Xu, Guoguang Chen, et al. [65]

A well-validated delayed detached eddy simulation technique was used to explore the transonic buffet over a prescribed-pitching OAT15A airfoil. The computational method was validated by comparing the results on the fixed airfoil with Jacquin's experiments as well as other computational results in previous studies. The current method effectively replicated self-sustaining shock wave oscillations. According to the computational results, the amplitude of the lift variations in the pitching case is almost six times that of the stationary case.

I.8.4. Control Surfaces

July 1, 1920, by Prandtl, Ludwig [66] The flow of a fluid around an infinite span lifting surface is investigated in terms of the presence of vortexes in the current. There is a discussion on the general basis of lifting surface theory and the general theory of permanent flow. There are formulas for determining the influence of aspect ratio that can be applied to all wings, regardless of plane form.

January 1, 1947, by Racisz, Stanley F [67] An investigation has been made in the Langley two-dimensional Low-turbulence tunnel to determine the highest maximum Lift configurations (ideal configurations)of a 0.35-chord slotted flap on a NACA 65(112)A111 (approx.) airfoil section. The scale effects on the aerodynamic characteristics were determined for Reynolds numbers ranging from 2.4×10^6 to approximately 25×10^6. Increasing the Reynolds number from 2.4×10^6 to 9×10^6 decreased the flap deflection for the highest maximum lift from 45° to 40° and 35° (deflections 40° and 35° gave some maximum lift).

When the Reynolds number was increased, the flap location for the highest maximum Lift moved upward roughly 1% of the airfoil chord for flap deflections of 35° and 40°, and rearward for a flap deflection of 35°.The flap configuration with the center or the riap Leading-edge radius Located at 1.98 percent chord behind and 3.21 percent chord below the slot lip at a flap deflection of 35° was the optimum configuration, A maximum increase of only 0,1 in the value of the maximum section lift coefficient was obtained at a Reynolds number of 9×10^6 by Shifting the flap from the position giving the highest maximum lift at a Reynolds number of 2.4×10^6 **[67].**

In general, raising the Reynolds number delayed the stall and created a more gradual stall for both the flap-retracted and flap-deflected designs. The maximum section lift coefficients for the flap-retracted configuration increased as the Reynolds number increased to 18×10^6 and then slightly decreased with a further increase in Reynolds number,

while the coefficients for the flap-deflected configuration increased as the Reynolds number increased to $13 \times 10^6$and then decreased slightly.

December 16, 1947, by Erickson, Albert L, Stephenson, and Jack D [68]

This report summarizes the findings of a study of shock movement on a three-dimensional wing with and without aileron flutter. Several adjustments and variations to the wing and control are included in the research. A preliminary technique of analysis is established based on these data and some fundamental ideas of the cause and mechanism of " transonic flutter."

The test results are provided, followed by a general discussion and design recommendations. It is demonstrated that transonic flutter is induced by a lag in the build-up of the resultant hinge moment when the velocity over the wing increases sufficiently to delay the change in circulation after control displacement. Under these conditions, the hinge moment operates in the direction of motion for more than half a cycle, allowing for a constant oscillation. According to the results of the analysis, controls must be designed with a large mass moment of inertial or with a high degree of irreversibility if damping is not applied. When a mechanical restraining influence is present in the control system, attention must be given in its design to ensure that the natural frequency of the system does not fall between one-half the aerodynamic frequency and the aerodynamic frequency.

April 25, 1950 by H. Kurt Strass [69]

The Langley Pilotless Aircraft Research Division used rocket-powered test vehicles to investigate the effect of spanwise aileron location on the rolling effectiveness of 0.2-chord plain faired ailerons on untapered wing plan forms with 0° and 45° sweep, NACA 65A009 airfoil sections, and an aspect ratio of 3.7 at subsonic, transonic, and supersonic speeds. Furthermore, drag data for all setups covered in this study are supplied. When the impacts of the control area and moment arm were considered, the findings reveal that for unswept wings, there was little or no difference

in rolling efficacy with spanwise aileron position of the particular aileron type studied.

However, spanwise control location on wings with a 45° sweep is an extremely important consideration because the inboard half-span aileron was significantly more effective than the outboard half-span aileron throughout the entire speed range tested and proportionally more effective than the full-span aileron when the effects of control area and moment arm were considered. At a Mach number of 0.7, the inboard aileron provided around 60% of the full-span effectiveness, with the proportion gradually rising until at a Mach number of 1.5 and higher, the inboard aileron was nearly as effective as the full-span design. Furthermore, statistics for a shielded horn balance connected to the outboard half-span aileron arrangement for both the swept and unswept instances are provided. There was little difference in rolling performance.

September 1, 1952, by Wood, George P [70] Interferometry was used to investigate several characteristics of transonic flow around the front regions of wedge profiles. The two types of flow patterns that occur at the leading edge of a wedge at an angle of attack were measured. The expansion of the supersonic area was also seen at a sharp convex corner produced by two flat surfaces. The pressure drag coefficient of 14.5 deg. semiangle wedge was measured at Mach numbers of 0.768, 0.819, and 0.854 and found to be comparable with those of smaller angle wedges when plotted using the transonic similarity law. The flow behind an experimentally determined sonic line was computed using the characteristics technique, and the predicted flow field was compared to the measured flow field. The precision with which the sonic line must be located in order to accurately represent the pressure distribution on the surface behind it was calculated.

June 1976, by Lovell, D. A. [71] The effects of adding a Fowler flap and spoiler to an advanced general aviation wing were investigated at the Langley Research Center V/STOL tunnel.

The wing was tested without a fuselage or empennage, and it was outfitted with three-quarter-span Fowler flaps and half-span spoilers. When the flaps were deflected, the spoilers were hinged at the 70% chord point and vented. Static longitudinal and lateral aerodynamic data were collected for various flap deflections and locations, spoiler geometries, and vent-lip geometries throughout an angle-of-attack range of -8° to 22°.

In general, the efficacy of the spoiler rises with increasing angle of attack, with increasing flap deflections, and is impacted by vent-lip geometry. Furthermore, the statistics demonstrate that in the three-dimensional case, some two-dimensional impacts on spoiler efficacy are reduced.

The results also show that the lift coefficient increases significantly when the Fowler flaps are deflected, when the flap was fully deflected, the maximum wing lift coefficient increased by about 96%.

September 1984 By Consigny, H., A. Gravelle [72]

Wind tunnel studies were conducted to assess the unstable efficiency of a spoiler-like control surface. The examination of oscillations of the spoiler was the focus of the initial series of tests. Several factors were studied to see how they affected the amplitude and phase of oscillatory pressures and lift. It was demonstrated, in particular, that the findings are highly dependent on the freestream Mach number, spoiler mean deflection, and frequency of oscillation. In the second series of studies, transient pressures and transient lift were measured in response to a quick and large shift in spoiler angle.

The experimental results show the complexity of the flow pattern associated with the motion of this form of control, as well as the presence of large unsteady and significant nonlinear effects, the possibility of a control unsteady effectiveness reversal was also seen. Such characteristics would almost probably complicate the design of a feedback control system.

May-June 1994 by Storms, Bruce L., and Cory S. Jang [73]

Two lift-enhancing devices were studied experimentally on a two-dimensional single-element airfoil, and the following findings were reached:

- At low-to-moderate lift coefficients, the Gurney flap may greatly boost the lift of a single-element airfoil while causing only a little increase in drag.
- To reduce drag during the cruise, the small split-flap arrangement with a hinge line forward of the trailing edge can be used, offering performance equivalent to the Gurney flap.
- Vortex generators can delay flow separation and raise the maximum lift coefficient on an airfoil that suffers trailing edge stall. However, because of the significant drag increase associated with these devices, they must be incorporated into a high-lift system by being placed towards the leading edge of the flaps and/or the primary element where they will be concealed during the cruise.
- The Gurney flap and vortex generators can be used in concert to produce a higher lift increase than either device alone.

March-April 2000 by D Jeffrey, X Zhang, DW Hurst [74]

The time-averaged flow downstream of a Gurney flap is composed of two counter-rotating vortex, while the instantaneous flow structure is composed of a wake of alternatively shed vortices. The frequency of shedding is proportional to the height of the Gurney flap and the thickness of the boundary layer at the trailing edge of the aerofoil. The vortex shedding causes an increase in base suction, which is nearly constant across the downstream face of the Gumey flap and is linked to the formation length of the recirculation zone.

The upstream face slows the flow in the same way as a flat plate immersed in a turbulent boundary layer does. As a result, the Gurney flap creates a pressure differential at the trailing edge, and this pressure difference generates an increase in overall circulation.

March 2002 by Heller, G., P. Kreuzer, and S. Dirmeier [75]

The development and integration of a new high-performance wingtip device for transonic aircraft is a comparison of numerous wingtip device types which revealed that a novel wingtip architecture provides the optimum compromise to meet the difficult criteria. This new Shark wingtip family's design idea is revealed. The possibility for improved aerodynamic performance is highlighted in the findings of computational and experimental investigations. The benefits of the Shark family are demonstrated by discussing integration effects, namely structural design concerns and features of aircraft controllability.

June 7, 2,006 by Fillola, Guillaume [76]

The purpose of this thesis is to assess the efficacy of numerical approaches based on RANS equations to predict the effects of moving surface deflections and the prediction of aerodynamic forces and hinge moments caused by the deployment of ailerons and spoilers which is an important step in the entire design process of an aircraft since it has a large influence on the final weight. It is based on the findings of two research. The first step is to describe the behavior of a supercritical profile with a spoiler or an aileron. A soufflerie test program is thus carried out in order to provide a platform for the validation of three-dimensional numerical models that include the tunnel walls. The second study's goal is to apply CFD to industrial designs of a fuselage/wing with a guided rudder. ""Chimère and Patched Grid" techniques are used in this approach to help with the meshing process. A mesh deformation approach is also created to quickly simulate multiple aileron deflections.

June 30, 2011 by A Ragheb, M Selig [77]

This work was motivated by the following objectives: decreasing the cut-in wind speed, increasing the transportability of large wind turbine blades, and developing the ability to raise the spar cap spacing to allow for structural optimization of the blades. The main purpose of this research was to create conceptual multi-element airfoil designs that would improve

the aerodynamic performance of a wind turbine blade's inboard area. Increasing the lift coefficient of a wind turbine blade's inboard region assists in starting the wind turbine at lower speeds and allows the turbine to produce its rated power at lower wind speeds, and these improvements would in turn increase the power output, increase the capacity factor, and open up new locations for wind turbines that would otherwise be unsuitable for wind turbine placement.

A computational research was conducted to evaluate possible multi-element airfoil configurations that would act as aerodynamic protection for an assumed spar cap geometry based on the DU 00-W-401 blade root airfoil shape. Using an inviscid multipoint inverse airfoil design method, seven multi-element airfoil shapes with varied combinations of flaps, slats, and struts were designed and optimized. The airfoil variants were then tested at Reynolds values representative of a utility-scale wind turbine. The airfoil versions were then evaluated at Reynolds numbers that corresponded to a utility-scale wind turbine. All of these designs produced much greater lift-to-drag ratios and lift coefficients than the baseline DU 00-W-401 airfoil, with Cl/Cdmax increases of up to 82 percent.

May 3, 2014, by Hossain, Md Amzad, Mohammad Mashud, and Khondakar Wahida Taskin [78]

The main objective of this project is to investigate the physics of flow over an airfoil without and with a spoiler at various angles. This investigation will reveal how to stall point decreases with spoiler angle change. The variation of the lift and drag components of force may be examined for the spoiler which is placed at 5 percent of the chord and the spoiler length is 10 percent of the chord at various angle values (2.5°, 5°, 7.5°, 10°, 12° degrees are held in design).

The following are the problem specifications: build geometry in GAMBIT, mesh geometry in GAMBIT, specify boundary types in GAMBIT, set up the problem in FLUENT, solve the problem, and evaluate the results. This analysis revealed that lift is reduced while drag is increased, demonstrating the frequent nature of spoilers, and it can be concluded

that the numerical experiment of the NACA 2415 airfoil having a spoiler on five different angles has been identical to the main function of the spoiler.

June 26, 2015, by Chia Min Leong, Erica Cruz, Dan Clingman, and Michael Amitay (Experimental Study) [79]

The interaction of both static and dynamic VG with a laminar boundary layer was investigated in this work using surface oil flow visualization and SPIV. The presence of five main vortical structures was revealed by oil flow visualization results: the main vortex caused by the VG, a primary and secondary horseshoe vortex caused by the roll-up of the incoming boundary layer upstream, and two induced vortices caused by the presence of these horseshoe vortices. The presence of these vortical structures was verified by SPIV data. It reveals that the vortices observed were unstable under small amplitude motion, despite the fact that the horseshoe vortices looked to be more sensitive to periodic motion since they formed and faded constantly during the oscillation cycle.

A dynamic vortex generator (**DVG**) was designed with the purpose of reducing any additional drag that may occur while the DVG is not in use and also investigating the effect of sinusoidally oscillating the DVG in the wall-normal direction on the flow field.

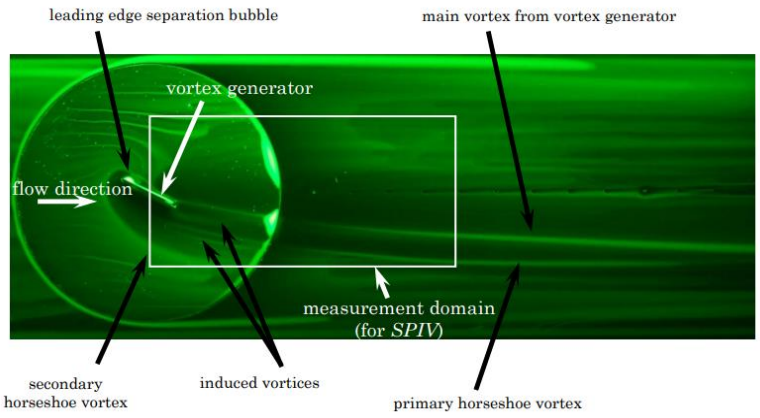

Figure 0-32 Surface oil flow visualization for flow over the static VG placed at a skew angle of 27°. Flow is left-to-right. The primary flow features present on the surface are labeled. The measurement domain selected for SPIV measurement is also shown [79].

June 26, 2015, by R Cummings, D Clingman, O Sahni (Numerical Study) [80]

A VG was put in a laminar boundary layer flow and its interactions with the cross-flow were investigated at various actuation parameters such as height/amplitude and frequency. In the case of the SVG, two vortices form in the wake: the main vortex and the horseshoe vortex. In the DVG cases, the motion of the VG significantly changes the flow field in the wake and these changes depend on the actuation amplitude and frequency.

According to these investigations, DVG is a more effective flow control device than SVG. However, the influence of various DVG settings on cross-flow is not well understood. The purpose of this study is to look at the impacts of the DVG's actuation amplitude and frequency. The VG was set at an angle of 18 degrees. The mean height was set at the local boundary layer thickness ($\boldsymbol{\delta}$), and the corresponding Reynolds number ($\boldsymbol{Re_\delta}$) at the VG position was around 2000.

June 17, 2016, by T Rice, R Cummings, D Clingman, O Sahni (Experimental and Numerical Investigation) [81]

The influence of VGs on flow reattachment over the flap was studied experimentally and numerically on a modified NACA 0012 airfoil with flap deflections of 20° and 30°.

The unsteady Reynolds averaged Navier-Stokes (URANS) equations and the Spalart-Allmaras turbulence model were used in the simulations by taking into consideration flap deflections of 20° and 30° while the experiments focused on the flap deflection of 20. For a flap deflection of 30, both the baseline and SVG cases were simulated, whereas for a flap deflection of 20, only the baseline case was simulated.

At two different heights, static vortex generators were examined. The SVGs resulted in a considerable increase in the local suction peak near the hinge line at both heights. SVGs increased circulation around the airfoil model by reducing the extent of flow separation over the flap.

January (3-7), 2022, by Xiong, Juntao, Nhan T. Nguyen, and Robert E. Bartels [82]

Aerodynamic optimization analysis of the Mach 0.8 Transonic Truss-Braced Wing (**TTBW**) aircraft with Variable Camber Continuous Trailing Edge Flap is presented in this work. The **VCCTEF** is an innovative wing shape control concept designed to increase aircraft aerodynamic efficiency. Drag reduction investigations are carried out for two alternative VCCTEF designs, with six and ten spanwise sections. In the design of the Mach 0.8 TTBW aircraft, a basic VCCTEF actuator weight model is employed to account for the weight penalty of the actuator. For quick aerodynamic performance assessments, a vortex-lattice model of the Mach 0.8 TTBW aircraft is created including transonic small disturbance, integrated boundary-layer, and airfoil interference corrections.

The optimization results show that the 6-spanwise sections VCCTEF provides a relatively better solution for drag reduction when the actuator weight penalty is considered. A high-fidelity CFD solver FUN3D is used to verify the VCCTEF optimization design.

CHAPTER

MATHEMATICAL MODELING II

CHAPTER CONTENT

II.1 Fundamental equation of instantaneous compressible fluid…..……
II.2 Reynolds-Averaged Navier-Stokes equations (**RANS**)……..….
II.3 Turbulence Modeling……...…….…….…….
II.4 Wall Treatments …….

OUTLINE

In this chapter, the equations that are allowed for the performance of the gas under consideration will be defined. We start with the law of the state that allows relating state variables, which describe the state of matter under a given set of physical conditions, such as pressure, volume, temperature, or internal energy.

The fundamental rule for viscous fluid is then retained by recalling the formulation of the tensor of the constraints inside the fluid owing to pressure and velocity gradients. We will start with the assumption of a continuous medium consisting of compressible and viscous fluid. It is assumed that the fluid under consideration validates the Navier-Stokes equations, which are supplemented with classical constitutive laws and the ideal gas state law. Furthermore, it is assumed that the fluid's density is low enough to allow gravity's effects to be ignored (non-heavy fluid hypothesis).

II.1 Fundamental equations of instantaneous compressible fluids

For a compressible, viscous, and supposedly ideal fluid, the fundamental equations of flow can be given by the conservation laws.

- **The continuity equation is:**

$$\frac{\partial \rho}{\partial t} + \frac{\partial}{\partial x_j}(\rho u_j) = 0 \qquad \textbf{(II.1)}$$

Where:

- ρ is the fluid density,
- u_j is the j component of the velocity vector.

And the conservation of momentum equation is:

$$\frac{\partial}{\partial t}(\rho u_i) + \frac{\partial}{\partial x_j}(\rho u_i u_j) = \frac{\partial}{\partial x_j}(-P\delta_{ij} + \tau_{ij}) \qquad \textbf{(II.2)}$$

Where:

- **P** is the static pressure,
- δ_{ij} is the the Kronecker tensor,
- τ_{ij} is the viscous stress tensor.

- **Conservation of energy equation:**

$$\frac{\partial}{\partial t}(\rho E) + \frac{\partial}{\partial x_j}\left[u_j(\rho E + P)\right] = -\frac{\partial}{\partial x_j} q_j + \frac{\partial}{\partial x_j}(u_i \tau_{ij}) \qquad \textbf{(II.3)}$$

Where:

- q_j is the heat flow in the **j** direction,
- **E** is the total energy per unit mass**,** which is expressed by the following relationship:

$$E = e + \frac{1}{2} u_k u_k \qquad \textbf{(II.4)}$$

- **Equation of state of an ideal gas:**

$$P = \rho RT \qquad C_p - C_v = r \qquad \gamma = \frac{C_p}{C_v} \qquad \textbf{(II.5)}$$

Where:

- γ being the particular ideal gas constant,
- C_p and C_v respectively represent the specific heats at constant pressure and constant volume.

For a supposedly Newtonian fluid, the viscous stress tensor τ_{ij} takes the following form:

$$\tau_{ij} = \mu\left(\frac{\partial u_i}{\partial x_j} + \frac{\partial u_j}{\partial x_i}\right) + \lambda\delta_{ij}\left(\frac{\partial u_i}{\partial x_j}\right) \qquad \textbf{(II.6)}$$

In which μ and λ are related by the Stokes hypothesis: $3\lambda + 2\mu = 0$

- The heat flow q_j per unit area as a function of temperature is written as follows:

$$q_j = -k\frac{\partial T}{\partial x_j} \qquad \textbf{(II.7)}$$

  - **K** is the thermal conductivity which is expressed as a function of the dynamic viscosity by the Prandtl number P_r**:**

$$P_r = \frac{\mu C_p}{k} = \gamma\frac{\mu C_v}{k} \qquad \textbf{(II.8)}$$

- Assuming that the fluid is calorically perfect (internal energy $e = C_v T$ and enthalpy $h = C_p T$), the heat flow can be written:

$$q_j = -k\frac{\partial T}{\partial x_j} = -\frac{\mu}{P_r}\frac{\partial h}{\partial x_j} \qquad \textbf{(II.9)}$$

- The dynamic viscosity is given for the temperature range studied,

by the following Sutherland law (used by FLUENT):

$$\mu = \mu_0\sqrt{\frac{T}{T_0}}\left(\frac{1 + S/T_0}{1 + S/T}\right) \qquad \textbf{(II.10)}$$

Where $\mu_0 = 1.78938\ 10^{-5}\text{kg}.m^{-1}.s^{-1}$ is the viscosity of the fluid at the reference temperature $T_0 = 288K$ and **S** is a fixed constant for the air at **110 K**.

II.2 Reynolds-Averaged Navier-Stokes equations (RANS)

An instantaneous quantity $\boldsymbol{\phi}$ of the flow can be decomposed according to Reynolds into an average part $\bar{\boldsymbol{\phi}}$and a fluctuating part $\boldsymbol{\phi'}$

$$\boldsymbol{\phi = \bar{\phi} + \phi' \; avec \; \bar{\phi} = \lim_{\Delta T \to \infty} \left(\frac{1}{\Delta t}\right) \int_{t_0}^{t_0+\Delta t} \phi(t) dt} \qquad \textbf{(II.11)}$$

Averaged Navier-Stokes equations may contain additional terms such as Reynolds stress tensors. These averaged equations are simplified for compressible flows using Favre's formula, which consists in decomposing the instantaneous quantity, and then we will have:

$$\boldsymbol{\widetilde{u}_i = \frac{\overline{\rho u_i}}{\bar{\rho}} = \frac{1}{\bar{\rho}} \lim_{T \to \infty} \frac{1}{\mathrm{T}} \int_t^{t+\mathrm{T}} \rho(x,\tau)\, u_i(x,\tau) d\tau} \qquad \textbf{(II.12)}$$

Since Favre's formula removes density fluctuations, it is considered a mathematical simplification. The quantities of the fluid according to the derivation of these Favre averaged equations (Favre-averaged Navier-Stokes equations) and their discretizations based on the technique of finite volumes, as utilized by the code FLUENT are written by:

$$\begin{cases} \boldsymbol{u_i = \widetilde{u}_i + u_i''} \\ \boldsymbol{\rho = \bar{\rho} + \rho'} \\ \boldsymbol{p = \bar{p} + p'} \\ \boldsymbol{e = \tilde{e}_i + e_i''} \\ \boldsymbol{h = \widetilde{h} + h''} \end{cases} \qquad \textbf{(II.13)}$$

By replacing the previous quantities in the Navier-Stokes equations, we obtain the following formulas:

- **The continuity equation is then**

$$\boldsymbol{\frac{\partial \bar{\rho}}{\partial t} + \frac{\partial}{\partial x_j}(\bar{\rho}\widetilde{u}_j) = 0} \qquad \textbf{(II.14)}$$

- **The momentum equation is:**

$$\frac{\partial}{\partial t}(\bar{\rho}\tilde{u}_i) + \frac{\partial}{\partial x_j}(\bar{\rho}\tilde{u}_i\tilde{u}_j) = -\frac{\partial \bar{p}}{\partial x_j} + \frac{\partial}{\partial x_j}\left[\bar{\mu}\left(\frac{\partial \tilde{u}_i}{\partial x_j} + \frac{\partial \tilde{u}_j}{\partial x_i} - \frac{2}{3}\frac{\partial \tilde{u}_k}{\partial x_k}\delta_{ij}\right)\right] + \frac{\partial}{\partial x_j}\left(-\bar{\rho}\overline{u_i'' u_j''}\right) \quad \textbf{(II.15)}$$

Where the term $-\bar{\rho}\overline{u_i'' u_j''}$ stands for Reynolds stresses (turbulent flows of momentum) which must be modeled in order to complete the closure of the system of equations.

The turbulence models in the FLUENT code use Boussinesq's concept of turbulent viscosity, which assumes that the Reynolds stress is a linear function of strain ratio:

$$-\bar{\rho}\overline{u_i'' u_j''} = \mu_t\left(\frac{\partial \tilde{u}_i}{\partial x_j} + \frac{\partial \tilde{u}_j}{\partial x_i} - \frac{2}{3}\frac{\partial \tilde{u}_k}{\partial x_k}\delta_{ij}\right) - \frac{2}{3}\bar{\rho}k\delta_{ij} \quad \textbf{(II.16)}$$

Where μ_t is the turbulent viscosity and **k** is the turbulent energy given by the following formula:

$$k = \frac{1}{2}\overline{u_k'' u_k''} \quad \textbf{(II.17)}$$

The averaged FANS equations (Favre-averaged Navier-Stokes equations) are obtained by replacing the momentum equation with the continuity equation:

$$\frac{\partial}{\partial t}(\bar{\rho}\tilde{u}_i) + \frac{\partial}{\partial x_j}(\bar{\rho}\tilde{u}_i\tilde{u}_j) = -\frac{\partial \bar{p}}{\partial x_j} + \frac{\partial}{\partial x_j}\left[\overline{(\mu} + \mu_t)\left(\frac{\partial \tilde{u}_i}{\partial x_j} + \frac{\partial \tilde{u}_j}{\partial x_i} - \frac{2}{3}\frac{\partial \tilde{u}_k}{\partial x_k}\delta_{ij}\right)\right] - \frac{2}{3}\frac{\partial}{\partial x_j}(-\bar{\rho}k) \quad \textbf{(II.18)}$$

- **For the energy equation**

$$\frac{\partial}{\partial t}(\bar{\rho}\tilde{h}) + \frac{\partial}{\partial x_j}(\bar{\rho}\tilde{u}_j\tilde{h}) = \frac{\partial \bar{p}}{\partial x_j} + \tilde{u}_j\frac{\partial \bar{p}}{\partial x_j} + \bar{\tau}_{ij}\frac{\partial \tilde{u}_i}{\partial x_j} + \overline{\tau'_{ij}\frac{\partial u''_i}{\partial x_j}} + \frac{\partial}{\partial x_j}\left(k\frac{\partial T}{\partial x_j}\right) - \frac{\partial}{\partial x_j}\bar{\rho}u''_j h'' \quad \textbf{(II.19)}$$

- Additional terms appear:

The first term is the fluctuating enthalpy, it can be written in the following form:

$$\frac{\partial}{\partial x_j}\bar{\rho}u''_j h'' = \Gamma_t\frac{\partial \tilde{h}}{\partial x_j} = C_p\Gamma_t\frac{\partial T}{\partial x} = C_p\frac{\mu_t}{Pr_t}\frac{\partial T}{\partial x_j} \quad \textbf{(II.20)}$$

Where:

- Γ_t is the turbulent diffusivity which is expressed as follows: $\Gamma_t = \frac{\mu_t}{Pr_t}$
- Pr_t is the turbulent Prandtl number fixed at 0.9.

The second term is the turbulent energy dissipation ratio ε which depends on the choice of the turbulence model. The dissipation ratio is obtained by solving the equation for ε.

- For the $k-\varepsilon$ model, this term is defined by:

$$\overline{\tau'_{ij}\frac{\partial u''_i}{\partial x_j}} = \bar{\rho}\varepsilon \quad \textbf{(II.21)}$$

If the equation of **ε** is not solved (as in the **Balwin-Lomax** model), it is expressed as follows:

$$\overline{\tau'_{ij}\frac{\partial u''_i}{\partial x_j}} = \mu_t\frac{\partial \tilde{u}_i}{\partial x_j}\left(\frac{\partial \tilde{u}_i}{\partial x_j} + \frac{\partial \tilde{u}_j}{\partial x_i} - \frac{2}{3}\frac{\partial \tilde{u}_k}{\partial x_k}\delta_{ij}\right) \quad \textbf{(II.22)}$$

- The averaged state equation is given by the following formula:

$$p = \bar{\rho}r\tilde{T} \quad \textbf{(II.23)}$$

II.3 Turbulence Modeling

II.3.1 Introduction

Over a century ago, why did **Osborne Reynolds** propose decomposing instantaneous flow quantities into two components? When we presented the incompressible laminar flow with constant viscosity, the Navier stokes equation governs laminar flow, which is derived from momentum conservation in three dimensions, where we have an x, y, and z component, and because we have three variables and three equations, we can solve this and find a specific and accurate governing equation for basic laminar flows under known boundary conditions, much like we learned in the differential equation. However, when the turbulent flow is included, engineers and mathematicians do not find it as easy as the laminar case, and they are still working to solve the Navier stokes equation by conceiving it as a Reynolds averaged Navier-stokes equation. To do so and progress to turbulent flow, we will need to apply Reynold's decomposition, which decomposes the velocity "**u**" stated in the Navier-Stokes equation into two components, an average velocity and a fluctuation that indicates a form of turbulent intensity. The fact that we take equations with velocities and substitute two variables for each time there is a velocity leads to a much more complicated **Reynolds averaged Navier-Stokes** equation.

When we compare the x-momentum of laminar flow to the x-momentum of turbulent flow, we can see that the first one was a solvable equation that included gravity, pressure gradient, viscosity, and acceleration, as well as the three variables of velocity, in three different directions. Yet, when turbulence is introduced, decomposition takes place. As previously stated, it is characterized as Reynolds' decomposition, which results in a difficult mathematical problem with more variables than equations (averages of variables, fluctuations, and the average of fluctuations). Now since we have an unsolvable issue, new equations are required to close the system, which is why turbulence models are used.

As early as **1910**, **Taylor** (**1913**) and **Prandtl** (**1925**) carried out the first successful calculations of turbulent flow, introducing for the first time the concept of Mixing-length[1] to determine the viscosity of turbulence. Afterward, **Von Karman** (**1930**), Taylor (**1930**), and others contributed significantly to the type of Mixing-length models (**1932**). In which they always consider turbulence viscosity to be the only function of local parameters.

Prandtl (**1945**) then introduced **k-l** models (**k:** kinetic energy of turbulence which is determined from a transport equation and **l:** it is a length scale determined algebraically). These models have been confirmed for relatively simple flow configurations.

Following **the Stanford Conference** (**1968**), **Klin et al** (**1969**) determined that a simple turbulence model may govern the two-dimensional boundary layer. This is incompatible with Tillman-type flow, which necessitates additional intermediate computations. The challenges of turbulence modeling discussed at the **1981 Stanford conference** are more complicated than those covered at the **1968** conference. The most recent conference provided a good synthesis of modeling and current numerical methods.

II.3.2. Turbulence Models

Modeling the turbulent flow is so complicated for complex scenarios like flow past an aerofoil, and a lot of it has to do with the turbulent eddies, the main challenge is capturing the wide range of length scales associated with the turbulent eddies.

Large eddies contain a lot of kinetic energy and over time the energy in these large eddies feeds the creation of progressively smaller eddies until at the smallest scale, the turbulent energy is minuscule eddies dissipates as heat due to frictional forces caused by the fluid viscosity, that means the energy in the flow is cascading from the largest to the smallest eddies, and so this concept is called **“ The energy cascade”** this term was summarised by the physicist **Lewis Fry Richardson**, who wrote:

"Big whirls have little whirls that feed on their velocity, and little whirls have lesser whirls, and so on to viscosity" **[84]**

Because of this behavior, turbulence involves a huge range of length and time scales that makes analysis of turbulent flow very complex and probably the most significant challenge facing the field of Fluid Mechanics because we can't accurately describe the fluid behavior of a flow past an aerofoil using simple equations. So to analyze the flow we have to use either experimentation or numerical methods, or a combination of the two. Modeling flow using numerical methods in the field of **Computational Fluid Dynamics**, which we will go through in-depth in the following chapter.

[1]Prandtl’s **mixing length** theory, which is known as simple modeling of Reynolds stress, the random movement of a fluid parcel is considered based on the analogy with the mean free path of a molecular in thermodynamics **[83]**

When we model the fluid domain around the aerofoil as a mesh of discrete elements, define boundary conditions and fluid properties, and apply an appropriate assessment technique to find a solution. There are three main techniques which are **DNS**, **LES,** and **RANS** techniques, and differ mainly in how they treat turbulence on these different scales to simulate flow in **CFD**.

II.3.2.1. Direct Numerical Simulation

DNS is very computationally expensive, it is not a practical solution for the vast majority of fluid flow problems. It involves solving the Navier-Stokes equations down to even the smallest scales, and so all turbulent eddies are fully resolved, meaning that they are simulated explicitly.

II.3.2.2. Large Eddy Simulation

LES is much less computationally expensive than DNS. This technique resolves the large-scale eddies explicitly, but small-scale eddies are filtered out and are modeled using what is known as a **subgrid-scale** model.

II.3.2.3. RANS technique

The Reynolds-Averaged Navier-Stokes technique is the least computationally expensive of the three techniques. This is a time-averaged method that doesn't resolve eddies explicitly at all. Instead, it models the effect of eddies using the concept of turbulent viscosity.

Several different turbulence models exist, like the **Spalart-Allamaras**, **K-Epsilon,** or **K-Omega** models, with different models being better suited to different problem types. They are organized as follows:

- One Equation Model Spalart-Allmaras equation.
- Two Equations Models are:
  - Standard $\boldsymbol{k-\varepsilon}$ model,
  - Renormalization-group **(RNG)** $\boldsymbol{k-\varepsilon}$,
  - Realizable $\boldsymbol{k-\varepsilon}$**,**
  - $\boldsymbol{k-\omega}$ Model,
  - $\boldsymbol{k-\omega\ SST}$ Model.
- Five Equations Reynolds stress model (**RSM**).

The following table summarizes the benefits and description of various eddy viscosity RANS models, starting from the 'zero' equation mixing length model to the more advanced two-equation $\boldsymbol{k-\omega\ SST}$ model **[85]**

Table 2.RANS Turbulence Model Descriptions and Usage [85]

Model	Description	Behavior and Usage
Spalart-Allmaras	▪ A single transport equation model solving directly for a modified turbulent viscosity. ▪ Designed specifically for aerospace applications involving wall-bounded flows on a fine near-wall mesh. ▪ Fluent's implementation allows the use of coarser meshes, and Option to include the strain rate in the production term improves predictions of vortical flows.	▪ Economical for large meshes. ▪ Performs poorly for 3D flows, free shear flows, and flows with strong separation. ▪ Suitable for mildly complex (**quasi-2D**) external/internal flows and boundary layer flow under pressure gradient **(eg** airfoils, wings, airplane fuselages,…**)**
Standard $k-\varepsilon$	▪ The baseline two-transport-equation model solving for k **and** ε. Coefficients are analytically derived, valid for fully turbulent flows only. ▪ Options to account for viscous heating, buoyancy and compressibility are shared with other $k-\varepsilon$ models.	➢ Strong. Widely used despite the known limitations of the model. ➢ Performs poorly for complex flows ➢ involving severe pressure gradient, separation, and strong streamline curvature. ➢ Suitable for initial iterations, initial screening of alternative designs, and parametric studies.
Realizable $k-\varepsilon$	➢ A variant of the standard $k-\varepsilon$ model. ➢ Equations and coefficients are analytically derived. Significant changes in the ε equation improve the ability to model highly strained flows. ▪ Additional options aid in predicting swirling and low Reynolds number flows.	➢ Suitable for complex shear flows involving rapid strain, moderate swirl, vertices, and locally transitional flows (eg boundary layer separation, massive separation, vortex shedding behind bluff bodies)
Renormalization-group (RNG) $k-\varepsilon$	➢ A variant of the standard $k-\varepsilon$ model. Its "**realizability**" comes from changes that allow certain mathematical constraints to be obeyed which ultimately improves the performance of this model.	➢ Offers largely the same benefits and has similar applications as Realizable. ➢ Possibly harder to converge than Realizable.
Standard $k-\omega$	➢ A two-transport-equation model solving for k and ω, the specific dissipation rate (ε / k) based on Wilcox (1998). ➢ This is the default $k-\omega$ model. ➢ Demonstrates superior performance to $k-\varepsilon$ models for wall-bounded and low Reynolds number flows. ➢ Options account for low Reynolds number effects, free shear, and compressible flows.	➢ Superior performance for the wall bounded boundary layer, free shear, and low Reynolds number flows. ➢ Suitable for complex boundary layer flows under adverse pressure gradient and separation (external aerodynamics and turbomachinery). ➢ Separation can be predicted to be excessive and early.
$k-\omega$ *SST*	➢ A variant of the standard $k-\omega$ model. Combines the original Wilcox model for use near walls and the standard $k-\varepsilon$ model away from walls using the blending function. ➢ Also limits turbulent viscosity to guarantee that $\tau\sim$k.	➢ Offers similar benefits as standard $k-\omega$. ➢ Not overly sensitive to inlet boundary conditions like the standard $k-\omega$ ➢ Provides a more accurate prediction of flow separation than other RANS models.
Reynolds stress model **(RSM)**	➢ Reynolds stresses are solved directly using the transport equation, avoiding the isotropic viscosity assumption of other models. ➢ Use for highly swirling flows. ➢ The quadratic pressure-strain option improves performance for many basic shear flows.	➢ Physically the most sound RANS model. Avoids isotropic eddy viscosity assumption. ➢ More CPU time and memory are required. Tougher to converge due to the close coupling of equations. ➢ Suitable for complex 3D flows with strong streamline curvature, and strong swirl rotation (eg curved duct, rotating flow passages,).

➢ **The transport equations :**

The transport equation defines how a scalar quantity moves through space.

$$\frac{\partial}{\partial t}(\bar{\rho}k) + \frac{\partial}{\partial x_j}(\bar{\rho}\tilde{u}_j k) = \frac{\partial}{\partial x_j}\left[\left(\bar{\mu} + \frac{\overline{\mu_t}}{Pr_k}\right)\frac{\partial k}{\partial x_j}\right] + G_k + G_b - \bar{\rho}\varepsilon - Y_M + S_k \quad \textbf{(II.24)}$$

$$\frac{\partial}{\partial t}(\bar{\rho}\varepsilon) + \frac{\partial}{\partial x_j}(\bar{\rho}\tilde{u}_j\varepsilon) = \frac{\partial}{\partial x_j}\left[\left(\bar{\mu} + \frac{\overline{\mu_t}}{Pr_\varepsilon}\right)\frac{\partial \varepsilon}{\partial x_j}\right] + C_{\varepsilon 1}\frac{\bar{\rho}\varepsilon}{k}(G_k + C_{\varepsilon 3}G_b) - C_{\varepsilon 2}\frac{\bar{\rho}\varepsilon^2}{k} + S_\varepsilon \quad \textbf{(II.25)}$$

Where:

- G_k indicates the generation of kinetic energy as a result of the velocity gradient,
- G_b is the production of **k** as a result of volume force detachment,
- Y_M is the contribution of fluctuating expansion in the compressible turbulence for (ε),
- $C_{\varepsilon 1}, C_{\varepsilon 2}, C_{\varepsilon 3}$ are constants,
- S_k, S_ε Source terms,
- Pr_k, Pr_ε are Prandtl's turbulent number for k and ε.

➢ **Turbulent viscosity modeling:**

The turbulent viscosity is calculated using the following formula:

$$\mu_t = \rho\, C_\mu \frac{k^2}{\varepsilon} \quad \textbf{(II.26)}$$

➢ **Turbulence production modeling:**

The term Gk denotes the generation of turbulent kinetic energy and is similarly modeled in standard $(k-\varepsilon)$ models, RNG models, and realizable models. This term can be defined using the exact transport equation of **k** as given in the following equation:

$$G_k = -\bar{\rho}\overline{u_i'' u_j''}\frac{\partial \tilde{u}_j}{\partial x_i} \quad \textbf{(II.27)}$$

The value of $G_k$using the Boussinesq hypothesis takes the following form:

$$G_k = \overline{\mu_t} S^2 \quad \textbf{(II.28)}$$

Where **S** is the medium tensor module of the stress ratio and S_{ij} is the strain tensor, defined as:

$$S = \sqrt{S_{ij}S_{ij}} \quad \textbf{(II.29)}$$

$$S_{ij} = \frac{1}{2}\left(\frac{\partial U_i}{\partial x_j} + \frac{\partial U_j}{\partial x_i}\right) \quad \textbf{(II.30)}$$

- **Effect of volume force on turbulence:**

The generation of turbulence due to pressure forces is given by:

$$G_b = \beta g_i \frac{\overline{\mu_t}}{Pr_t}\frac{\partial \widetilde{T}}{\partial x_i} \quad \textbf{(II.31)}$$

- Pr_t is the turbulent Prandtl coefficient for energy, which is given on both realizable and standard models by default by: $Pr_t = 0.85$
- g_i is the component of the gravitational vector in the **i** direction.
- Thermal expansion coefficient β is given by: $\beta = -\frac{1}{\bar{\rho}}\left(\frac{\partial \bar{\rho}}{\partial T}\right)_p$
- In ideal gas case we have:

$$G_b = -g_i \frac{\overline{\mu_t}}{\bar{\rho} Pr_t}\frac{\partial \bar{\rho}}{\partial x_i} \quad \textbf{(II.32)}$$

- **Compressibility Effects:**

Compressibility influences turbulence through dissipation of expansion for flows with a high Mach number, which is generally ignored in the modeling of incompressible flows. Neglecting expansion dissipation explains the reduction in dissipation ratio observed for compressible mixtures and other free shear layers as the number of Mach increases **[86]**.

To describe these effects in the $k-\varepsilon$ models in Fluent, the term Y_M dilation dissipation is included in the equation of k. According to **S. Sarkar et al.**, this term consists of the following form **[87]**:

$$Y_M = 2\bar{\rho}\varepsilon M_t^2 \quad \textbf{(II.33)}$$

$$M_t = \sqrt{\frac{k}{a^2}}\ , \qquad a = \sqrt{\gamma r T} \quad \textbf{(II.34)}$$

Where a represents the speed of sound.

II.4 Wall Treatments

FLUENT provides three types of wall treatment, although all three may not be available at all times depending on the turbulence model, and wall treatment is a set of near-wall modeling assumptions for each turbulence model. The types are described in the following:

The **"high-y+"** wall treatment implies a wall function approach in which the near-wall cell is assumed to be within the boundary layer's logarithmic region.

The **"low-y+"** wall treatment is only appropriate for low Reynolds number turbulence models in which the viscous sub-layer is assumed to be suitably resolved.

The **"all-y+ "** wall treatment is a hybrid that aims to replicate the high-wall treatment for coarse meshes and the low-y+ wall treatment for fine meshes. It is also developed with the required feature of generating appropriate responses for meshes of intermediate resolution (– in other words, when the wall-cell centroid falls inside the boundary layer's buffer zone).

The wall functions are a set of semi-empirical functions that are used to match the physics of the flow near the wall. The existence of the wall influences turbulent flow in a variety of ways, including the non-slip requirement that must be achieved at the wall. The near-wall zone is made up of four parts: the laminar sub-layer, the blending region, the log law region, and the outer region. Each region has a different influence on turbulence, and the y^+ position of the initial cell in the boundary layer requires special attention. Depending on the size of this cell, a new set of equations will be employed, although this one must not be comprised between $y^+ = 5$ and $y^+ = 30$ because no turbulent model is available in this area.

Instead of not resolving the entire boundary layer for a y^+ comprised in the viscous sub-layer and buffer layer, wall functions are used to bridge the viscosity-affected region between the wall and the fully-turbulent region.

II.4.1. Standard Wall Functions

Standard wall functions provide good accuracy for the vast majority of high-Reynolds-number, wall-bounded flows, but they fail when the flow circumstances differ considerably from the ideal conditions used to create the functions.

The following are examples of when these restrictions may be reached:

- Widespread low-Reynolds-number or near-wall effects (e.g., flow through a small gap or highly viscous, low-velocity fluid flow),
- Strong transpiration (blowing/suction) through the wall,
- Extreme pressure gradients induce boundary layer separations,
- Body forces that are strong (e.g., flow near rotating disks, buoyancy-driven flows),
- High three-dimensionality in the near-wall region (e.g., Ekman spiral flow, severely skewed 3D boundary layers).

The standard wall functions are derived from the momentum equation, which leads to the law of the wall for the temperature and depends on the y* to considerably minimize the cost of computation (memory size and simulation time) and the laws of walls are utilized to replace the condition of adherence to a wall.

$$\mathbf{T}^* = \frac{(\mathbf{T_\omega} - \mathbf{T_p})\,\boldsymbol{\rho}\mathbf{c_p}\mathbf{C_\mu^{\frac{1}{4}}}\mathbf{k_p^{\frac{1}{2}}}}{\dot{\mathbf{q}}} \qquad \textbf{(II.35)}$$

$$\mathbf{T}^* = \begin{cases} \mathbf{Pr}\, y^* + \frac{1}{2}\rho Pr \frac{C_\mu^{\frac{1}{4}} k_p^{\frac{1}{2}}}{\dot{q}} U_P^2 & (y^* < y_T^*) \\ Pr_t \left[\frac{1}{k}\ln(Ey^*) + P\right] + \frac{1}{2}\rho \frac{C_\mu^{\frac{1}{4}} k_p^{\frac{1}{2}}}{\dot{q}} \left\{Pr_t U_P^2 + (Pr + Pr_t) U_c^2\right\} & (y^* > y_T^*) \end{cases} \qquad \textbf{(II.36)}$$

$(y^* < y_T^*)$**:** Linear law for the thermal conduction sublayer where conduction is important.

$(y^* > y_T^*)$**:** Logarithmic law for the turbulent region where effects of turbulence dominate conduction.

The pressure **P** is computed using ***Jayatilleke***'s formula, and the y_T^* is determined as the y^* reach the linear and logarithmic laws intersect. The linear or logarithmic profile is used to calculate the wall temperature $\mathbf{T_\omega}$ or heat flux **q**, depending on the y^* value at the near-wall cell.

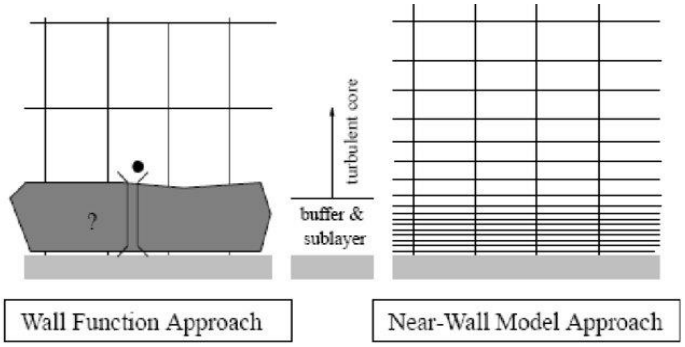

Figure II-1 Near-wall treatment in FLUENT (FLUENT, 2005a) [88]

Table 3.Near-wall treatment in FLUENT (FLUENT, 2005a) [88]

➢ **Wall Function Approach:**	➢ **Near-Wall Model Approach:**
▪ First grid point in log-law region $30 \sim 50 \leq y^+ \leq 500$ ▪ The viscosity-affected region is not resolved, instead is bridged by the wall functions. ▪ High-Re turbulence models can be used because the viscosity-affected region is skipped.	▪ First grid point at $y^+ \sim 1$ *or less*. ▪ Requires a sufficient number of grid points (>10) within buffer and sublayers. ▪ Low-Re models are needed ▪ The near-wall region is resolved all the way down to the wall. ▪ The turbulence models ought to be valid throughout the near-wall region.

- Transport equations for turbulent quantities are only solved in the fully formed turbulence zone and outside of the boundary layer using the law of the wall model. This is accomplished by taking the distance between the center of the first mesh and the wall as $30 < y^+ < 300$.
- A local equilibrium hypothesis is used to compute the production of turbulent kinetic energy, G_k, and its dissipation rate ε, in the cell close to the wall. We have, according to Launder and Spalding **[89]**, the production term is defined as follows:

$$G_k \approx \tau_\omega \frac{\partial U}{\partial y} = \tau_\omega \frac{\tau_\omega}{\rho \kappa C_\mu^{1/4} k_p^{1/2} y_P} \quad \textbf{(II.37)}$$

ε is computed from**:**

$$\varepsilon_P = \frac{C_\mu^{3/4} k_p^{3/2}}{\kappa y_P} \quad \textbf{(II.38)}$$

We are not concerned with the specifics of the boundary layer, but with the overall effect of a wall on the flow. The modeling of near-wall turbulent flows is based on the modeling of simple sheared wall turbulent flows.

The following parameters are developed in order to represent the various rules of speed distribution in the various zones:

$$y^+ = \frac{\bar{\rho} y u_\tau}{\mu} \quad \textbf{(II.39)}$$

$$u^+ = \frac{\tilde{u}}{u_\tau} \quad \textbf{(II.40)}$$

- **Where:**

$$u_\tau = \sqrt{\frac{\tau_\omega}{\rho}}$$

τ_ω is the shear stress at the wall.

➢ The turbulent boundary layer near a smooth wall is decomposed into three separate layers by a multi-scale temporal analysis:

1. A viscous sublayer is the first layer in which the fluid viscosity dominates the turbulent viscosity. The velocity profile in this zone is linear and is expressed as follows:

$$u^+ = y^+ \qquad \textbf{(II.41)}$$

2. The viscous sublayer extends to a thickness of $y^+ = 5$

A buffer zone is an intermediate layer where fluid viscosity and turbulent viscosity are equal.

3. An outer layer with high turbulent viscosity and a logarithmic velocity profile, which is expressed as follows:

$$u^+ = \frac{1}{\kappa}\log(EY^+) \qquad \textbf{(II.42)}$$

Where E, κ (Von Karman constants), which have fixed values equal to: $E = 0.9$ and $\kappa = 0.4$.

- This outer layer is supposed to start from $y^+ > 50$
- The turbulence model is the $k-\varepsilon$ model, in which the k equation is calculated over the entire domain, including the surrounding wall region, with the following boundary condition:

$$\frac{\partial k}{\partial n} = 0 \qquad \textbf{(II.43)}$$

where **n** is the local coordinate normal to the wall.

- With the standard k-ε model, the Reynolds wall stresses are calculated assuming the existence of a velocity profile between the wall and the first cell close to it. This profile is modeled by laws similar to those described above. They are written as follows:

$$u^* = \begin{cases} y^* & if \quad y^* \le 11.225 \\ \frac{1}{\kappa}\log(Ey^*) & if \quad y^* > 11.225 \end{cases} \qquad \textbf{(II.44)}$$

The expressions for u^* and y^* are:

$$y^* = \frac{\bar{\rho} C_\mu^{1/4} k_p^{1/2} y_p}{\mu}, \qquad u^* = \frac{\tilde{u}}{u_\tau} = \frac{C_\mu^{1/4} k_p^{1/2} \tilde{u}_p}{\tau_w/\bar{\rho}} \qquad \textbf{(II.45)}$$

- **With:**

$\tilde{u}_p$ being the average velocity of the fluid at point **P** located at a distance y_p from the wall,

k_p is the turbulent kinetic energy at point **P**.

II.4.2. Enhanced wall functions

In FLUENT, the enhanced function is utilized to enable near-wall modeling with the accuracy of the standard two-layer approach for fine meshes at the same time without compromising the results for wall function meshes. The enhanced wall functions are coupled with the two-layer model to accomplish that.

The two-layer model is a near-wall model that resolves the entire boundary layer until it reaches the viscous sub-layer. The entire domain is divided into two regions: viscosity-affected and totally turbulent, with the separation determined by a wall distance given by a Reynolds number dependent on **y**.

$$Re_y \equiv \frac{\rho y \sqrt{k}}{\mu} \qquad \textbf{(II.46)}$$

Although the enhanced wall treatment is intended to extend the validity of near-wall modeling beyond the viscous sublayer, it is still recommended that you build a mesh large enough to resolve the viscosity-affected near-wall region. In this situation, the two-layer component of the enhanced wall treatment will be dominant, and the following mesh requirements are suggested (notice that the mesh requirements are expressed in terms of y^+ rather than y^*) **[90].**

- When using the enhanced wall treatment to resolve the laminar sublayer, y+ at the wall-adjacent cell should be on the order of y^+**= 1**. A greater y+, however, is acceptable as long as it is well inside the viscous sublayer **(y^+<4 to 5) [90].**

- At least ten (10) cells must be available within the viscosity-affected near-wall region **(Re_y<200),** to resolve the mean velocity and turbulent quantities in that region **[90]**

II.5 Conclusion

In this chapter, we provided the equations that govern the flows around an aerodynamic profile, along with the continuity and momentum equations, as well as their non-dimensional and averaged equations. As it introduces an extra element (Reynolds stress), a suitable closure model combining the flows near to the walls and those far from the wall was necessary.

CHAPTER

Numerical Approach

III

CHAPTER CONTENT

III.1 Numerical Approach…..……
III.2 CFD with ANSYS Fluent …….
III.3 Conclusion……..

OUTLINE

In this chapter, The third chapter goes into great depth on the presentation of the computational code, containing a brief explanation of the **CFD** which stands for computational fluid dynamics, which is used for numerical resolution, followed by the inputs and parameters of our simulation.

III.1 Introduction

What is the exact meaning of **CFD**? **CFD** stands for computational fluid dynamics, which is a powerful tool that simulates fluid motion using computational models. It can be used to analyze aerodynamics, fluid dynamics, combustion systems, and a variety of other case studies.

Fluid dynamics is a branch of fluid mechanics that studies the motion of liquids and gases. In particular, it focuses on the properties of fluids at rest and under the influence of forces that act on a fluid causing it to move and fluid motion can be described in different ways. It is divided into various sub-disciplines in physics and engineering, one of which is aerodynamics, which is the study of moving air and its influence on solid bodies placed in the flow field as an obstacle, and most fluid dynamics equations, including all governing equations, turbulence, boundary layer theory, and the ideal gas assumption, also apply to aerodynamics. However, in terms of physical behavior, they are very similar and can be modeled using CFD, more importantly, this can be integrated into the mechanical design process for almost anything that moves in a fluid or gas, such as airplanes, vehicles, motorcycles, and so on.

To begin, performing an effective simulation requires a fundamental understanding of fluid dynamics and partial differential equations. This understanding is based mostly on the fact that CFD replicates the Navier-Stokes equation, which governs fluid dynamics. A numerical solver or a commercial CFD solver is all that is necessary.

Numerical solvers can be any form of calculator that allows you to solve the governing equations of fluid dynamics, such as Matlab or Python. In this manner, we may create our own solver and numerical factors. What is also very common are CFD solvers that contain all of these numerical solvers fully integrated and we only need to know which solver we want to use and what parameters to experiment with. The most common of these is, Ansys Fluent, which I use in my validations.

III.2 CFD with ANSYS Fluent

The general process is to first create a geometry in CAD software or within Ansys (Design Modeler, SpaceClaim), then meshing, which divides the entire system into smaller parts to simulate, then set the solver to specify how exactly we want the computer to solve the governing equations, solve those equations numerically, and lastly post-processing.

As a result, unless the geometry is very simple, meshing and setting up the solver is always the most complex and time-consuming element of putting up a successful CFD simulation.

Although the actual iterative procedure is generally something we only watch the computer execute, post-processing might take some time.

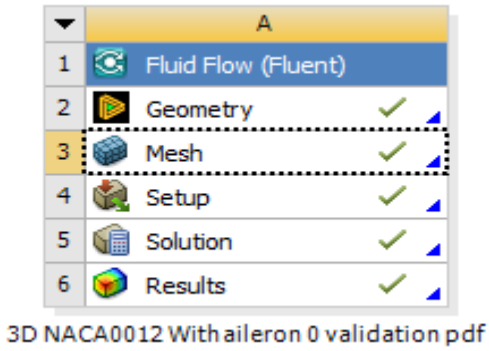

Figure III-1 ANSYS Fluent 21 R2 workbench steps

III.2.1. Geometry

The geometry is straightforward, depending on the case study, it can be two-dimensional or three-dimensional, and we investigated both in this research, it is important to note that the fluid is being simulated and not the object. Starting with a **2D simulation**, I subtract the location of the airfoil and simulate the fluid around and outside of it, with the airfoil only serving as a limitation. The following are the aerodynamic profiles investigated in this paper:

1. Symmetric airfoil NACA0012,
2. Supercritical airfoil OAT15A,
3. Supercritical airfoil RAE2822,
4. Symmetric airfoil NACA0012 with aileron at different deflection angles.
5. Supercritical airfoil OAT15A with aileron and spoiler at different deflection angles.

III.2.2. Meshing:

Meshing is the process of dividing a fluid region into smaller parts, or cells, in order to solve the governing equations at each point in space. It assists in discretizing and approximating the values of the turbulent equations using iterative approaches, allowing us to do multiple CFD simulations efficiently. In theory, it is feasible to simulate non-iterative methods or directly solve the Navier-Stokes equations on turbulent scales for CFD, which is known as a direct numerical simulation that enhances accuracy by adding more cells. In general, more cells indicate greater accuracy, but also more computational effort for meshing, thus there is always a delicate balance between what is accurate and what can be achieved in a reasonable amount of time. Therefore, there are three methods for dividing these cells: the finite element method, the finite volume method, and the finite difference method. There are several methods for solving each cell inside a mesh, each with significant advantages and disadvantages in terms of stability and solution precision.

Meshing and obtaining technical details are important because we want everything to be exact while being computationally economical. Cells should be refined only in locations with larger pressure gradients where an interesting phenomenon, such as separation, would occur. Flaps, sharp edges, and bumps can all create various forms of separations.

- Ansys can do both structured and unstructured meshing on an airfoil. When we run a higher angle of attack, the structured mesh on an airfoil should have a more defined region in the wake direction.

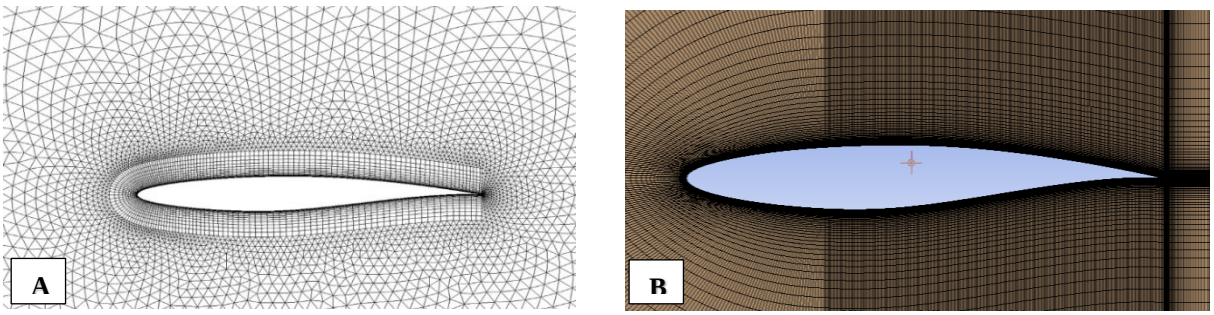

Figure III-2 RAE2822 airfoil A) Unstructured mesh B) Structured mesh

III.2.2.1. Y Plus (Y^+)

Y plus is the first layer height, for most models, including the Spalart-Alamars, k-omega, LES, and DES models, it should be less than one. There are techniques to increase y plus values in order to reduce computational demand by using wall functions, which are usually seen in the k-epsilon model but also in the k-omega SST model. In this case, y plus less than five is preferable based on the "Law of the Wall."

The "Law of the Wall" governs how boundary layers behave and the approximations that are appropriate for different areas of the boundary layers, as well as why "y plus" less than one is required for accurate boundary layer calculation. This is detailed in-depth in the previous chapter.

III.2.2.2. Mesh quality

The precision and stability of the numerical computation are greatly influenced by the mesh quality. Characteristics associated with mesh quality include node distribution, smoothness, and skewness.

Verifying the quality of the grid is essential regardless of the type of mesh utilized in your domain. Different quality parameters are examined depending on the cell types in the mesh (tetrahedral, hexahedral, polyhedral, etc.). There are several options for determining mesh quality:

1. **Mesh independence** is an important technique in which we begin with an initial mesh (structured or unstructured) and increase the cell count by decreasing the size. The refinement may then be increased in the first layer's height or in the region behind it. And then observe how the values change, if they don't change after raising the number of cells any further, we've reached a point where adding more cells doesn't result in additional accuracy, showing that we've achieved mesh independence.

2. Other basic guidelines for creating a decent mesh include skewness, aspect ratio, orthogonality, and growth ratio. They can be very different for various types of applications.
    - **2.1. Skewness**, for example, is an essential aspect of mesh quality since it relates to cell form. A structured quadrilateral mesh should have zero skewness, but nothing can be this perfect, therefore we should aim to maintain it as low as possible. However, the skewness for unstructured meshes is on a scale of zero to one, and the skewness for triangular and tetrahedral meshes should be maintained below **0.9**.

2.2. **Aspect ratio** is a measure of a cell's stretching; it is the ratio of the cell's length and height and should be kept below **35** in areas with severe stress or flux gradients. However, even around **40** produces acceptable outcomes. In terms of convergence, higher aspect ratios can cause flux imbalance and divergence. It may also be defined as the greatest distance between cell centroid and centroids divided by the minimum distance between cell nodes.

2.3. **The growth ratio** is the change in volume from one cell to the next, and the smaller the change, the better. According to research, you should not go over **1.2**.

Furthermore, we can test running the computation first to determine if the mesh is appropriate for the calculation. For example, since meshing might take hours or days for larger simulations, we can compute it for 100 steps and then evaluate the convergence.

However, a decent mesh is also determined for the models that we are using. These measurements just provide geometric information about the mesh and do not tell if the mesh is good or bad for a certain set of EDPs such as K-omega SST, k-epsilon, or LES models.

Each physics has its own set of criteria when creating a mesh. Some challenges need either a maximum or a minimum element size, or both, in order to completely represent the physics.

"Is the mesh suitable for my problem?" we might ask. A defective mesh or the incorrect usage of a mesh that does not effectively describe the physics can cause **residue oscillations**, **slow convergence**, and **divergence**. However, while a decent metric will not tell us if we have a good or poor mesh, it will ensure that convergence difficulties are avoided or decreased. The physical nature of the problem must also be considered in this approach.

With the assumption that everything is correct in terms of metrics and physics. In addition, if we have three grids with solutions that are quite near, we may measure the difference and evaluate if we have mesh independence based on the criterion of change of solution, as well as how these three meshes may operate within our requirements. The computational effort may be an issue, and a hard mesh may be employed to complete the tasks, but consider the fact that we are not certain if our problem is meshed independence.

III.2.3. Setting up Solver:

After meshing, the next step is to set up the solver, which should be straightforward because we choose whether we want two or three dimensions.

I set up parallel processing to divide the mesh and have each processor solve a section of the grid, which may speed up the process of putting it all together in the end, but it may also create errors. Because various applications have significantly varied setups, it is likely safer if we investigate our case carefully so that we can be certain about the setups.

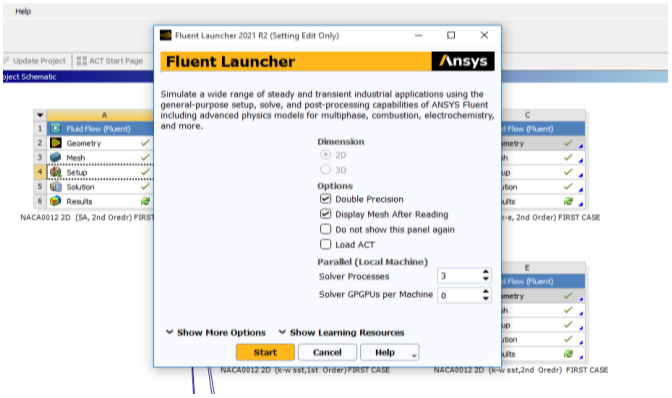

Figure III-3 ANSYS Fluent Launcher 2021 R2

Here is how Ansys Fluent is set, as we can see, there are various solver settings that must be altered based on our condition. In general, we utilize pressure-based flow for incompressible flow because density does not change, and density-based for compressible flow since the density of fluid varies, which is our study case. Moreover, we have the option of using either **Steady-state** or **Transient-state** solvers.

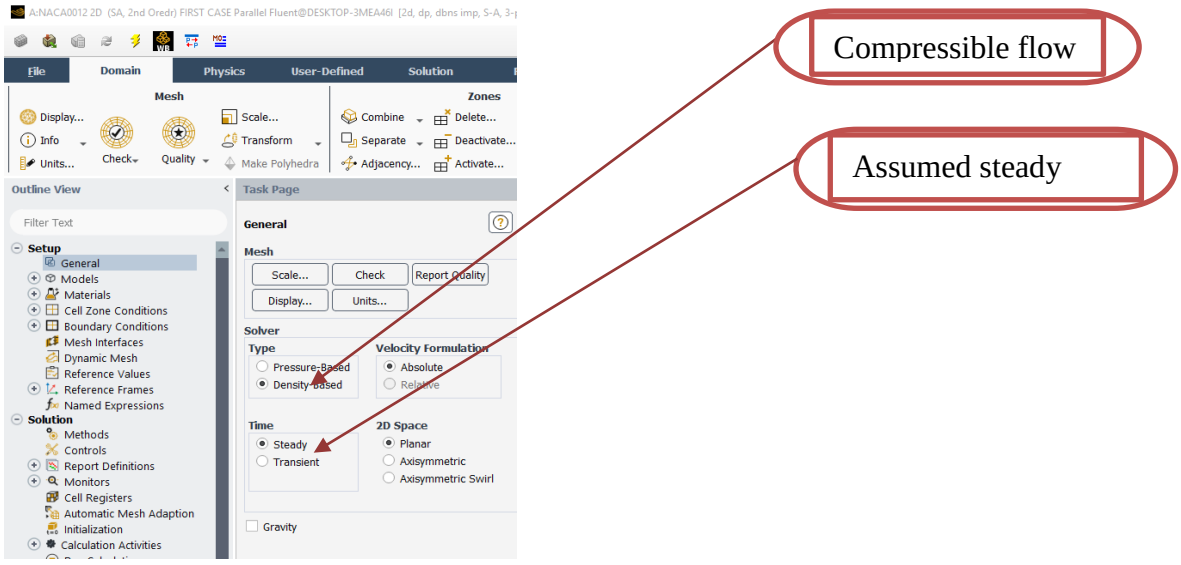

Figure III-4 Setting Up The Solver

A transient state is used to see how values change over time, whether it is vortex shedding or the time changing evolution of a fluid system, while a **steady state** is probably the best for general aerodynamic forces analysis (Drag, Lift, etc.).

III.2.3.1. Models

A. Energy equation

The energy equation is applied when heat transfer or combustion problems are included.

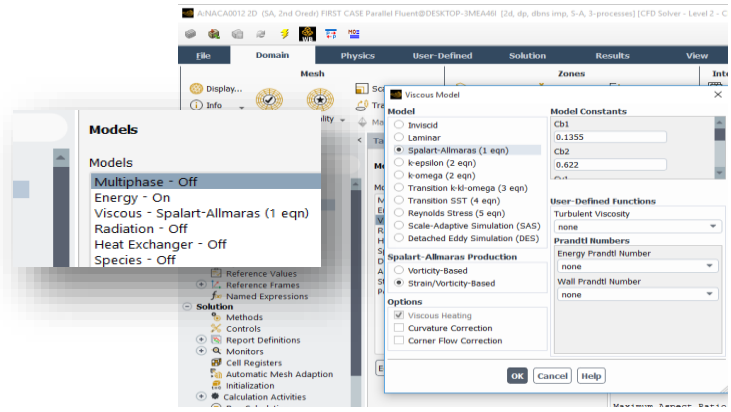

Figure III-5 Setting Up The Physics

B. Turbulent Model equations

- One Equation Turbulent: Spallart-Allmarus,
- Two Equation Turbulent: K-Omega, K-Epsilon.

They are most commonly used for basic solutions and space difficulties. These equations have many forms, such as the K-omega SST and the K-Epsilon, as well as their different wall functions, including standard wall functions, enhanced wall functions, far and wide, and in between.

III.2.3.2. Define Materials

Once we choose the model, we **Define Fluid** (Air, Water, etc). Temperature, viscosity, and other properties vary as we deal with heated air or hot water.

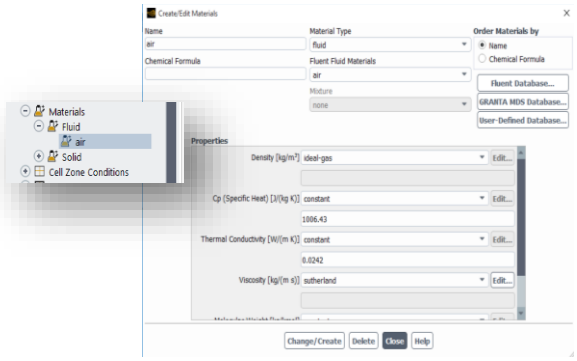

Figure III-6 Defining fluid and its properties

Also, the solid which is aluminum

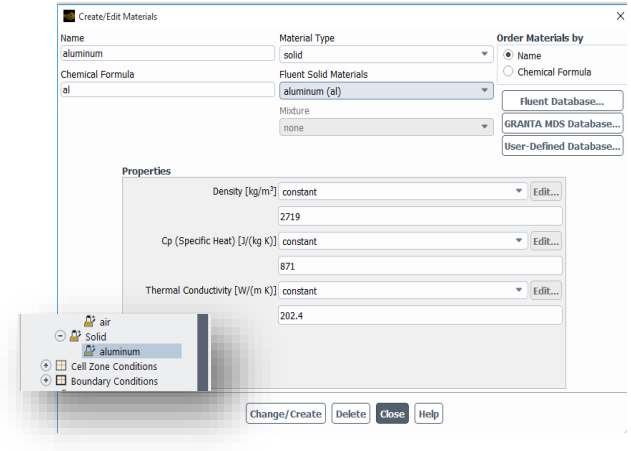

Figure III-7 Defining solid and its properties

III.2.3.3. Boundary conditions

From there, we define Boundary Conditions, in which there are several different value conditions that have a huge role in a fluid system.

A. Pressure Far Field

We used **Pressure Far Field** as a boundary condition. In addition, the static pressure and upstream air temperature for the simulations were calculated using:

$$P_\infty = P_0 \left[1 + \frac{(\gamma-1)}{2} M_\infty^2\right]^{(\gamma-1)/\gamma} \quad \textbf{(III.1)}$$

$$T_\infty = T_0 \left[1 + \frac{(\gamma-1)}{2} M_\infty^2\right]^{-1} \quad \textbf{(III.2)}$$

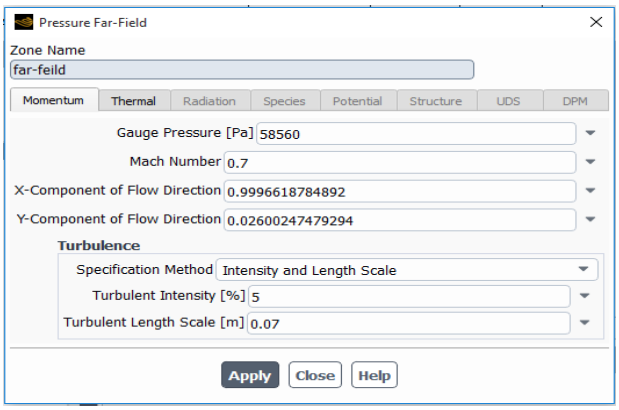

Figure III-8 « Pressure Far-Field » boundary condition

B. wall

No-slip condition for **Walls**, such as an airfoil:

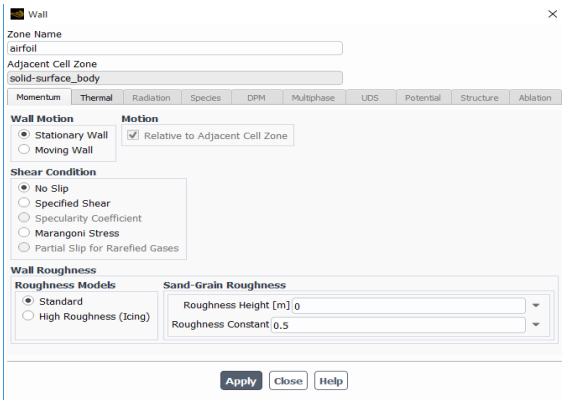

Figure III-9 « Wall » boundary condition.

Dynamic Mesh, we use it to allow the mesh or geometry to actually change during a transient simulation, which is **not** our case.

III.2.3.4. Reference values

We must also define our **Reference values,** which determine the Reference region depending on whether we are simulating in 2D or 3D. For example, the chord length is the reference length of an airfoil. It also defines inlet velocity and metrics for lift, drag, friction coefficients, and other **Report definition** parameters.

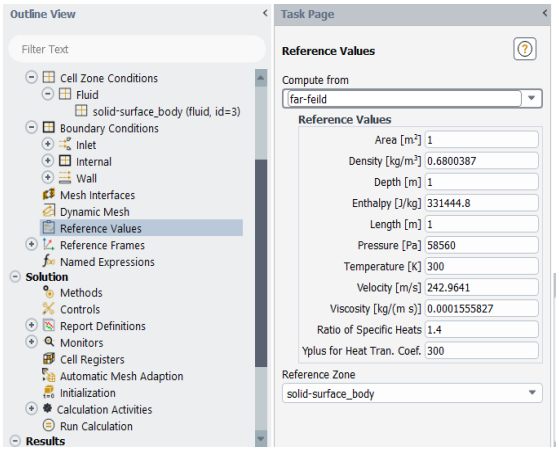

Figure III-10 reference values

III.2.4. Methods and Control

Underneath the **"Methods"** menu, you may set the parameters for the discretization schemes for pressure, momentum and modified turbulent viscosity.

There are different orders for the viscosity and turbulence terms. Higher-order, in general, uses a larger stencil and allows for more precision, but it demands more computational effort.

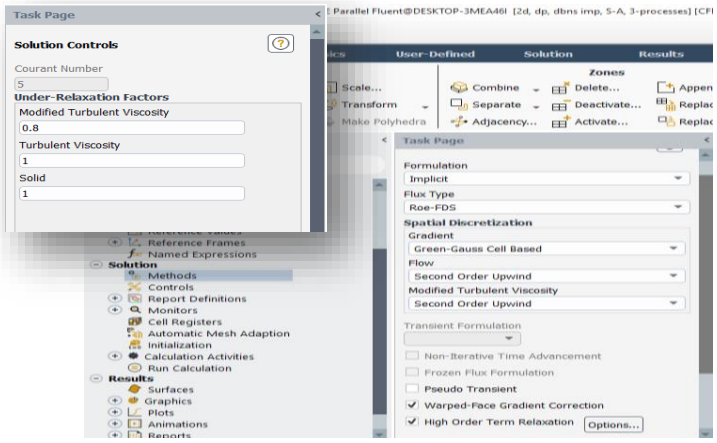

Figure III-11 Simulation Methods and Control

III.2.4.1. Report definitions

Next, **Report definitions** enable calculations for drag, lift, shear stress, and so on.

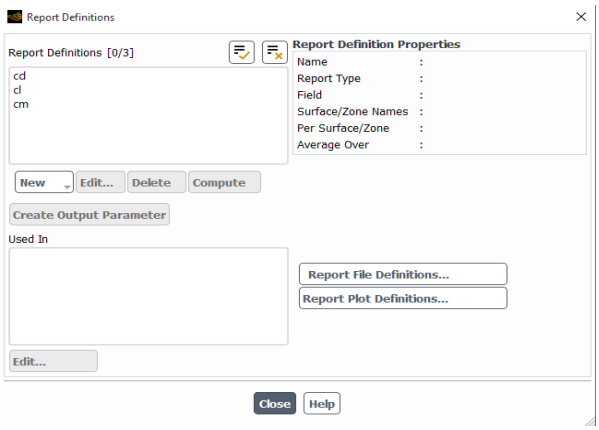

Figure III-12 Report Definitions.

III.2.4.2. Monitors

Monitors indicate what is displayed during the simulation, such as how the continuity, lift, drag, and other values change with each iteration, so if we see a physical value, such as pressure or lift, not changing after any iterations, it means it has finally converged, and no changes in monitored values is generally what convergence is based on.

III.2.4.3. Convergence and monitors

Convergence and monitors, on the other hand, are highly dependent on mesh quality and a variety of other factors.

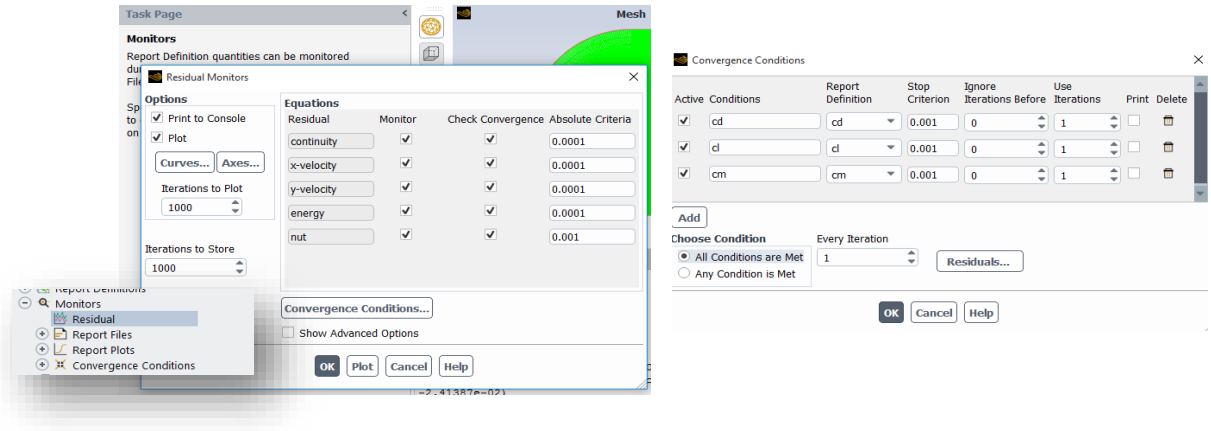

Figure III-13 Simulation Monitors and Convergence Conditions

III.2.5. Calculation

III.2.5.1. initialization

In an iterative method, **initialization** refers to the starting condition that must be applied to all cells, in addition to the boundary conditions that must be satisfied before it can begin solving. In fluent, we have the option of using a **hybrid initialization.**

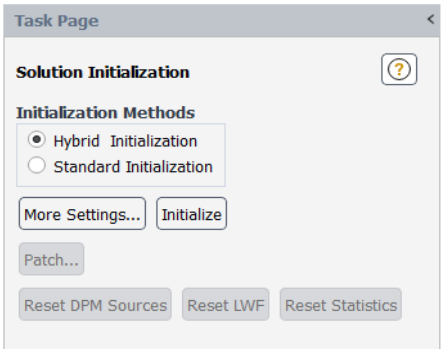

Figure III-14 Solution Initialization

We are brought to the **Run Calculation** button after entering the number of iterations and choosing the flow type, that is transonic flow in our case.

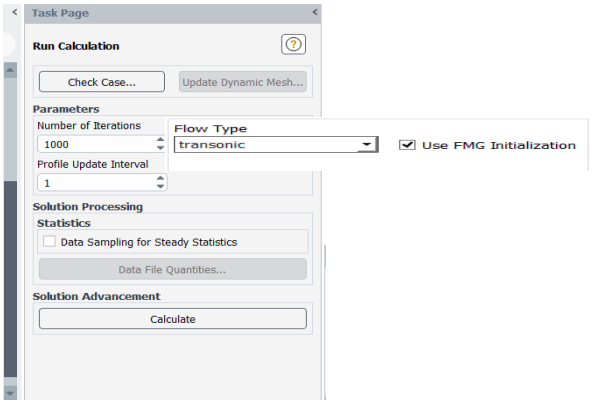

Figure III-15 Run Calculation

After that, the computer proceeds to solve until **Convergence** is reached, which occurs when no changes are observed after each iteration.

Divergence requires troubleshooting and can be caused by many different reasons, including:
Poor mesh quality,
Numerical issues,
Fluid model instability and many more, depending on the situation.

- **Types of errors we face:**

- **Numerical errors**: Whether local or global, solving equations on a machine also introduces numerical errors, which occur when iterative methods are imperfect at approximating values of the governing equations, and a very common problem we get, is the **floating-point** error which is hard to be fixed due to divergence, some other errors are due to settings like coupled/simple flow, parallel processing, relaxation factors, etc.

- **Modeling errors:** Due to the general nature of the governing equations and turbulent models, they provide a good approximation of reality but do not entirely represent reality and analytical solutions, and therefore do not perfectly describe the turbulent flow.

- **Meshing errors:** discretizing a fluid system into smaller cells, the mesh quality might cause errors.

Table 4.Solver parameters used in this study

Parameters	Setup
Type Of Simulation	2D et 3D, Steady
Solver	Double precision, Density -based
Formulation	Implicit
Turbulence Models	$k-\varepsilon$, $k-\omega$, SA
Flow type scheme (differentiation scheme)	Roe-FDS (flux difference splitting)
Flux	Upwind 2^{nd} order
Turbulent kinetic energy	Upwind 2^{nd} order
Turbulente Dissipation Ratio (for k-ε)	Upwind 2^{nd} order
Boundary Conditions	
Far-field	Pressure far-Field
Airfoil	wall

III.3 Conclusion

Computational Fluid Dynamics (**CFD**) is a very powerful tool for predicting fluid flow, heat transfer rates, pressure drops, chemical reactions, fluid dynamic forces such as lift, drag, pitching moments, and related phenomena by solving the mathematical equations that govern these processes and simulating under real conditions fluid flow around or through any object in detail. It can be used in different industries for different analytical capabilities. Such as aerospace, automotive, chemical, power generation, manufacturing, chemical engineering, product design and optimization, oil and gas industry, turbomachinery, etc.

The accuracy of modern **CFD** methods significantly increases the design knowledge available to engineers throughout the design process, and further integration into the mechanical design process for aerodynamic surfaces means fewer physical prototypes are built during product development, reducing costs and prototype testing.

CASE		GEOMETRY	AIRFOIL	MESH	MESH CLOSEUP 200%
2D	RAE2822 Without Control Surface	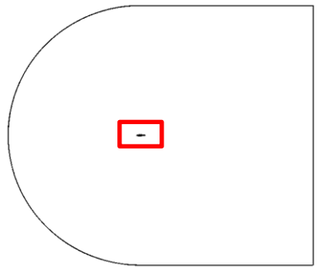		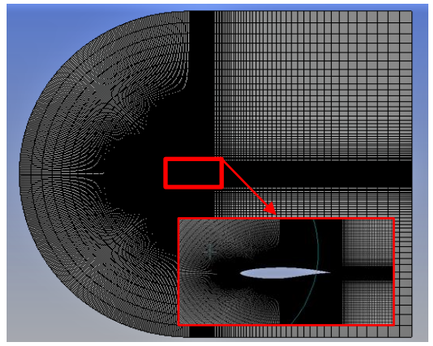	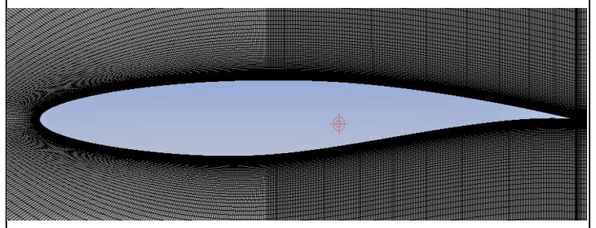
	NACA0012 Without Control Surface	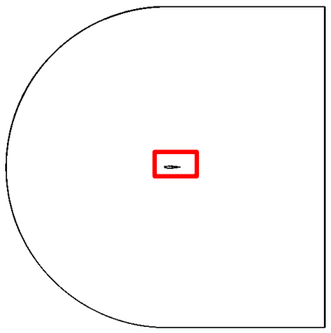		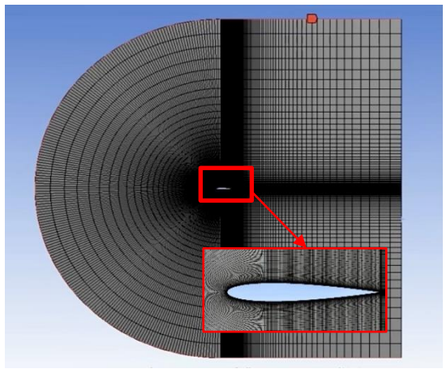	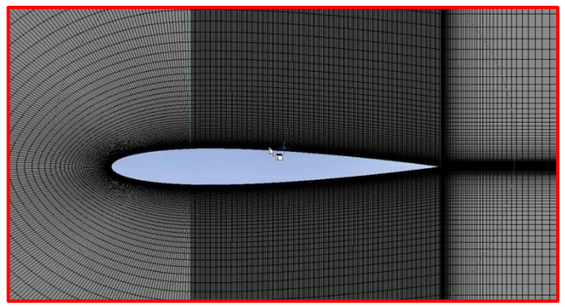
	NACA0012 With Aileron	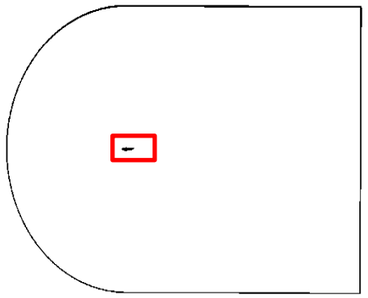	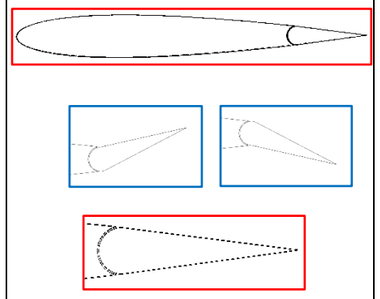	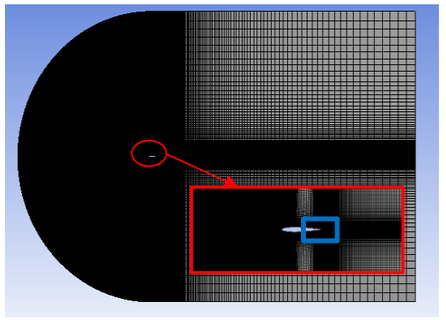	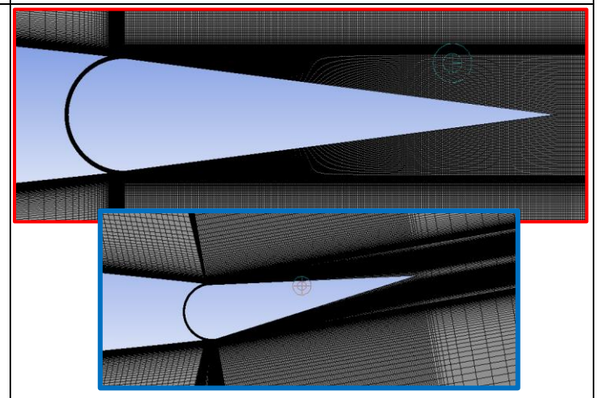

	OAT15A Without CS	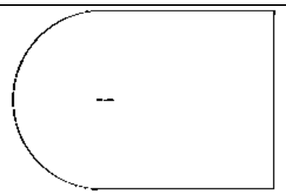		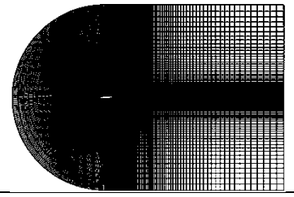	
	OAT15A With Spoiler	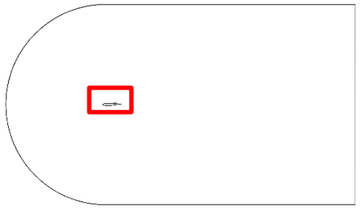	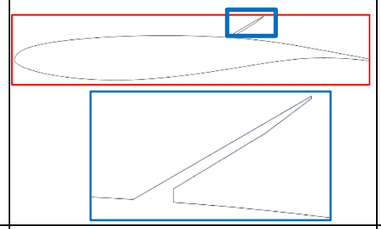	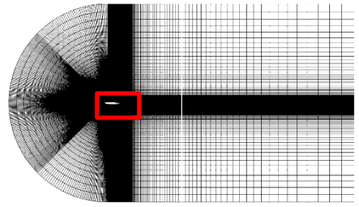	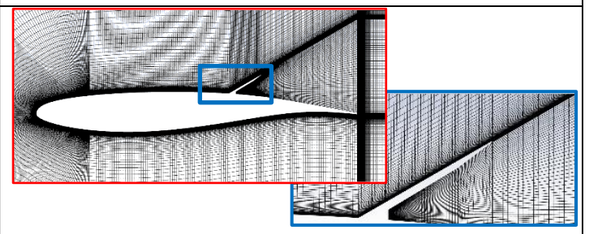
	OAT15A With Aileron		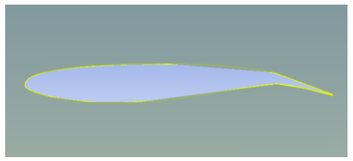	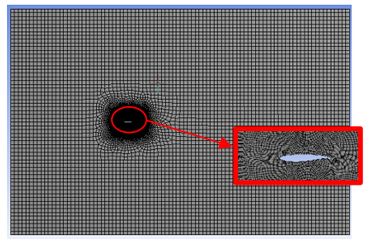	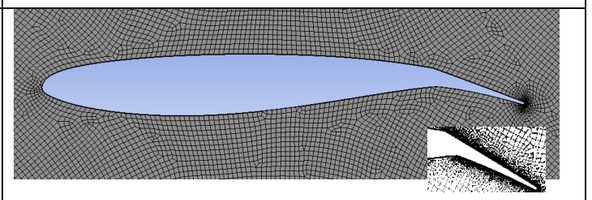
		ONERA M6 Wing	Wing Of NACA0012 Airfoil with Aileron	Wing Of OAT15A Airfoil with Aileron	
3D Wing		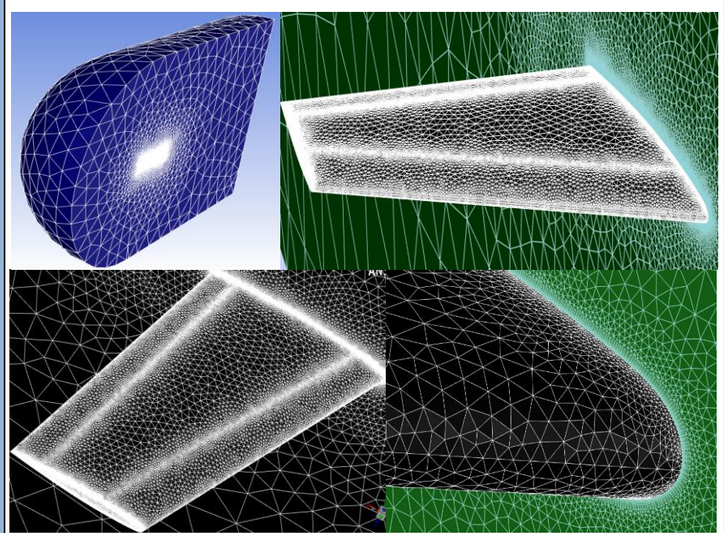	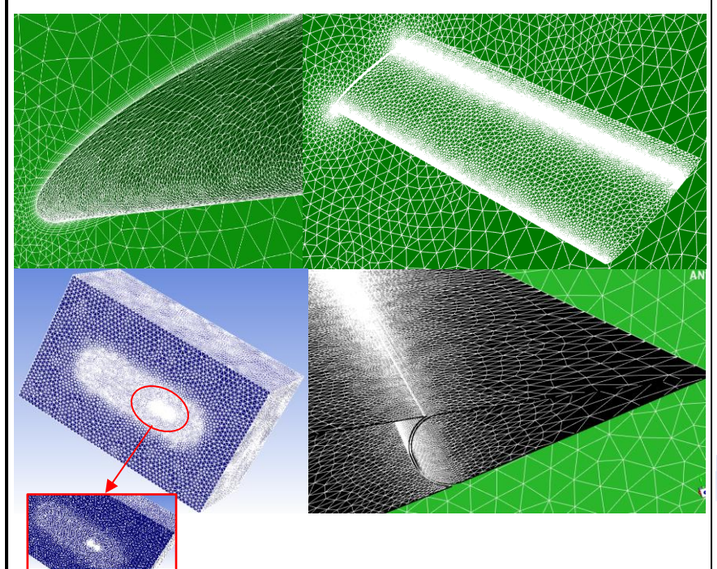	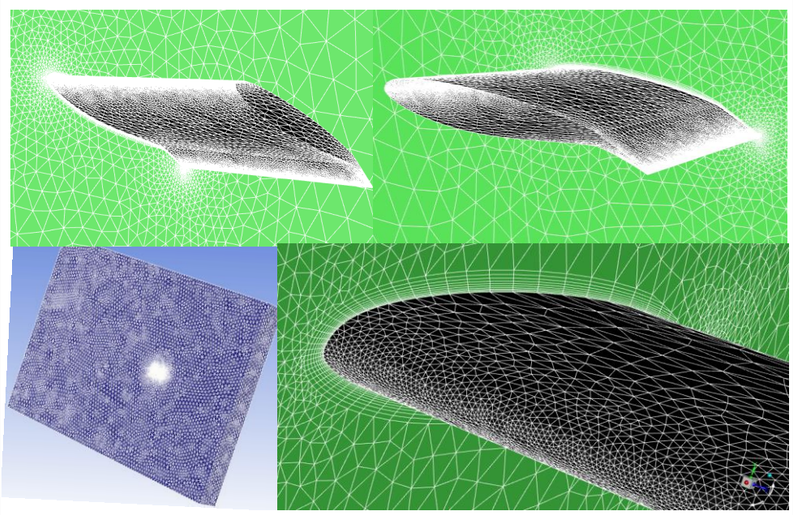	

CHAPTER

RESULTS & DISCUSSION

IV

CHAPTER CONTENT

IV.1 Computer system characteristics and presentation of Ansys workbench…..
IV.2 Convergence criterion for the solutions……..…….
IV.3 Numerical simulation on airfoils without control surface……..
IV.4 Validation of 3D simulation case……...
IV.5 Numerical simulation on OAT15A Airfoil with Spoiler at 30°……..…
IV.6 Comparative Numerical Studies……...
IV.7 AOA Effect On OAT15A airfoil with Aileron at different deflection angles…..
IV.8 Flow description over OAT15A airfoil attached to Spoiler at $\delta_{sp} = 30°$…….
IV.9 Aspect Ratio Impact on Three different Wings…….……..
IV.10 Conclusion……..……..

OUTLINE

This chapter presents studies in the transonic regime, first addressing the influence of fluid domain, mesh, and numerical parameters, as well as turbulence modeling, to determine configuration requirements and mesh generation strategy for airfoils with and without control surfaces such as spoilers and ailerons, as well as wing configurations with and without aileron. As a result, a comparative evaluation with an experimental database available, a number of sample solutions, and the effects are discussed with regard to the varied spoiler and aileron deflections and incidences angles compared with measurements.

For 2D simulation, the choice fell on experimental studies for the supercritical airfoils OAT15A and RAE2822, as well as conventional airfoil NACA0012, and for 3D simulation, we have ONERA M6 Wing, Wing of OA15A Airfoil with aileron, and Wing of NACA0012 airfoil with and without aileron at different deflection angles..

IV.1 Computer system characteristics and presentation of Ansys workbench

The results of simulations depend on the capacity of the machine. In this Master project, the calculations are performed by *Spirit of Gamer Deathmatch 5* which has the following properties summarized in the table below:

Table 5.Characteristics of the used computer system

Processor	Intel ® i9-10900kf 20 cores (3.75 GHz)	
RAM	32 GO	
Graphic processor	Nvidia Quadro	
Hard Disc	**HDD**	2 TO
	SSD	500 GO

IV.1.1. Ansys 2021 R2

This software tool provides an unlimited modeling possibilities with increased meshing efficiency and quality and also the power to explore early stage product design and complex system engineering from the nanometer scale of chip design to the mission level of aerospace and defense operating environments. The figure below represent the Ansys 2021 R2 workbench.

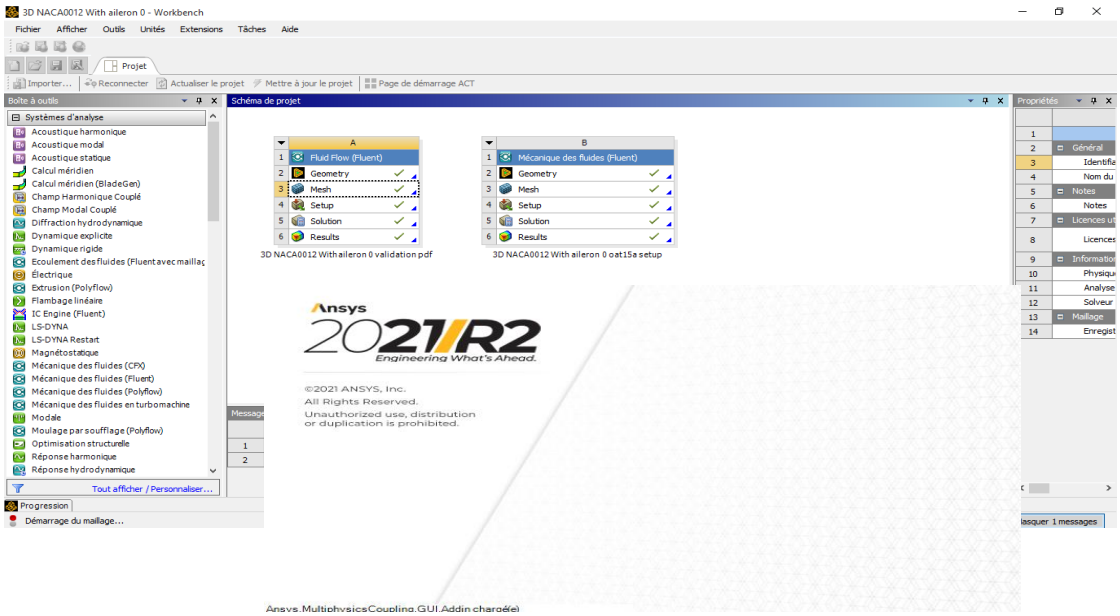

Figure IV-1 ANSYS 2021 R2 Workbench used for the study simulations

IV.2 Convergence criterion for the solutions

For the density-based solver, a residual is simply the time rate of change of the conserved variable (pressure, velocity, energy, kinetic energy k, and dissipation rate ε) of the problem between the current iteration and the previous iteration for each calculation step, which means that the residual measures the local imbalance of a conserved variable in each control volume. As a result, for each of the equations being solved, every mesh cell in the model will have its own residual value and in the iterative numerical solution will never be exactly zero. We set their minimum value to 10^6 and display them to monitor the solution's progress.

For the chosen cases, the minimum number of iterations was set to 1200, and in certain cases, it reached 3000, to observe that the solution has converged and that the simulations were automatically forwarded to the last step of the iteration when the residuals are stabilized. It is also important to note that taking the relaxation factor into consideration is required since the under and over-relaxation factors influence the stability and convergence rate of the iterative process.

The under relaxation factor increases the stability while over relaxation increases the rate of convergence. Additionally, the lift and drag coefficients were checked to examine the converged solution. The results are shown in Figure IV-2.

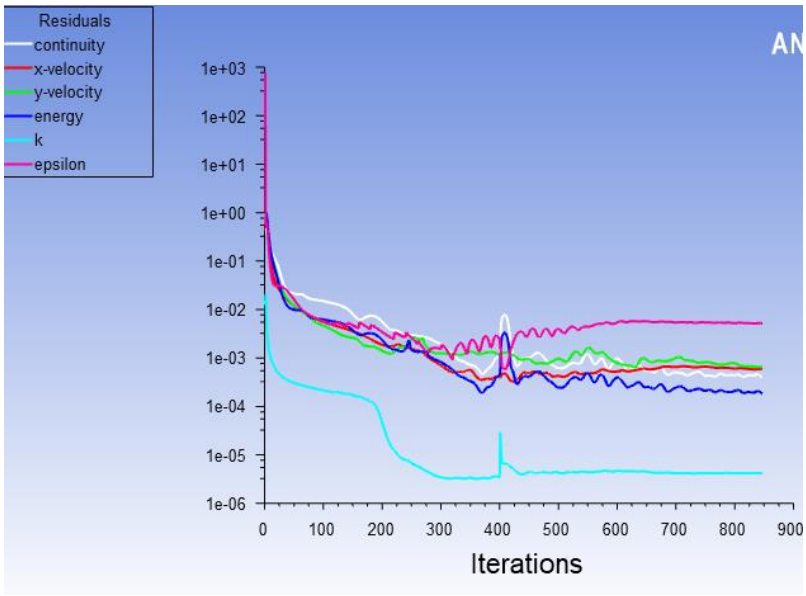

Figure IV-2 Fluent residuals graph to check convergence

IV.3 Numerical simulation on airfoils without control surface

The initial simulations have mostly been validations of cases without control surfaces to determine the optimum calculation strategy to use before proceeding on to cases of numerical modeling of control surfaces that determine the effect of these surfaces, and various factors had to be provided first such as the choice of a meshing methodology to conduct different deflections efficiently, the sensitivity of turbulence models, and also of the fluid domain.

IV.3.1. Fluid Domain Sensitivity

In order to ensure that the results are independent of the Fluid Domain Geometry, the pressure coefficient distribution of three configurations is compared to the values obtained by RAE. This case was carried out to demonstrate the use of WIND and associated programs for simulating two-dimensional turbulent, transonic flows over the RAE2822 airfoil. Additionally, the experimental data consists of surface pressure (Cp) measurements, as published in Ref [56].

This study assumes freestream flow conditions, as shown in the table below. Based on a chord length of 0.3048 m, these conditions correspond to a Reynolds number of 6.5 million. The static pressure was calculated using the given Reynolds number and Mach number, as well as an assumed static temperature.

Table 6.The free-stream conditions for the three cases of RAE2822

First Case	
$\boldsymbol{R}_e$	$6.5\ 10^6$
M	0.729
AOA	2.31°
T (k)	255.55
P (Pa)	108987.8

Data from a wind tunnel experiment are available for comparison with CFD FLUENT results using k-w SST models with varying fluid domain configurations. The following table represents the fluid domain details used for the study around a RAE2822 airfoil.

Table 7.Details of the fluid domin used for the study around a RAE2822 airfoil.

	Dimensions	N° Nodes	N° Elements	Orthogonal Quality
1^{st} Geometry	$5c \times 10c$	111345	110400	0,95705905622887
2^{nd} Geometry	$10c \times 20c$	199160	198000	0,943291570839951
3^{rd} Geometry	$20c \times 30$	279168	277920	0,95947878870643

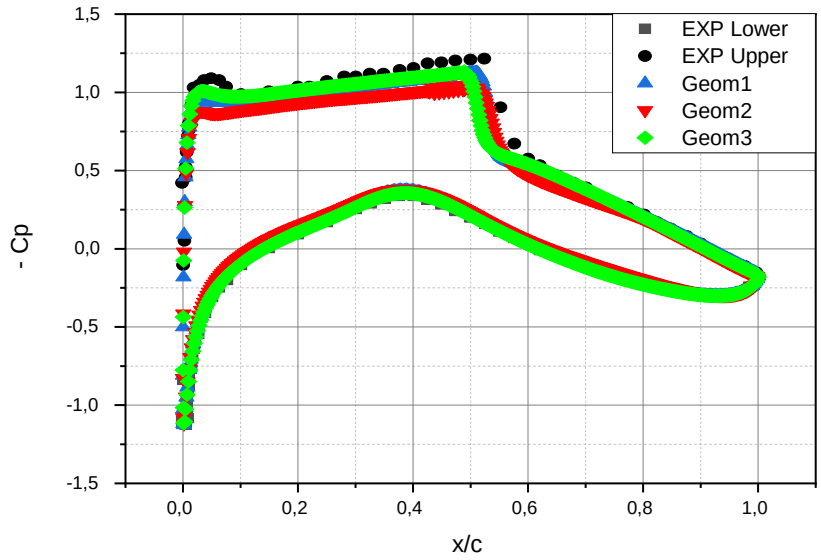

Figure IV-3 Pressure Coefficient Distribution over RAE2822 airfoil with different fluid domains for Case 1 in comparison with experimental measurements

.

The experimental data. The computational results for geometry 2 closely match the experimental data, with a slight improvement in the capture of the shock wave on the upper surface than the other geometries.

IV.3.2. Mesh Independence

To invest in the performance of a mathematical model for specific fluid flow studies, the mesh independence must reassure us that the findings produced are not impacted by the gradual increase of the mesh. If the computed results differ from the experiment, we cannot tell if this is due to an inaccurate physical model or an insufficient mesh resolution. As a result, many meshes were tested for the chosen setup, as indicated in the table.

We monitor one of the flow parameters that we are most concerned about after each simulation (in our case, this will be the pressure and aerodynamic coefficients). Therefore, for each mesh, we plot the evolution or variation curves of the selected parameter and observe if it continues to change. If so, we refine our mesh further, otherwise, we conclude that the solution has become independent of grid refinement.

Three cases of NACA0012 airfoil have been simulated for mesh independence testing and will be shown briefly in the following paragraphs.

IV.3.2.1. NACA0012 Airfoil

After multiple testing, In order to ensure that the results are independent of the mesh, we were able to determine the refinement criterion of the grids at which the computed solution becomes independent. The mesh utilized is a structured mesh that is compatible with the modeling software (Ansys, Fluent,...). The combination of a structured mesh with a multi-block geometry provides the following advantages: fewer mesh divisions as compared to an equivalent unstructured mesh and the numerical errors are reduced as the mesh is aligned with the flow.

The three NACA 0012 test cases are as follows:

- ✓ **Case one [102]:** The flow is attached and slightly supersonic near the leading edge of the airfoil in this case. This is a relatively benign situation in which the flow is only slightly transonic.
- ✓ **Case two [102]:** In this case, the flow contains a supersonic bubble on the leading edge of the top surface of the airfoil. Furthermore, the flow is slightly separated at the shock's bottom. Case 2 is a more challenging situation than Case 1.
- ✓ **Case three [102]:** A shock wave exists on the upper surface of the airfoil in this flow field at approximately x/c = 0.5, which is strong enough to produce considerable boundary layer separation. The difficulty in predicting the right

shock position and separation bubble led to the selection of this test case. The proper prediction of the shock location has been demonstrated to be substantially dependent on the turbulence model used.

Table 8.The free-stream conditions for the three cases of NACA0012

First Case		Second Case		Third Case	
$\boldsymbol{R_e}$	$9\ 10^6$	$\boldsymbol{R_e}$	$9\ 10^6$	$\boldsymbol{R_e}$	$9\ 10^6$
M	0.7	**M**	0.55	**M**	0.799
AOA	1.49°	**AOA**	8.34°	**AOA**	2.26°
T (k)	300	**T** (k)	300	**T** (k)	300
P (Pa)	58560	**P** (Pa)	74525	**P** (Pa)	51300

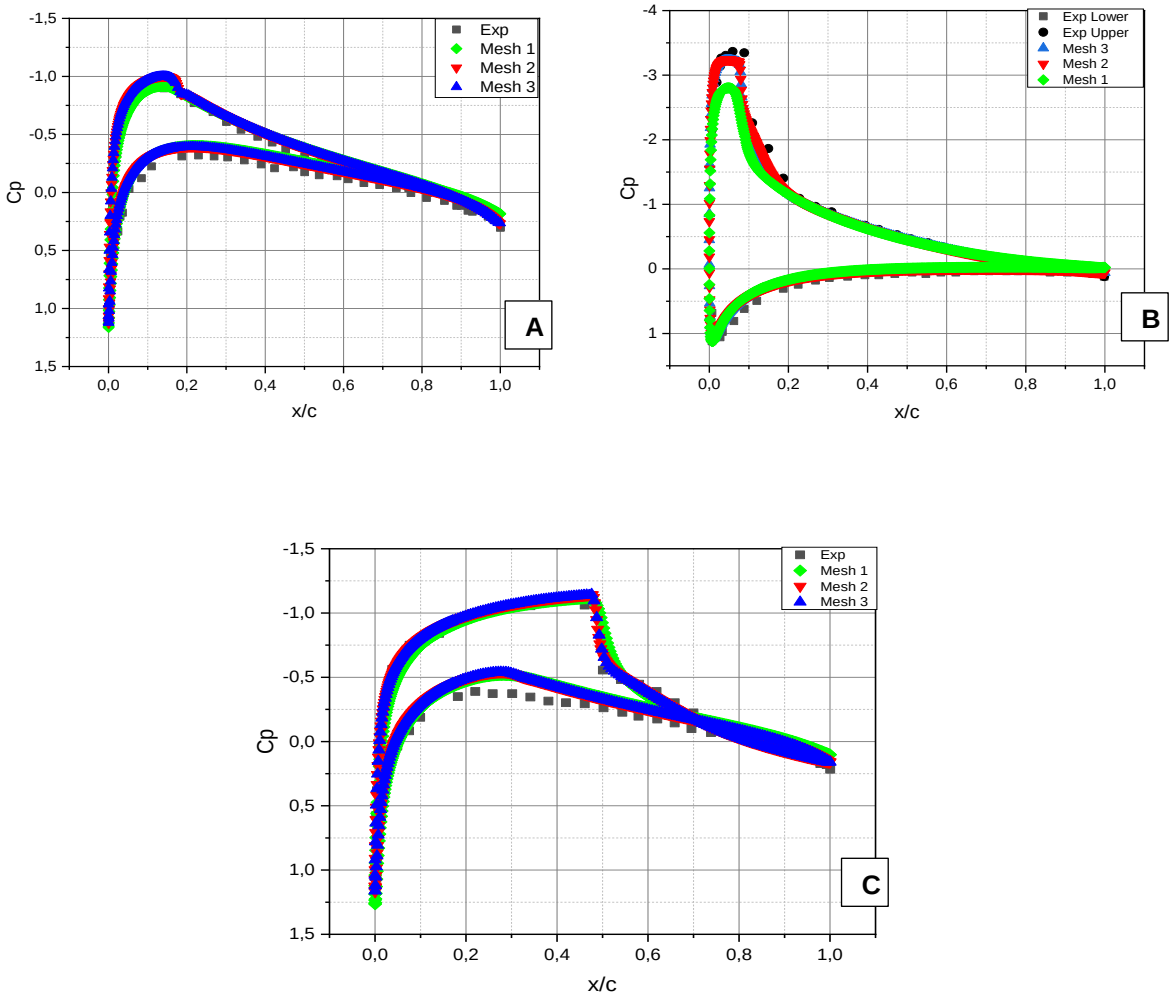

Figure IV-4 Mesh convergence analysis around the wing profile NACA0012 for Pressure Coefficient Distribution comparison with experimental mesurments **[102]** using K-w SST For A) Case1 B) Case2 C) Case3

The pressure coefficient distribution of three configurations is compared with those of experimental results under the freestream conditions summarized in the table abonve.

The impact of the geometry mesh on the simulation results can be seen in Figure N, which shows the experimental pressure coefficient distribution along with the numerical pressure coefficient of the three different mesh configurations.

A more significant indicator of solution convergence is to examine the convergence of the engineering quantity to be obtained from the analysis. Here it is the lift and drag coefficients on the airfoil of the three cases:

Table 9.The effect of mesh refinement on lift and drag coefficients

Case	Coefficient	Mesh 1	Mesh 2	Mesh 3
1 [102]	c_L	0.20002635	0.22536874	0.2298221
	c_D	0.022801925	0.009563627	0.009082803
2 [102]	c_L	0.80492389	0.88567511	0.88330025
	c_D	0.059151689	0.035470221	0.035666904
3 [102]	c_L	0.27541646	0.29825205	0.29800941
	c_D	0.051485947	0.034442067	0.034332912

For a viscous computation, it is useful to examine how well the boundary layers were resolved. One measure of this is the y+ values at the grid points in the boundary layers. The figure below contains information on the y+ values throughout the grid to examine the boundary layer at a certain location.

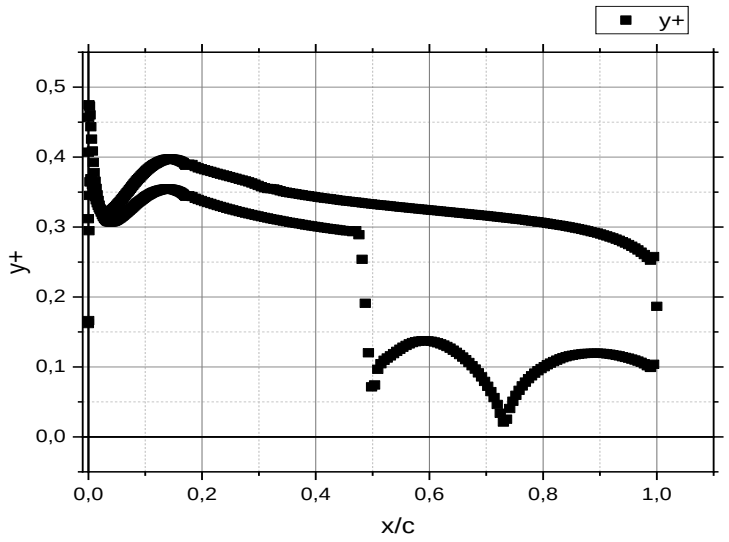

Figure IV-5 Wall Y Plus values in function of poistion (x/c)

IV.3.3. Turbulence Models Independence:

The RANS turbulence models differ in how they describe flow near walls, the number of additional variables solved for, and the significance of these variables. All of these models augment the Navier-Stokes equations with an additional turbulence eddy viscosity term. The role of turbulence model selection on shock wave predictions was investigated based on a well-defined fluid domain using three turbulence models, The Spalart Allmaras, k-epsilon, and k-w SST, to evaluate the influence of modeling techniques on simulation accuracy. Starting with:

IV.3.3.1. OAT15A Airfoil:

The tests were performed in the Onera S3CH transonic wind tunnel [50]. The relative thickness of the OAT15A wing profile is 12.3 percent, and the chord length is 0.23 m. The test run was done at a Reynolds number of 3 million for upstream Mach numbers (M) of 0.73 and 0.75, and angles of attack (AOA) of 1.5 and 3 degrees. Throughout the analysis, the total temperature and pressure remain constant at 300 K and 100000 Pa, respectively. The conditions in the three cases are given in the table below.

Table 10.The conditions for the three cases of OAT15A airfoil

First Case		Second Case		Third Case	
$\boldsymbol{R_e}$	$3\ 10^6$	$\boldsymbol{R_e}$	$3\ 10^6$	$\boldsymbol{R_e}$	$3\ 10^6$
M	0.73	**M**	0.73	**M**	0.75
AOA	1.50°	**AOA**	3°	**AOA**	3°
T (k)	300	**T** (k)	300	**T** (k)	300
P (Pa)	10^5	**P** (Pa)	10^5	**P** (Pa)	10^5

Table 11.The lift and drag coefficients on the OAT15A airfoil of the three cases computed with different turbulence models.

Case	Coefficient	$\boldsymbol{SA}$	$\boldsymbol{K-\varepsilon}$	$\boldsymbol{K-w\ SST}$
1 [50]	$\boldsymbol{c_L}$	0.66096391	0.80238946	0.59874732
	$\boldsymbol{c_D}$	0.023029656	0.02756204	0.032579006
2 [50]	$\boldsymbol{c_L}$	0.91791901	0.84828335	0.87397126
	$\boldsymbol{c_D}$	0.016189541	0.017079077	0.012414461
3 [50]	$\boldsymbol{c_L}$	0.87534352	1.1509871	0.77470448
	$\boldsymbol{c_D}$	0.027744219	0.09606263	0.055761978

The lift and drag coefficients on the OAT15A airfoil of the three cases computed with different turbulence models are shown in the previous table and The pressure distribution that characterize the behavior of this airfoil are shown in this figure.

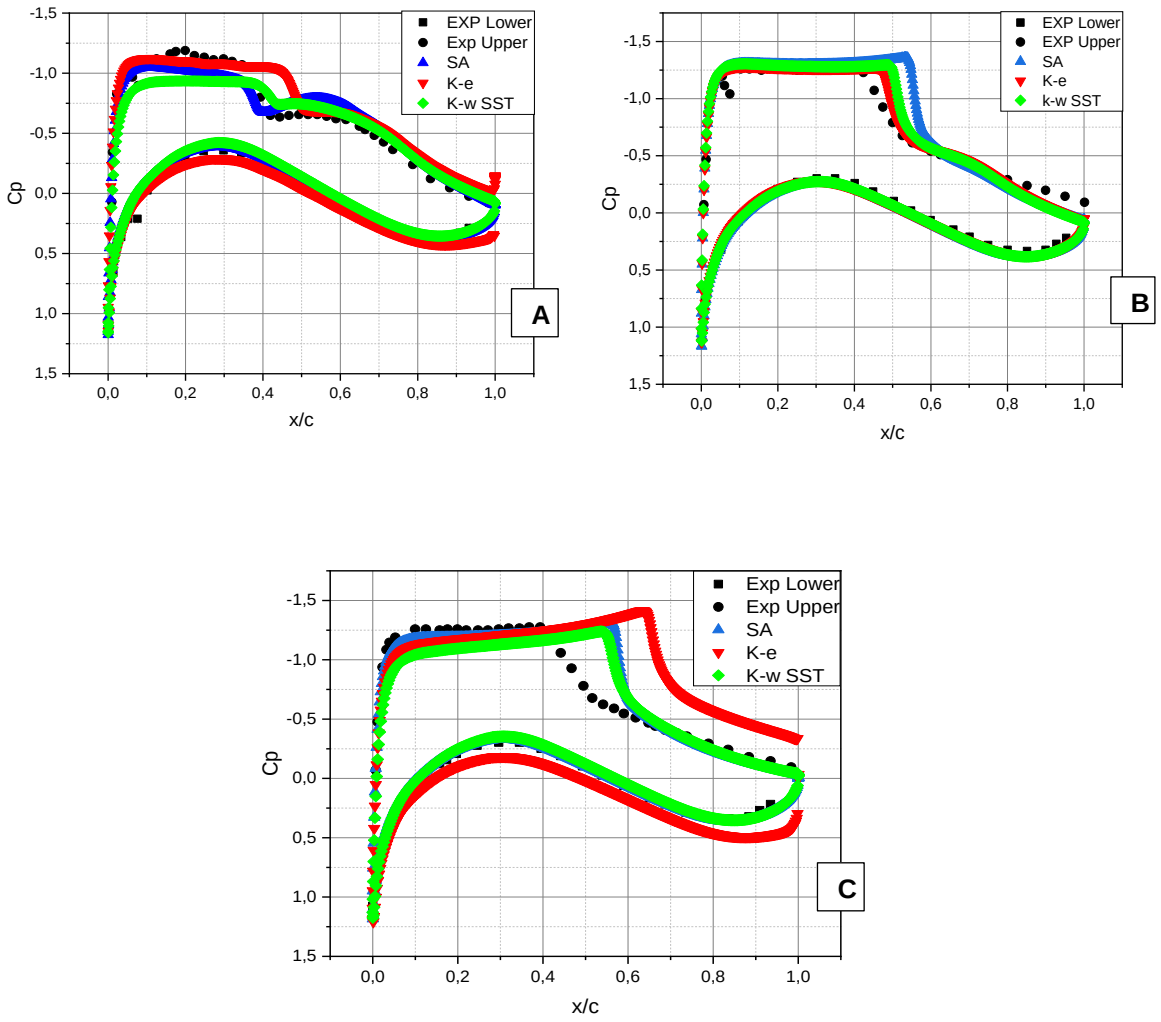

Figure IV-6 Pressure Coefficient Distribution Over OAT15A using Different Turbulence Models in comparison with experimental measurements [50] For A) Case1 B) Case 2 C) Case 3

IV.3.3.2. RAE2822 Airfoil

Two additional validation cases, reported in references **[104]** and **[105]** of the second and third case, respectively, investigate transonic flow over the RAE 2822 airfoil. And for the first case has already been discussed in detail previously in this chapter. The results are compared to the experimental data given in **[56], [104], [105]**.

All the cases assume freestream flow conditions that are already summarized in the table for a chord length of 0.3048 m. The static pressure was computed based on the specified Reynolds number, Mach number, and an assumed value of the static temperature of each case.

Table 12.The free-stream conditions for the three cases of RAE2822

First Case		**Second Case**		**Third Case**	
$\boldsymbol{R_e}$	$6.5\ 10^6$	$\boldsymbol{R_e}$	$7\ 10^6$	$\boldsymbol{R_e}$	$6.2\ 10^6$
M	0.729	**M**	0.73	**M**	0.75
AOA	2.31°	**AOA**	2.7°	**AOA**	2.81°
T (k)	255.55	**T** (k)	255.55	**T** (k)	255.55
P (Pa)	108987.8	**P** (Pa)	1170656	**P** (Pa)	1009217

The table below provides the aerodynamic coefficients of the numerical findings and the available experimental data.

Table 13.The aerodynamic coefficients of the numerical findings and the available experimental data

Case	**Coefficient**	**Exp**	$\boldsymbol{SA}$	$\boldsymbol{K-\varepsilon}$	$\boldsymbol{K-w\ SST}$
1 [56]	$\boldsymbol{c_L}$		0.68656391	0.65622525	0.65521136
	$\boldsymbol{c_D}$		0.016515475	0.017899552	0.01295984
2 [104]	$\boldsymbol{c_L}$	0.7894	0.80956958	0.79545672	0.80973019
	$\boldsymbol{c_D}$	0.01928	0.019459863	0.018324094	0.01596989
3 [105]	$\boldsymbol{c_L}$		0.8163032	0.79882771	0.7950928
	$\boldsymbol{c_D}$		0.030816481	0.029137578	0.02631775

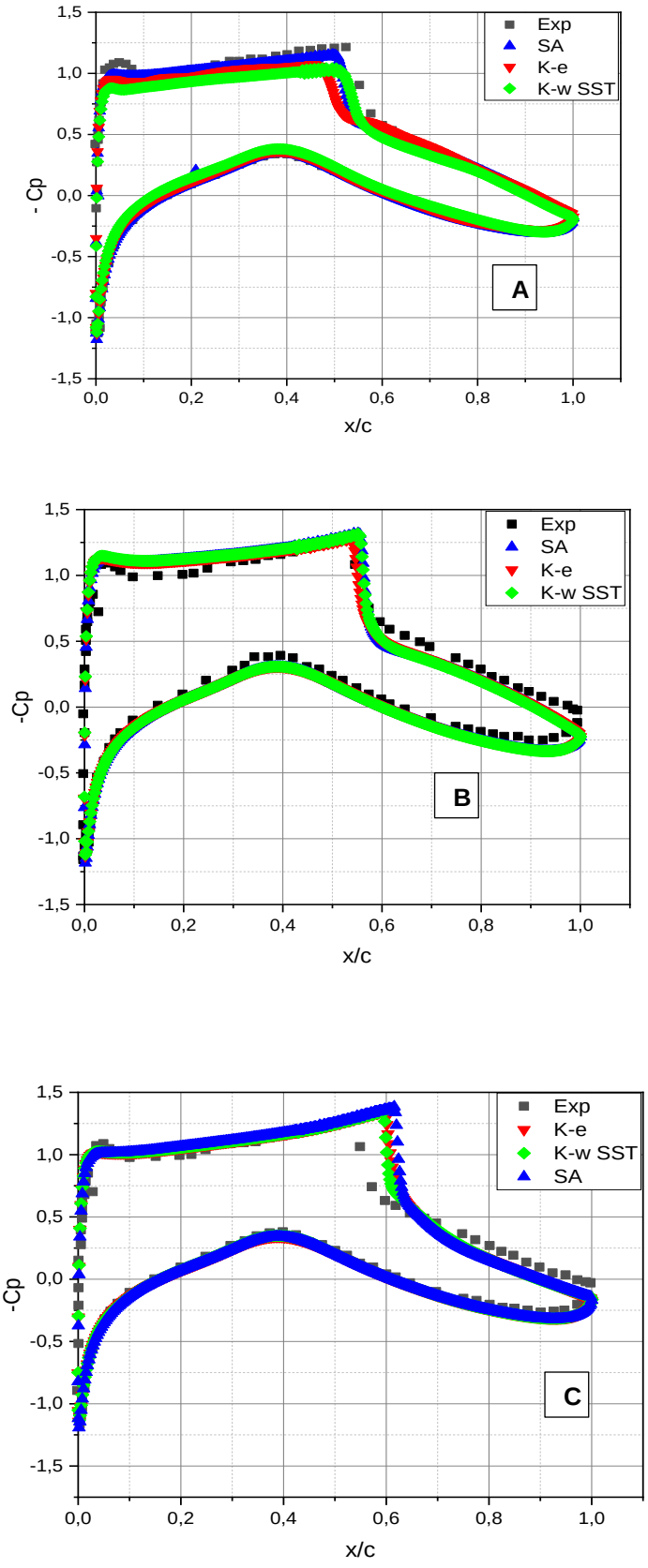

Figure IV-7 Pressure Coefficient Distribution Over RAE2822 using Different Turbulence Models in comparison with experimental results For A) Case1 [56] B) Case2 [104] C) Case3 [105].

IV.3.3.3. NACA0012 Airfoil

The NACA 0012 test cases used for validation are based on Harris's experimental work **[102]**. The data consists mostly of surface pressure observations. These simulations have been widely used to verify a broad range of flow solvers, including Navier-Stokes codes. Attached and separated transonic flows are included in the three test situations. As a result, these cases are suitable for detecting turbulence modeling and numerical errors related with transonic flow fields.

Detailed information regarding the upstream conditions has already been supplied in this chapter and collected in Table IV.10

The figures in this section compare the simulated surface pressure coefficients to experimental data for three separate cases based on three different airfoils, adopting a well-defined fluid domain for the simulation using various turbulence models.

The negative of the pressure coefficient is frequently presented in plots of pressure coefficients for the airfoil to indicate that the lower pressure region is on top and the high-pressure region is on the bottom surface.

The aerodynamic characteristics (C_l, C_d) of the numerical results are compared to those of the experimental data in the table below.

Table 14.The aerodynamic coefficients of the numerical findings for the chosen cases [102]

Case	Coefficient	SA	$K-\varepsilon$	$K-w\ SST$
1	c_L	0.20507282	0.19807173	0.20002635
	c_D	0.026794841	0.02872172	0.02280192
2	c_L	0.83883901	0.79549284	0.80492389
	c_D	0.065359363	0.06626593	0.05915168
3	c_L	0.29007641	0.27541646	0.24538453
	c_D	0.05075917	0.05148594	0.04504484

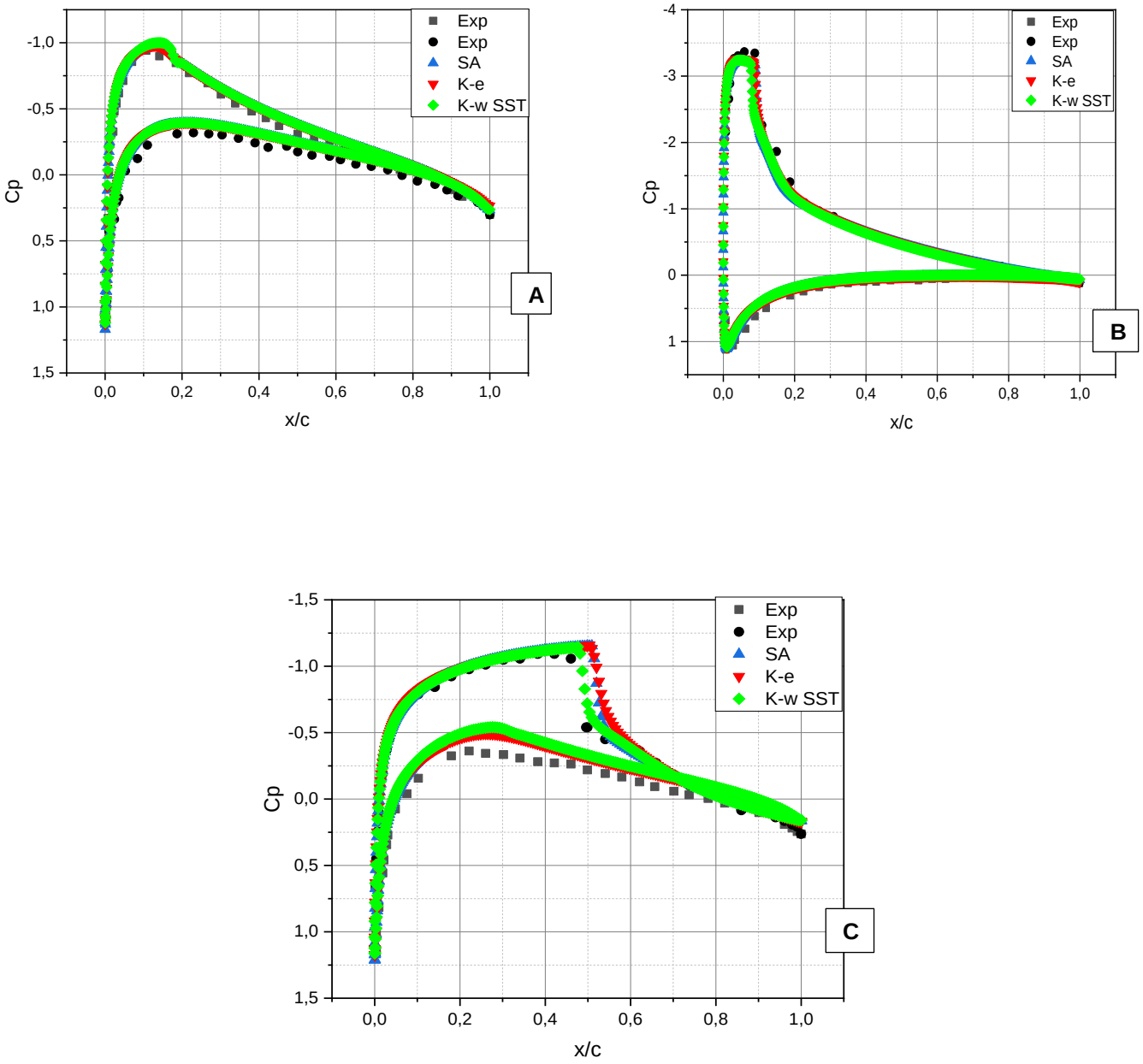

Figure IV-8 Pressure Coefficient Distribution Over NACA0012 using Different Turbulence Models For A) Case1 B) Case2 C) Case3 in comparison with experimental reults [102].

IV.4 Validation of 3D simulation case

IV.4.1. ONERA M6 Wing

The Onera M6 wing is a typical CFD validation case for external flow due to its shape combined with the complexity of transonic flow (i.e.: local supersonic flow, shocks, and turbulent boundary layer separation). It has essentially become a standard for CFD codes due to its use as a validation example in several CFD publications.

IV.4.1.1. Geometry and case specification

Bernard Monnerie and his colleagues constructed the ONERA M6 wing in 1972 as part of the AGARD collaboration to serve as experimental support for three-dimensional flow research at the transonic speed at high Reynolds numbers and for the validation of numerical modeling of flows. It was tested in a wind tunnel at various angles of attack up to 6 degrees and transonic Mach values (0.7, 0.84, 0.88, 0.92). Based on the mean aerodynamic chord, the Reynolds values were around 12 million. Schmitt and Charpin detailed the wind tunnel testing in the 1979 AGARD Report AR-138 **[56]**. The ONERA M6 is a half-span wing. The wing is swept and consists of a symmetrical profile. It has no twist, as seen by the wing dimensions in Figure IV.8:

Aspect ration $A = 3.8$

Taper ration $\lambda = 0.56$

Sweep angle $\Lambda_{25\%} = 26.7°$

ROWS OF PRESSURE TAPS

N°	y/b	upper	under
1	0.20	23	11
2	0.44	23	11
3	0.65	23	11
4	0.80	23	11
5	0.90	31	14
6	0.95	31	14
7	0.99	31	14

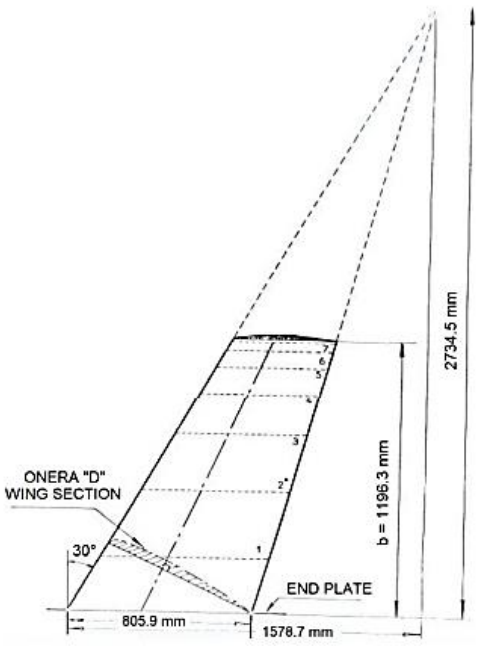

Figure IV-9 Geometric layout of the ONERA M6 wing [106]

Table 15.ONERA M6 wing geometry.

Span, b	1.1963 m
Mean Aerodynamic Chord, c	0.64607 m
Aspect Ratio	3.8
Taper Ratio	0.562
Leading-edge Sweep	30.0°
Trailing-edge Sweep	15.8°
Twist	NO

The free-stream conditions chosen for this validation case are shown below:

Table 16.The free-stream conditions for ONERA M6 Wing

$\boldsymbol{R_e}$	$11.72\ 10^6$
M	0.839
AOA	3.06°
T (k)	272
P (Pa)	104470

IV.4.1.2. Mesh Independence

For the simulations using ANSYS MESHING, an unstructured mesh was generated that was composed of small tetrahedral grids near the region of interest, which was the wing, and larger sizes further away. A mesh independence study was tested and compared to the experimental findings (presented on the next page), these mesh divisions produced precision while allowing complicated gradients around the wing to be resolved. The final step in the meshing process is to determine the model's boundary conditions provided in the Table IV-13

Table 17.Mesh metrics for the first and second grid around ONERA M6 wing

	1^{st} **Mesh**		2^{nd} **Mesh**	
N° Nodes	1839830		553883	
N° Elements	5345165		2043380	
Orthogonal Quality	**min**	0,74792	**min**	0,72391
	moy	0,99849	**moy**	0,96835
Skewness	**max**	0,23277	**max**	0,18782
	moy	0,0015123	**moy**	0,010433

Mesh metrics are generally used to assess mesh structure situations on various bases, as I explained in Chapter 3 about mesh performance measures. One of these mesh indicators for assessing the grid's structure set is “Orthogonal Quality”

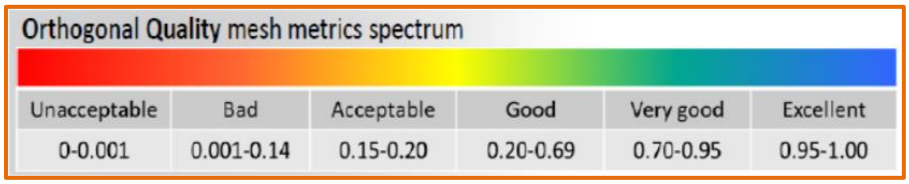

Figure IV-10 Fluent Orthogonal Quality mesh metrics spectrum [107].

The important thing to remember about 'Orthogonal Quality' is that 0 is the worst and 1 is the best as shown in the figure above. It is also commonly used to evaluate the mesh shape quality including the skewness of mesh structures.

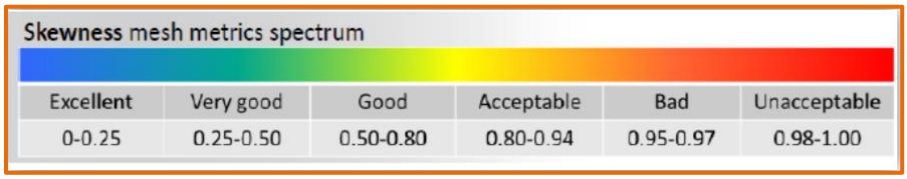

Figure IV-11 Fluent Skewness mesh metrics spectrum [107].

The figures in the next two pages illustrates the numerical findings in comparison with the experimental results, In order to examine the mesh sensitivity as well as the turbulence models. The choice fell on the ONERA M6 Wing to compute at 6 sections the surface pressure distributions.

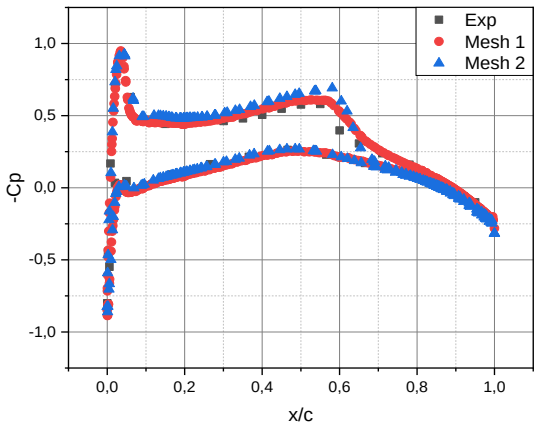

y/b= 0.2

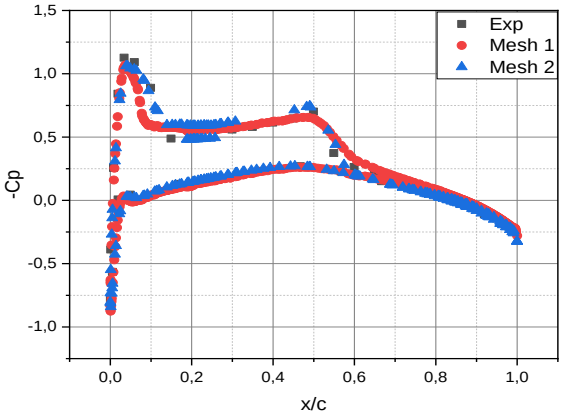

y/b= 0.44

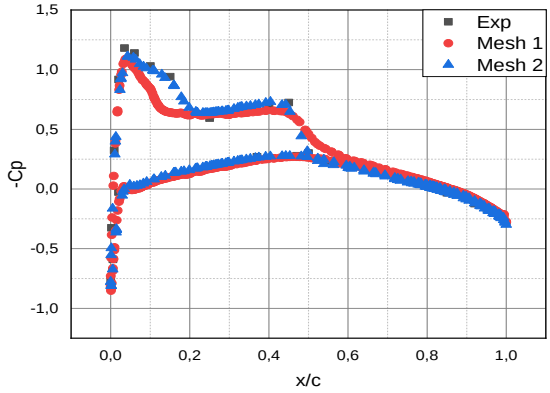

y/b= 0.65

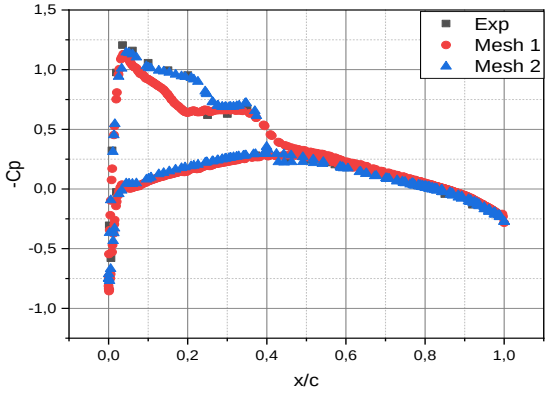

y/b= 0.8

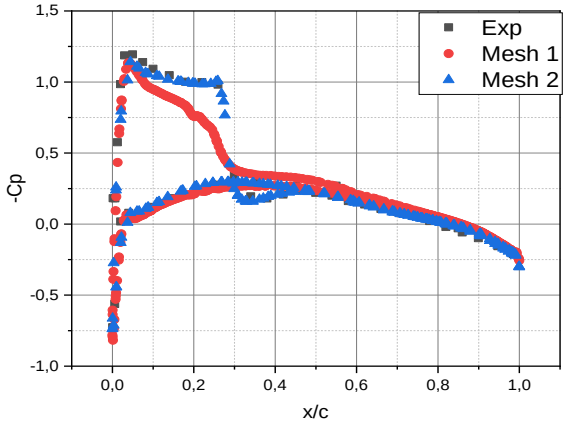

y/b= 0.9

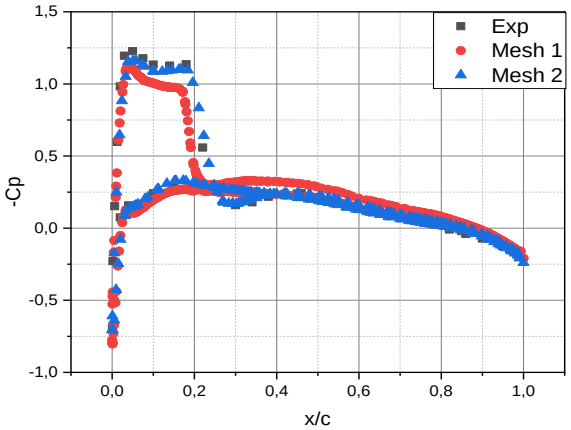

y/b= 0.95

Figure IV-12 Pressure Coefficient Distribution over Onera M6 Wing at 6 sections compared to experimental [106] for mesh independence study using the Spalart-allmaras turbulence model

IV.4.1.3. Turbulence Models Sensitivity:

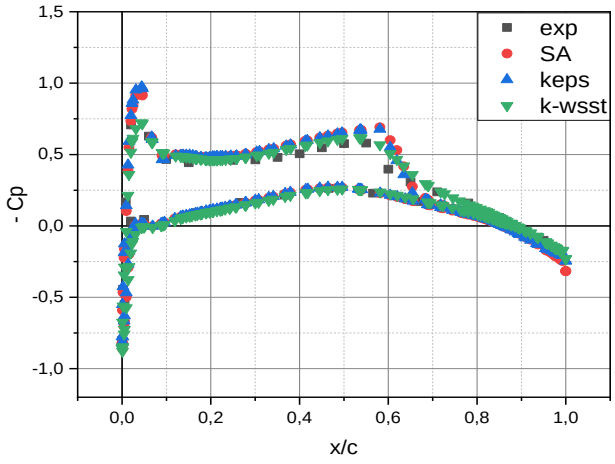

y/b= 0.2

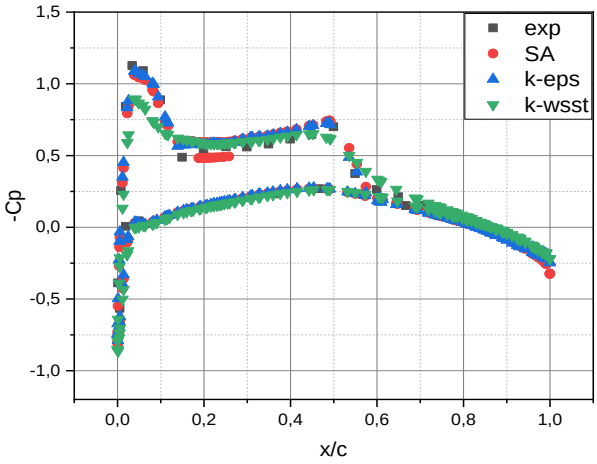

y/b= 0.44

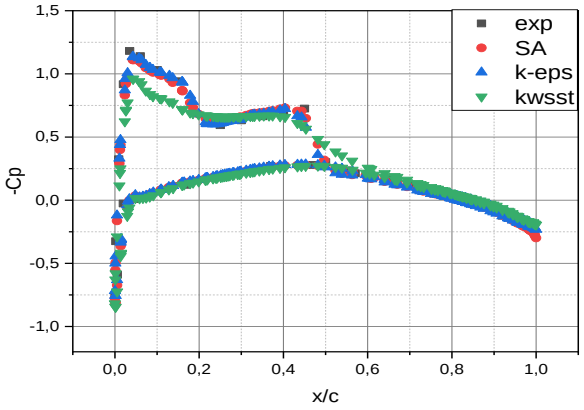

y/b= 0.65

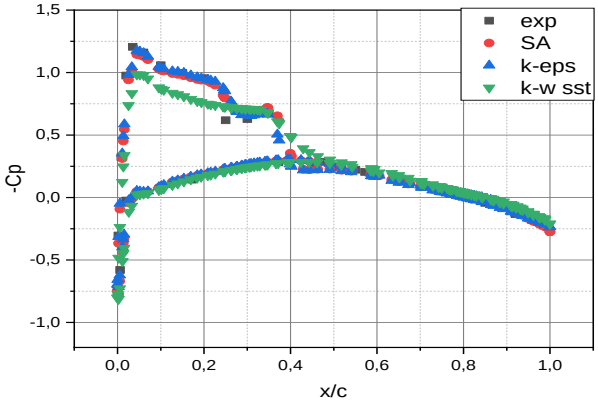

y/b= 0.8

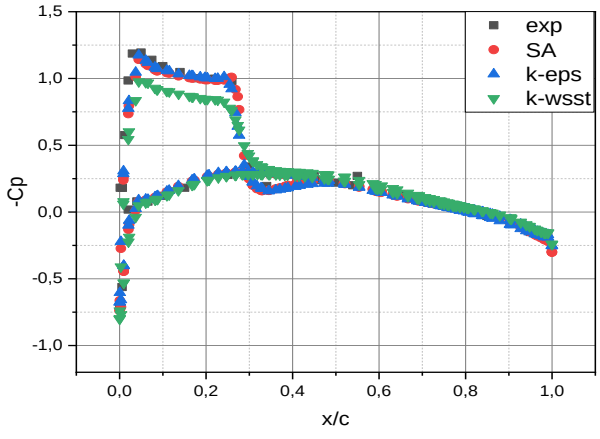

y/b= 0.9

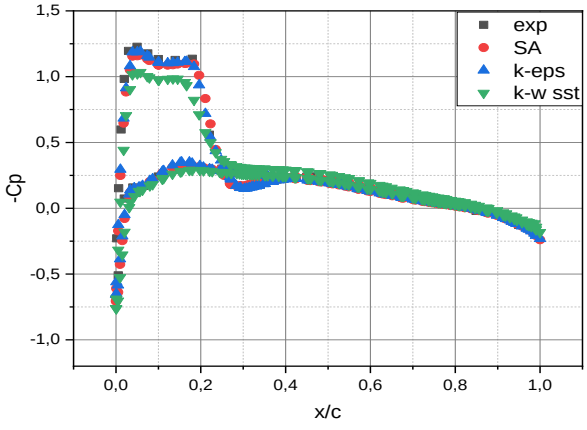

y/b= 0.95

Figure IV-13 Pressure Coefficient Distribution over Onera M6 Wing sections using different turbulence models in comparison with experimental results [106].

IV.5 Numerical simulation on OAT15A Airfoil with Spoiler at 30°

Fillola (2006) **[76]** investigates experiments performed in the T2 tunnel of ONERA Toulouse on a supercritical airfoil OAT15A with spoilers deflected. It analyzes results at $Mach = 0.73$, $AOA = 1.5°$, and $\delta_{sp} = 30°$, focusing on the recirculation zone behind the spoiler. The pressure curves seen behind the spoiler indicate a pressure plateau in this region. In this section, the independence of turbulence models is investigated and compared to the results published in reference **[76]** as shown in **Figure IV-14**

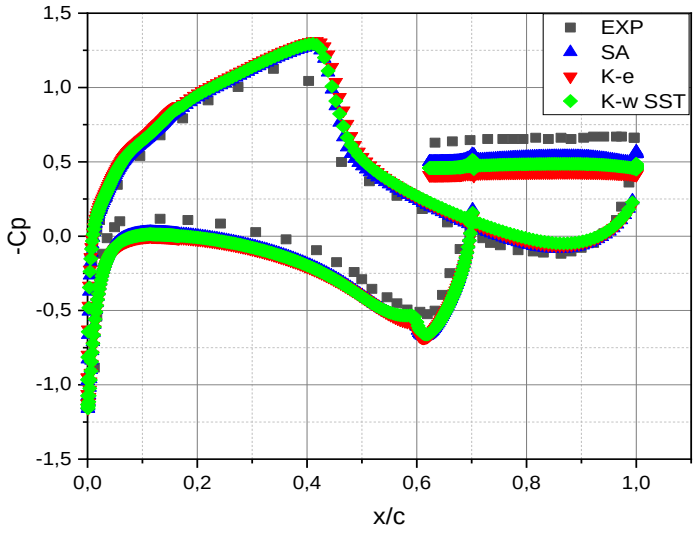

Figure IV-15 Pressure Coefficient Distribution over OAT15A Airfoil with the spoiler at an angle of deflection 30° using different turbulence models in comparison with experimental results of Fillola (2006) [76].

The following table provides the computed aerodynamic properties (lift and drag coefficients).

Table 18.The lift and drag coefficients on the OAT15A airfoil attached to Spoiler at 30° computed with different turbulence models to compare with the experimental [76].

Coefficient	Exp	SA	$K-\varepsilon$	$K-w\ SST$
c_L	-0.294	-0.2827240	-0.27214961	-0.30177806
c_D	0.981	0.95852949	0.95538103	0.97344124

IV.6 Comparative Numerical Studies

The process has been done by taking steady-state around the airfoils using the same chord length at the same upstream flow conditions. The main aim is to understand the aerodynamic characteristics of the airfoils and wings with and without control surface to reach a conclusion on which performs better under the same conditions. Modeling and numerical analysis have been carried out and the numerical results illustrated in the figures are compatible with those of the theory.

IV.6.1. NACA0012 Airfoil & OAT15A Airfoil without control surface:

A comparison between NACA 0012 and OAT15A airfoils has been made, by comparing the pressure coefficient distribution and pressure contour at $Mach = 0.73$, $\propto = 1.5$, and $R_e = 3.5 \times 10^6$ using 0.15m chord length, the results are given in **Figure IV-6** and **Figure IV-16** respectively.

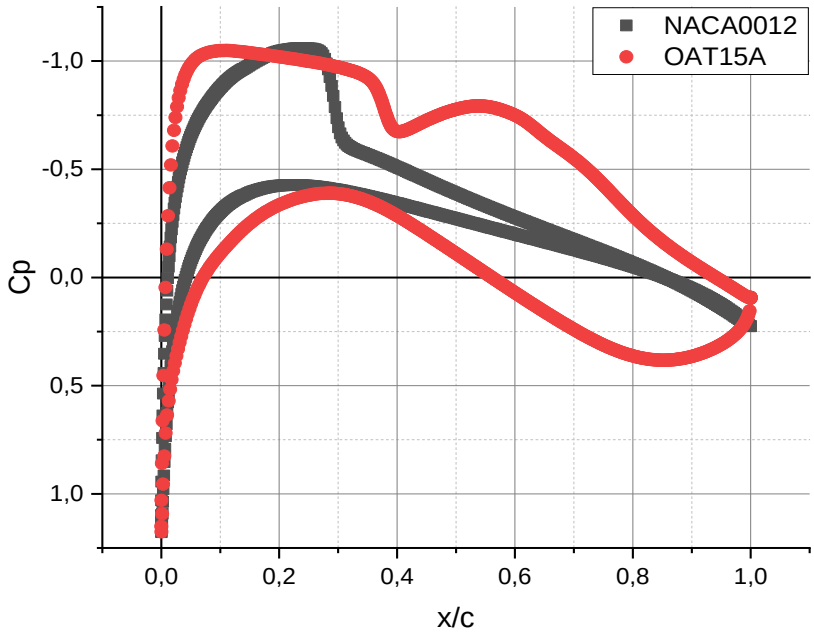

Figure IV-17 Pressure Coefficient Distribution Over NACA0012 in comparison with that of OAT15A at M= 0.73, AOA= 1.5, and $R_e = 3.5 \times 10^6$.

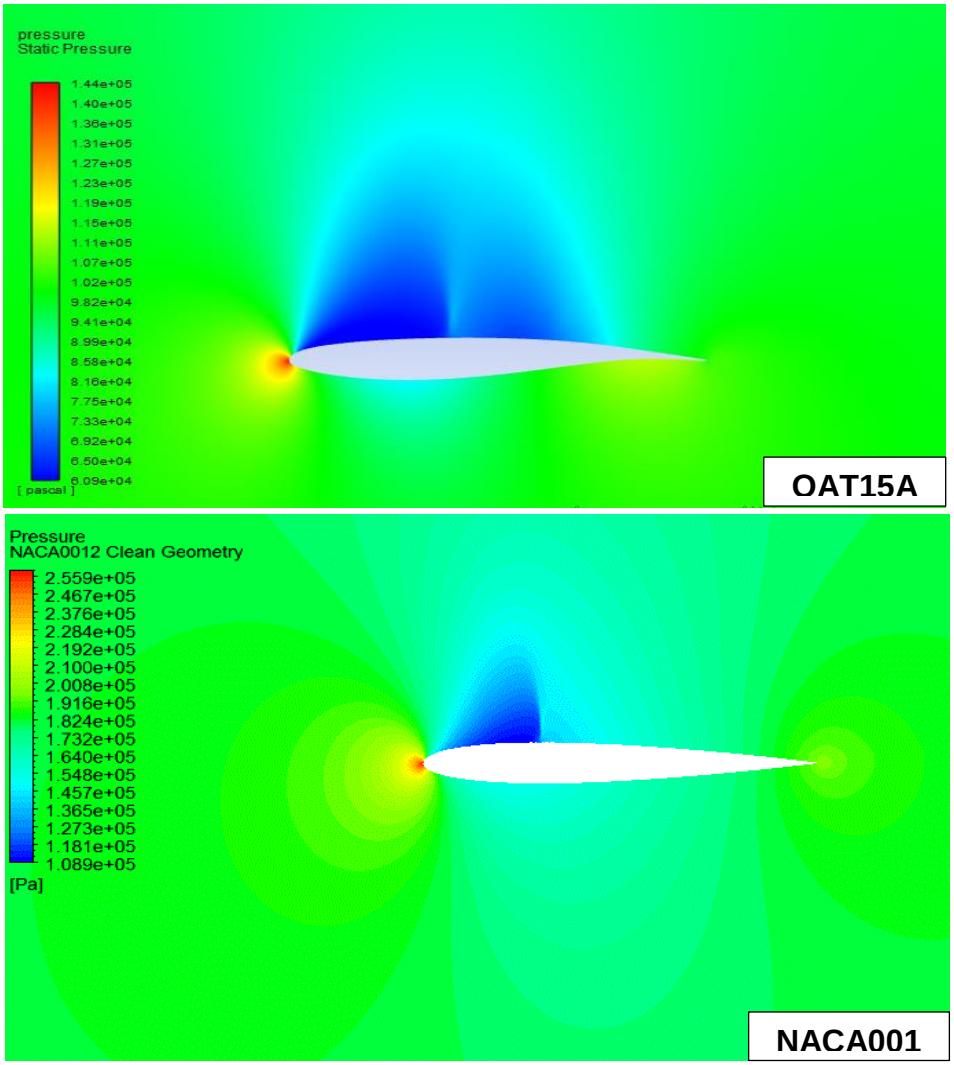

Figure IV-18 Pressure Contour Over NACA0012 airfoil in comparison with that of OAT15A airfoil without control surface at M= 0.73, AOA= 1.5, and $R_e = 3.5 \times 10^6$.

From these results, compared to the NACA0012 airfoil, the supercritical airfoil OAT15A creates more of its lift due to its more even pressure distribution over the upper surface. In addition to improved transonic performance, the supercritical airfoil enlarged leading edge gives it excellent high-lift characteristics.

Supercritical OAT15A airfoil has a flat-on-top look. As air moves across the top, it does not speed up nearly as much as over the NACA 0012 curved upper of the airfoil. This delays the onset of the shock wave and also reduces aerodynamic drag associated with boundary layer separation.

IV.6.2. NACA0012 airfoil without control surface at an angle of attack 0° & 1.5°

In order to capture the supersonic pocket over the NACA0012 airfoil without a control surface in a transonic regime, Pressure contours were plotted over that airfoil at AOA of 0° and 1.5°as shown in **Figure IV-19**

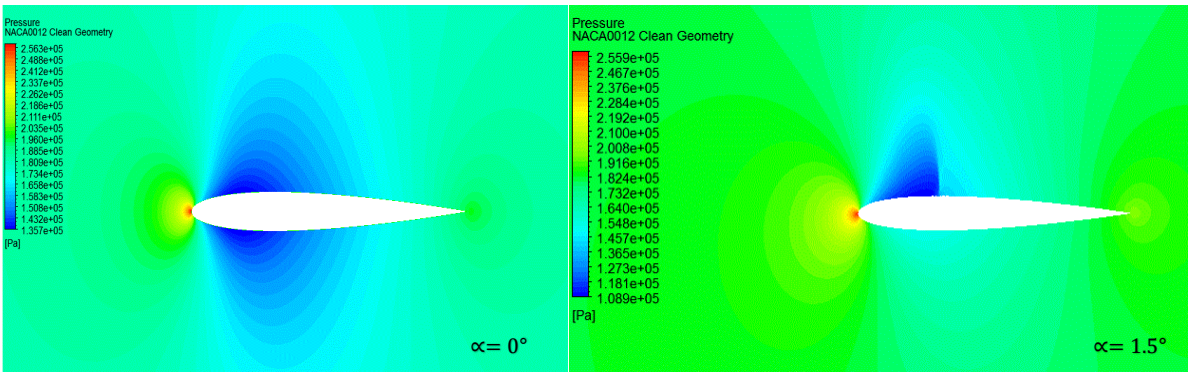

Figure IV-20 Pressure Contour Over NACA0012 without control surface at AOA of 0° and 1.5° under freestream conditions of M= 0.73 and $R_e = 3.5 \times 10^6$.

The pressure contour over the airfoil with the angle of attack 0 degree shows clearly a perfect symmetry of the physical phenomenon. It is noted for this case, that the depression is located in the vicinity of the maximum thickness of the profile and this on both the lower and the upper surface, the influence of the angle of incidence is also marked on the Figure as the variation of this angle induces an asymmetry of the flow which is accentuated with the increase in the angle of incidence. This increase also affects the position and the thickness of the shock wave.

IV.6.3. NACA0012 airfoil without control surface & NACA0012 Airfoil with Aileron at $\delta_A = 0°$

Prior to starting the comparative analysis, a computed pressure coefficient distribution was validated with the experimental data of the NACA0012 airfoil with aileron as published in reference [108] at a Mach number of 0.75 and angle of attack AOA=5 and angle of deflection $\delta_A = 0°$. The figure in the next page represents both the calculated and experimental pressure coefficient distributions

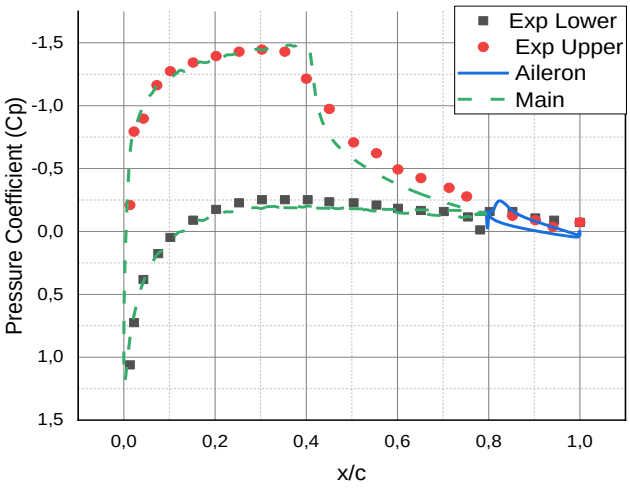

Figure IV-21 Pressure Coefficient Distribution Over NACA0012 with aileron in comparison with experimental results [108] at M= 0.75, AOA= 5, and δ_A= 0°

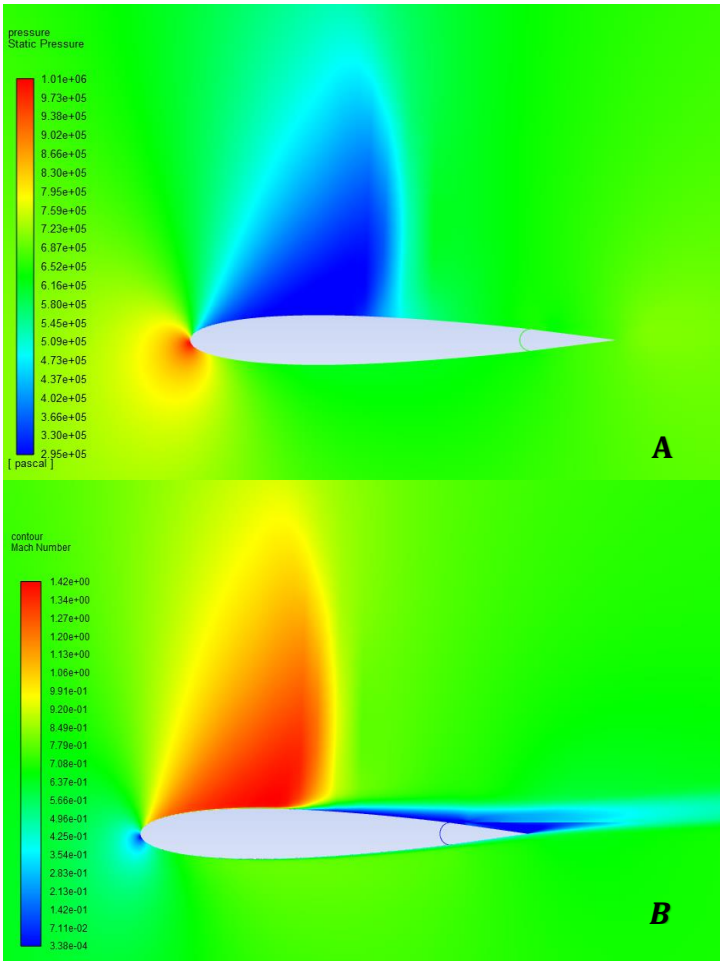

Figure IV-22 A) Pressure Contour B) Mach Number Contour over NACA0012 Airfoil with aileron at δ_A= 0°, Mach = 0.75, ∝= 5.

After this result, the following figure compares the distribution of the pressure coefficient of NACA0012 airfoil without control surface to NACA0012 Airfoil with Aileron at $\delta_A = 0°$, M= 0.73, AOA= 1.5, and $R_e = 3.5 \times 10^6$.

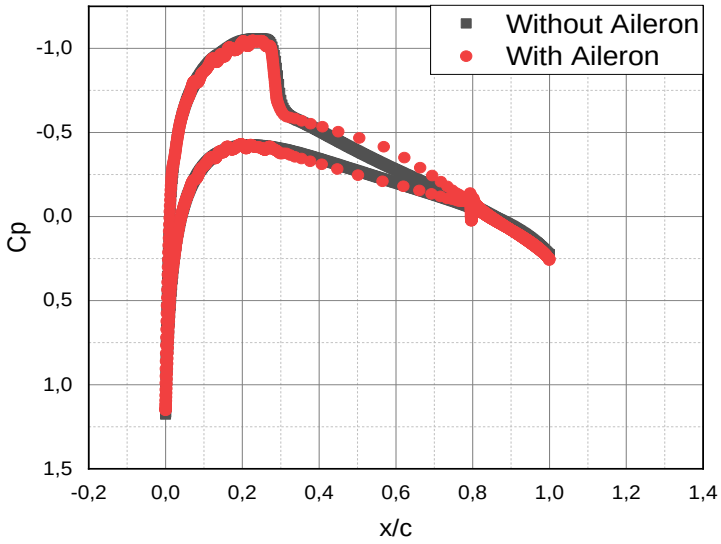

Figure IV-23 Pressure Coefficient Distribution Over NACA0012 without aileron compared to that of NACA0012 with aileron at δ_A= 0°, M= 0.73, AOA= 1.5

The figures below illustrate the pressure contours over NACA0012 without aileron and NACA0012 with aileron at $\delta_A = 0°$, M= 0.73, AOA= 1.5 and $R_e = 3.5 \times 10^6$.

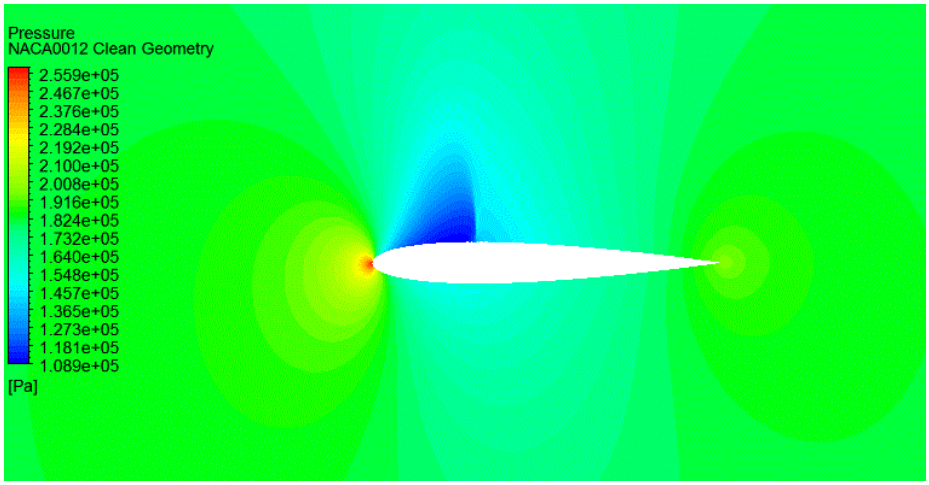

Figure IV-23 Pressure Contour Over NACA0012 without aileron at M= 0.73, AOA= 1.5, and $R_e = 3.5 \times 10^6$.

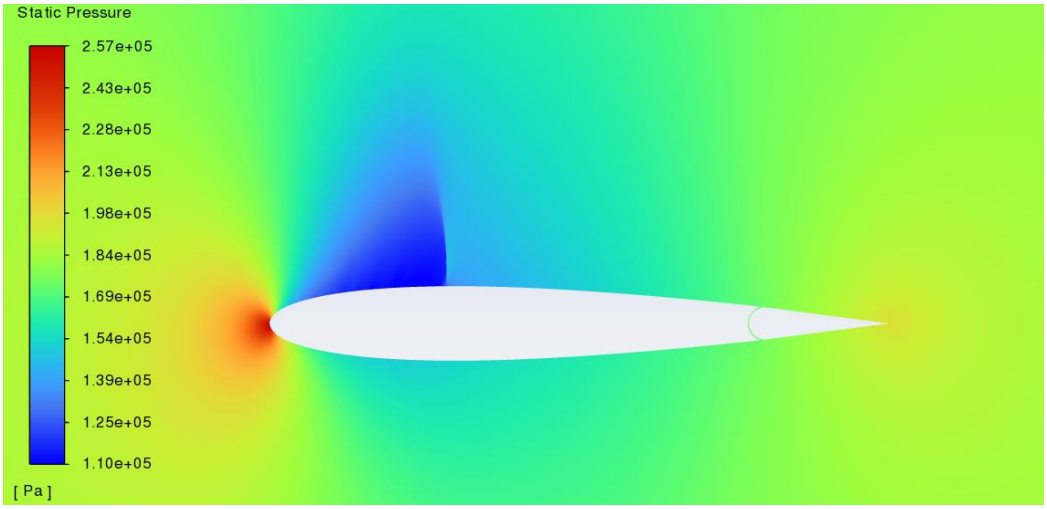

Figure IV-24 Pressure Contour Over NACA0012 with aileron at M= 0.73, AOA= 1.5, and $R_e = 3.5 \times 10^6$.

IV.6.4. Aileron Deflection Effects On Airfoils

The numerical results of the pressure distributions and pressure contours obtained on the OAT15A airfoil with aileron shows that beyond a certain deflection angle, detachments will appear on the upper surface ($\boldsymbol{\delta_A > 0}$) or on the lower surface ($\delta_A < 0$), and the return of the shock wave by increasing the aileron deflection.

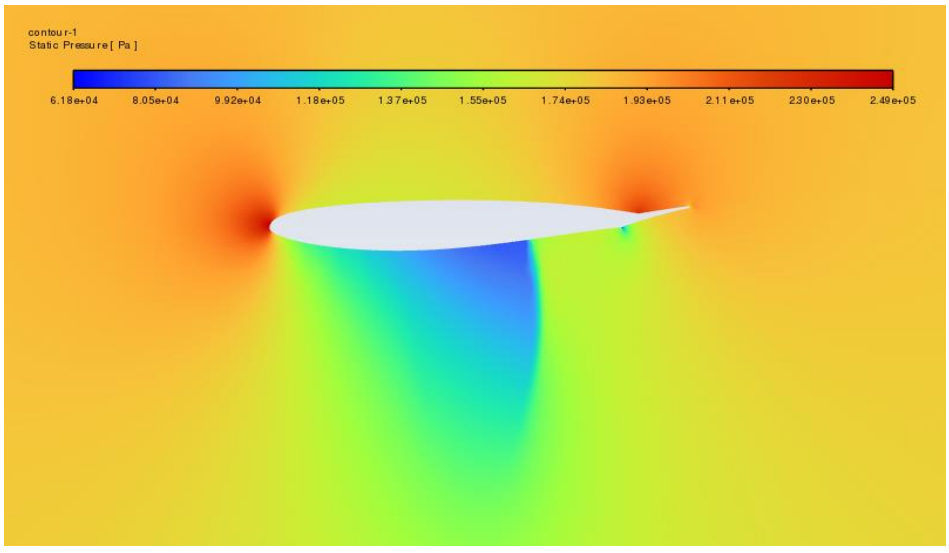

Figure IV-25 Pressure Contour Over OAT15A with aileron at : δ_A=-20 ,M= 0.73, AOA= 1.5, and $R_e = 3.5 \times 10^6$.

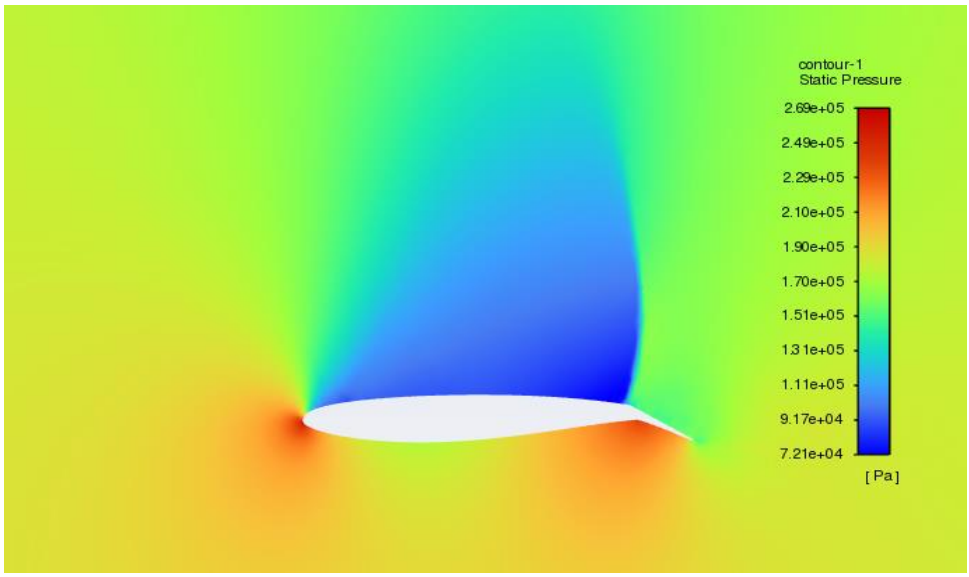

Figure IV-26 Pressure Contour Over OAT15A with aileron at : δ_A=+20 ,M= 0.73, AOA= 1.5, and $R_e = 3.5 \times 10^6$.

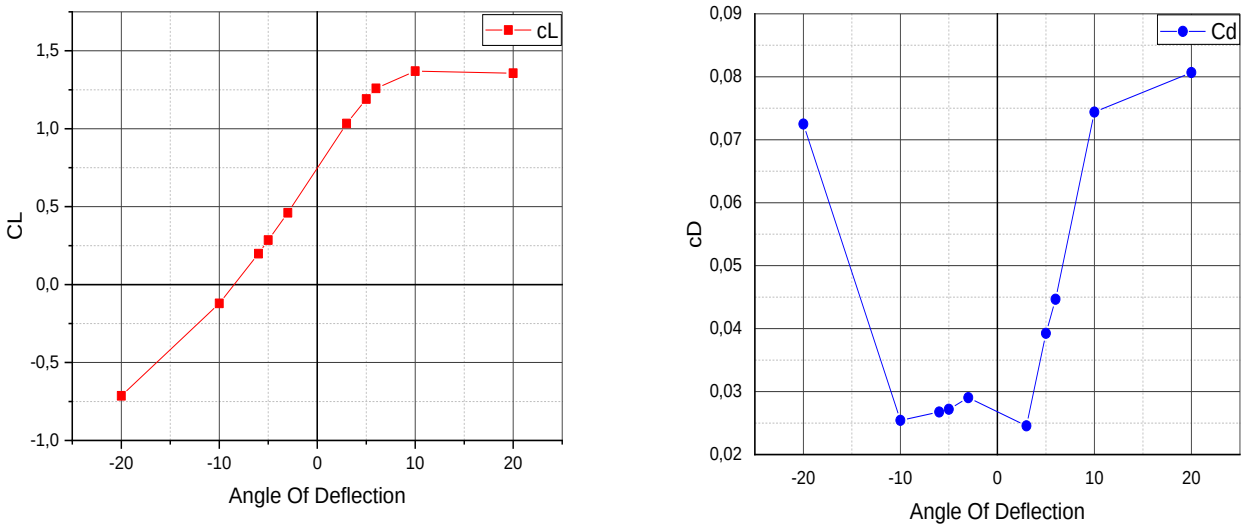

Figure IV-27 Lift and Drag Coefficients variation over OAT15A airfoil with aileron in function of angle of deflection at M=0.73, and $R_e = 3.5 \times 10^6$

The figure above is the Lift and Drag coefficient variation in function of angle of deflection and clearly represents the lift efficiency of the aileron connected to the OAT15A airfoil at ($Mach = 0.73, = 1.5°$, and the angle of deflection varying [-20,20]).

IV.6.5. Angle Of Attack Effect On OAT15A airfoil with Aileron at different deflection angles

To investigate the effect of angles of attack on the lift and drag coeffients at upstream Mach number of 0.73 for aileron angle of deflection: $\delta_A = \pm 3°$, $\delta_A = 6°$, $\delta_A = 20°$, the simulations were for different angles of attack as shown in the figure below.

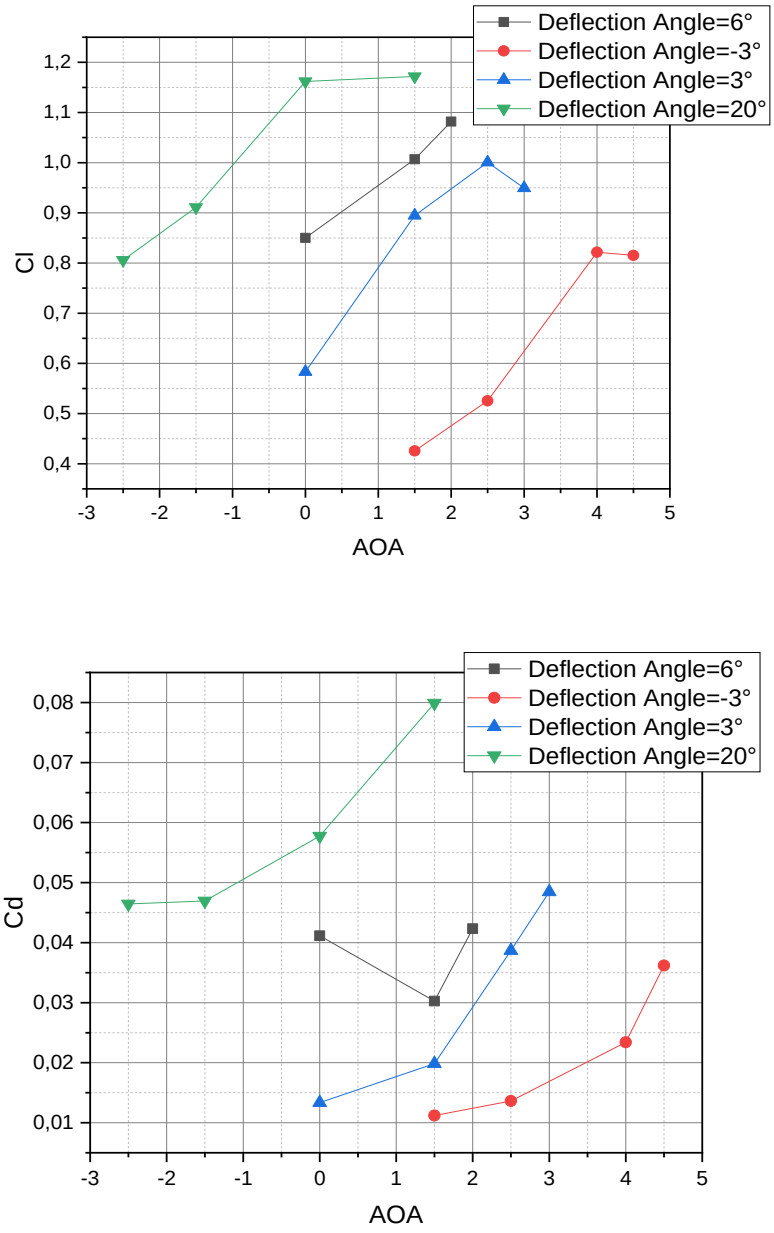

Figure IV-28 Lift and Drag Coefficients variation over OAT15A airfoil with aileron in function of angle of Attack at M= 0.73 and $\delta_A = \pm 3$, $\delta_A = 6°$, $\delta_A = 20°$

From the graphs , it is seen that the lift coefficient increases significantly as the angle of attack increases, however there is a limitation of increasing angle of attack since at angles of attack greater than those that provide the highest lift, the airfoil is seen to be stalled.

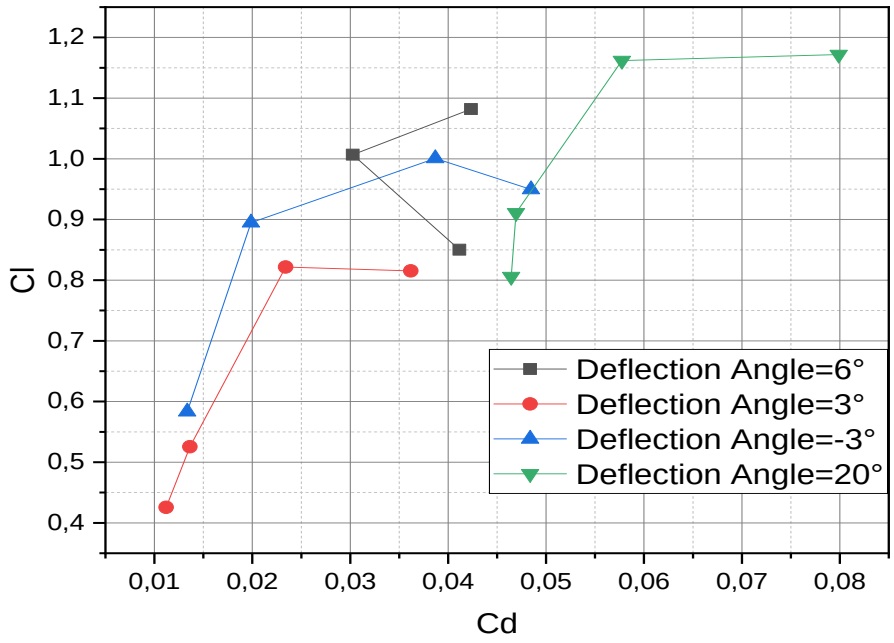

Figure IV-29 Drag Polar at M= 0.73, diffirent angles of attack over OAT15A airfoil with aileron for $\delta_A = \pm 3$, $\delta_A = 6°$, $\delta_A = 20°$

The figure represents a drag curve, often known as a drag polar (also called a "polar plot"). It is the relation between the drag coefficient (or drag force) on an airfoil and the coefficient of lift (or lift force) at various angles of attack at M= 0.73 for $\delta_A = \pm 3°$, $\delta_A = 6°$, and $\delta_A = 20°$.

IV.6.7. Flow description over OAT15A airfoil attached to Spoiler at $\delta_{Sp} = 30°$

The interest in spoilers is due to their capacity to generate drag and downforce. Deflecting a spoiler tends to increase the boundary layer on the upper surface of a profile because of the surface discontinuity. The spoiler creates a significant recirculation zone by joining its trailing edge and that of the profile. The study is conducted at $Mach = 0.73$, $\propto = 1.5$, and $\delta_{Sp} = 30°$.

The figures below illustrate the pressure and Mach number contours, as well as the velocity vectors. Respectively.

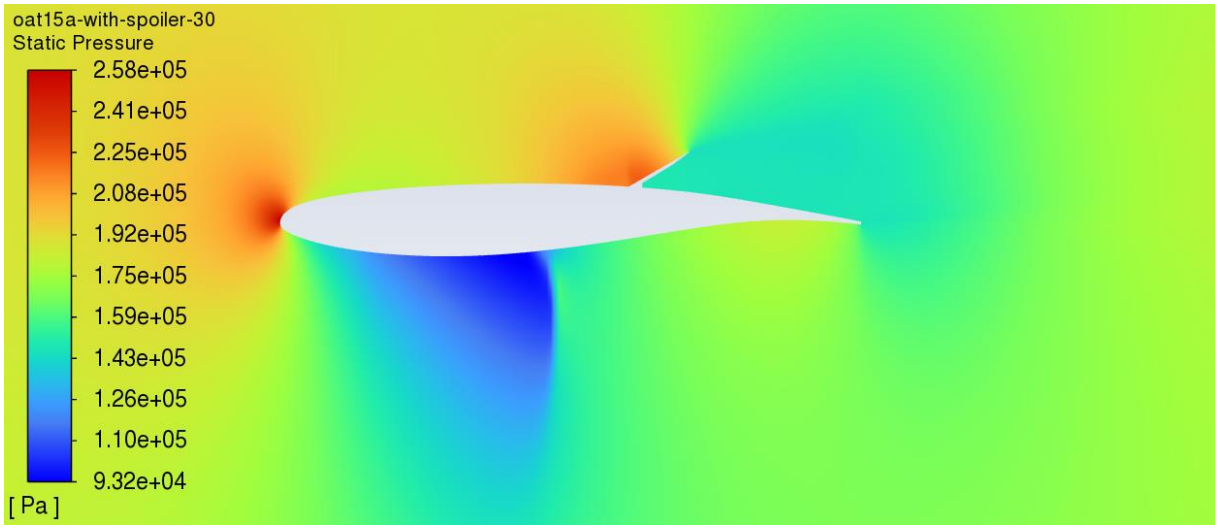

Figure IV-30 Pressure Contour over OAT15A Airfoil with Spoiler at δ_{Sp}= 30°, Mach = 0.73, ∝= 1.5, and $R_e = 3.5 \times 10^6$.

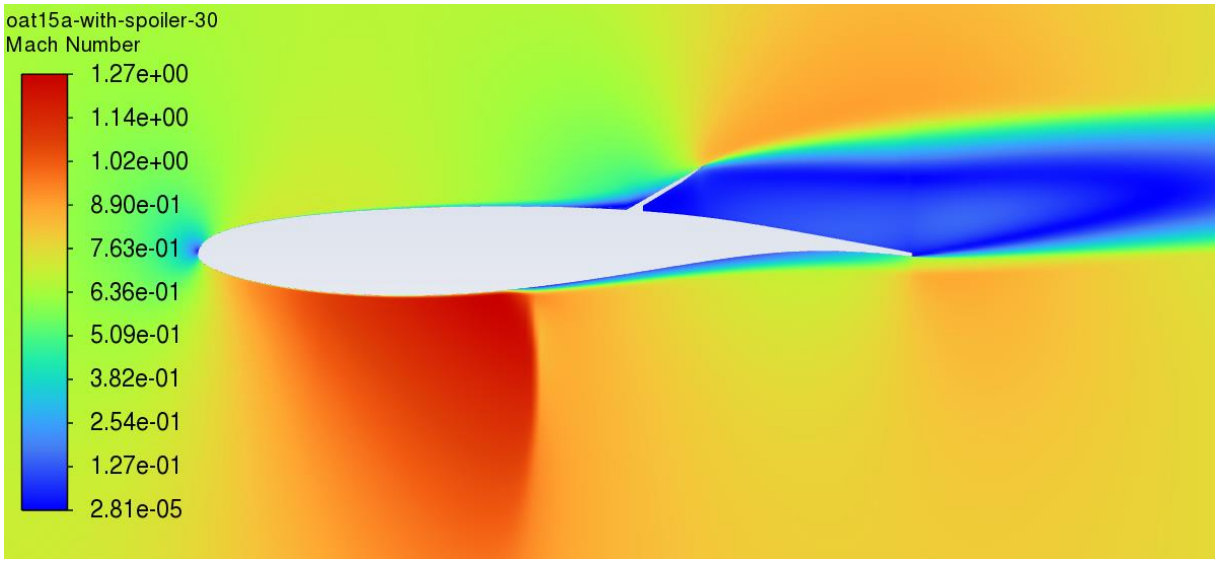

Figure IV-31 Mach number Contour over OAT15A Airfoil with Spoiler at δ_{Sp}= 30°, Mach = 0.73, ∝= 1.5, and $R_e = 3.5 \times 10^6$.

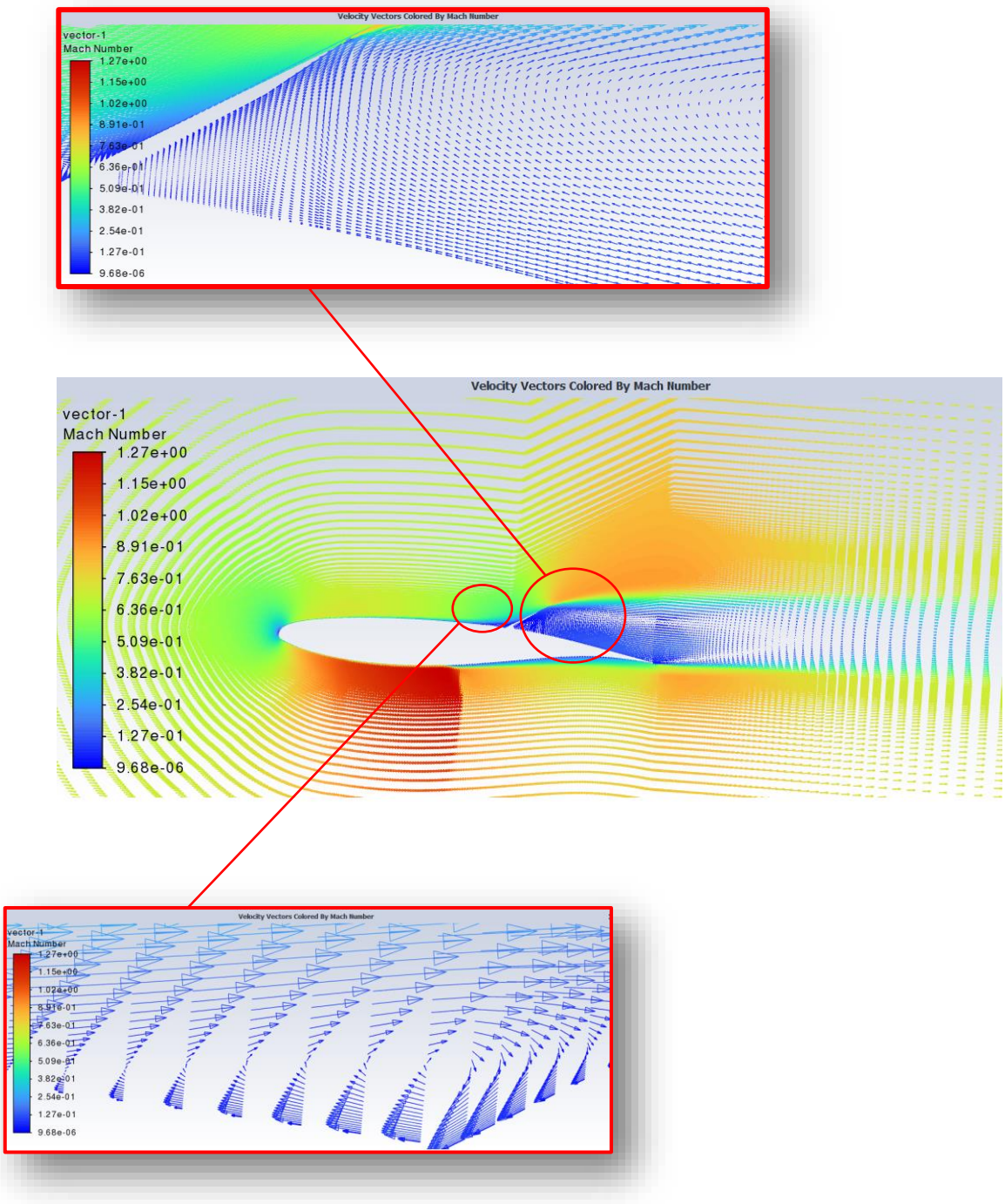

Figure IV-32 Velocity Vectors over OAT15A Airfoil with Spoiler at $\delta_{Sp} = 30°$**,** $Mach = 0.73$**,** $\propto = 1.5$**, *and*** $R_e = 3.5 \times 10^6$**.**

IV.7 Aspect Ratio Impact on Three different Wings

A wing is simply an airfoil extrusion, and comprehending how lift and drag forces are generated in a wing is essential. These simulations investigates three-dimensional flow fields around three different wings, and the pressure coefficient distribution along the wing surface at defined sections, are illustrated in the figures below as well as the pressure and mach number contours.

IV.7.1. Wing of NACA0012 airfoil

The 3D wing studied has a NACA0012 profile and is equipped with an aileron at a deflection angle of zero under the parameters M=0.75 and AOA=5, the results of pressure coefficient distribution at those conditions are presented in Figure **Figure 33** and **Figure 32**

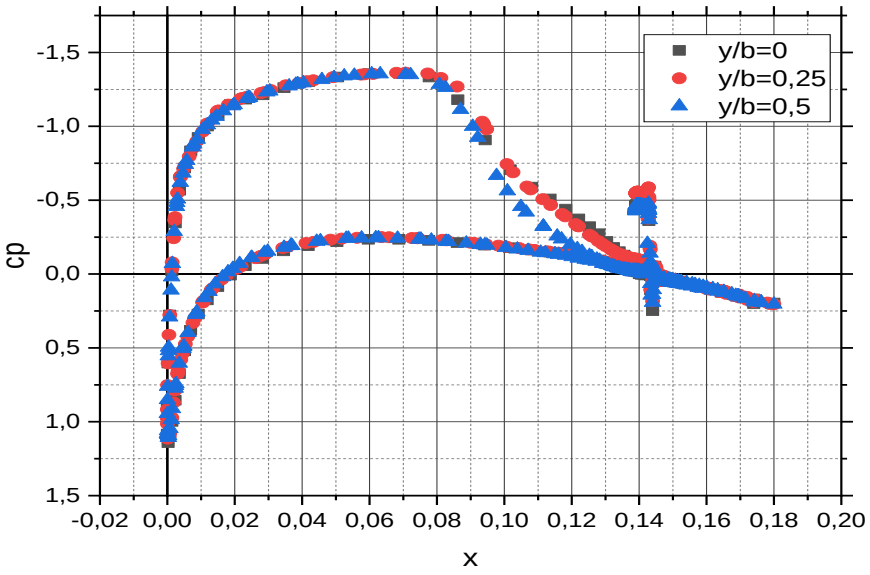

Figure IV-33 Pressure Coefficient Distribution over the Wing of NACA0012 airfoil with aileron at 0%, 25%, and 50% of wing span using the Spalart-Almaras turbulence model at $\delta_A =$ 0°, *M=0.75, and AOA=5°.*

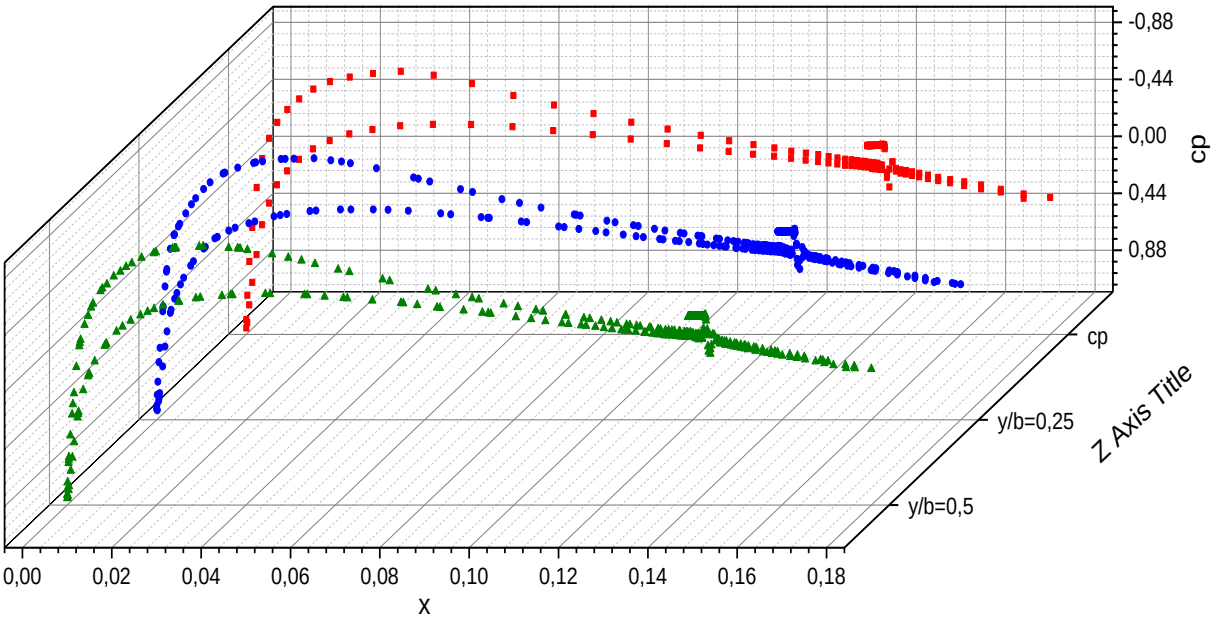

Figure IV-34 3D Illustration of Pressure Coefficient Distribution over the Wing of NACA0012 airfoil equipped with aileron of 0° deflection angle at 0%, 25%, and 50% of wing span using the Spalart-Almaras turbulence model at M=0.75 and AOA=5°.

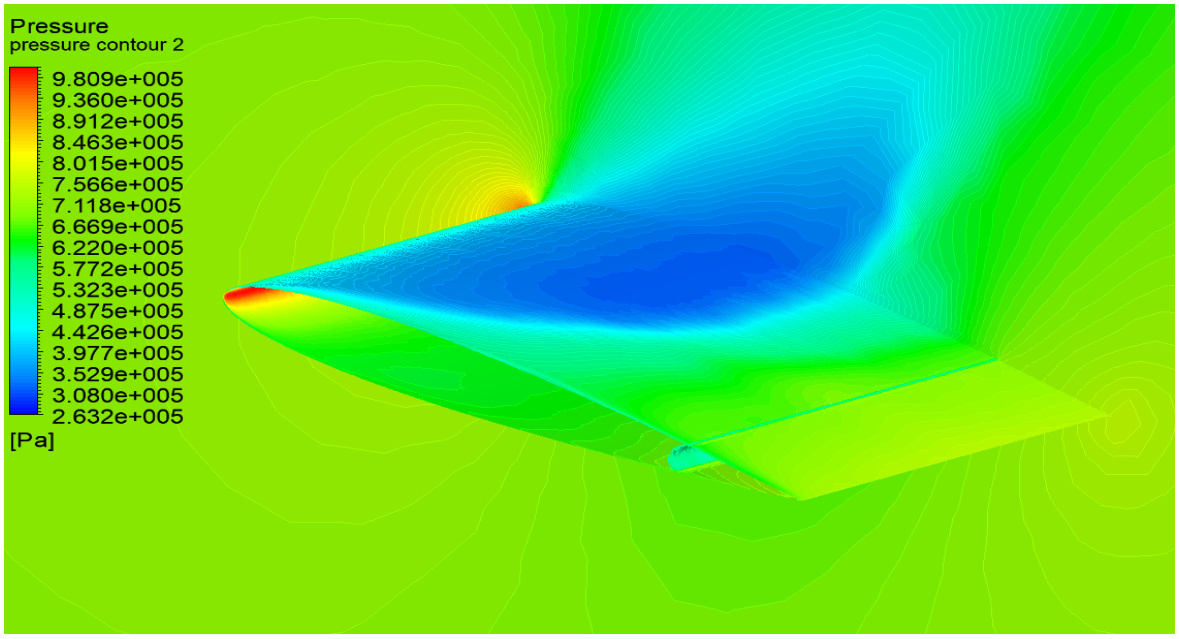

Figure IV-35 Pressure Contour over the Wing of NACA0012 airfoil with aileron using the Spalart-Almaras turbulence model at $\delta_A = 0°$, ***M=0.75, and AOA=5°.***

In addition, the results of surface pressure coefficient distribution and the contours of pressure and Mach number under conditions of a mach number M=0.73, AOA=1.5, and deflection angles of (-10,0) are also shown on the following figures.

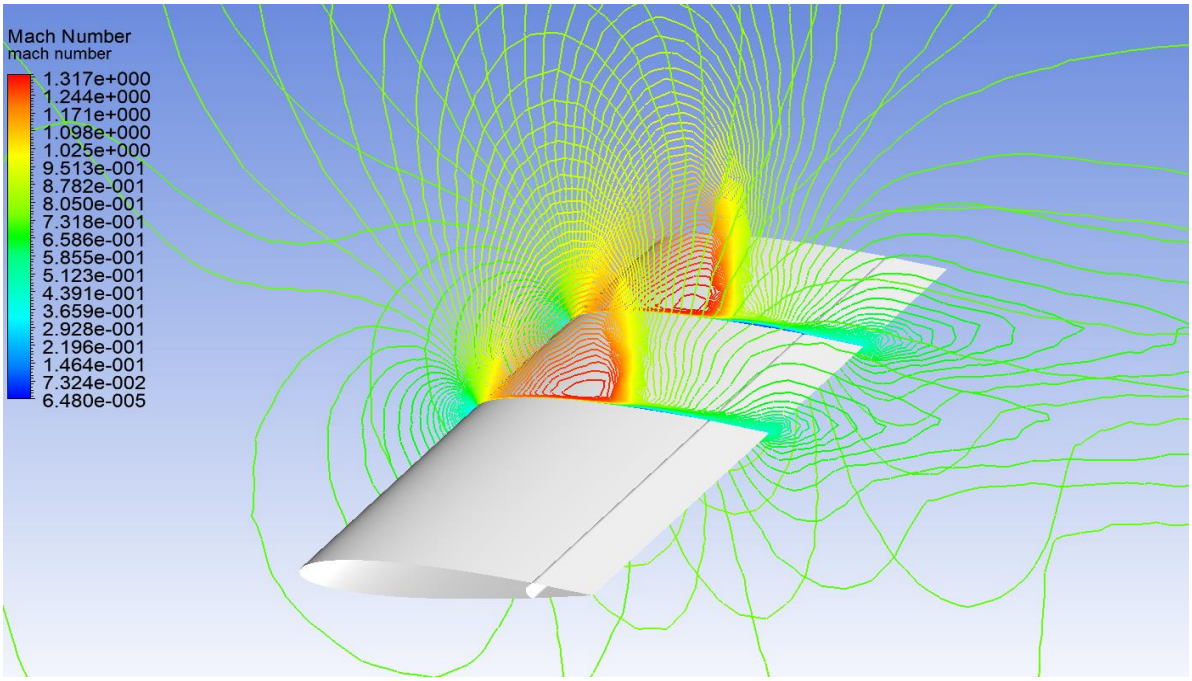

Figure IV-36 Mach Number Contour over the Wing of NACA0012 airfoil with aileron at 25% and 50% of wing span using the Spalart-Almaras turbulence model at $\delta_A = 0°$, ***M=0.75, and AOA=5°.***

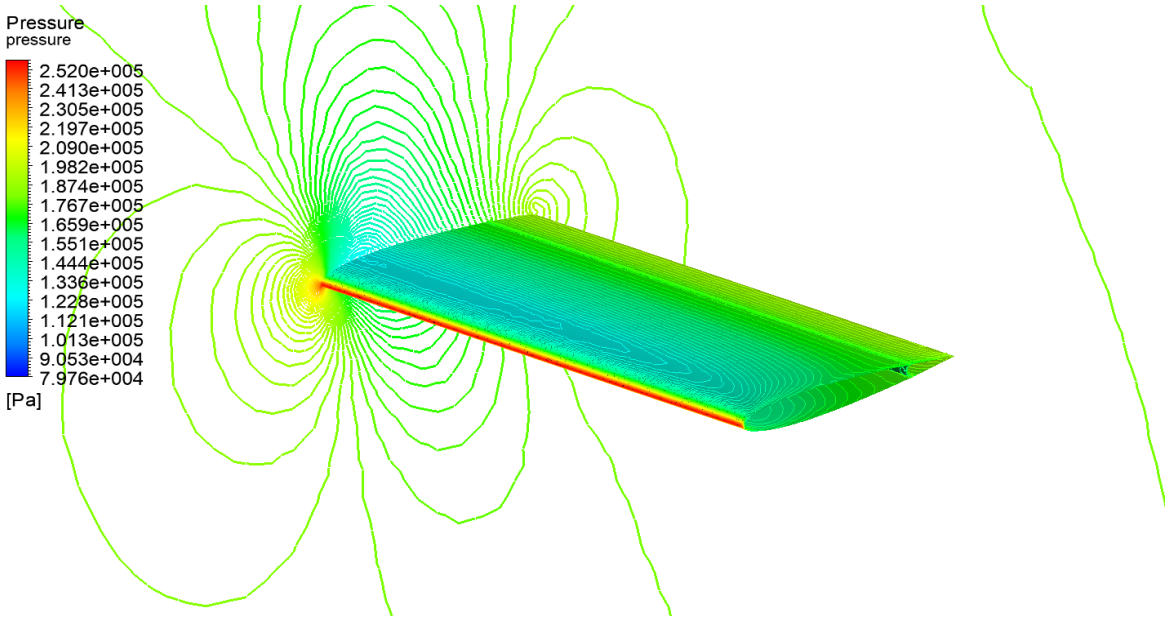

Figure IV-37 Pressure Contour over the Wing of NACA0012 airfoil with aileron using the Spalart-Almaras turbulence model at $\delta_A = 0°$, ***M=0.73, and AOA=1.5°.***

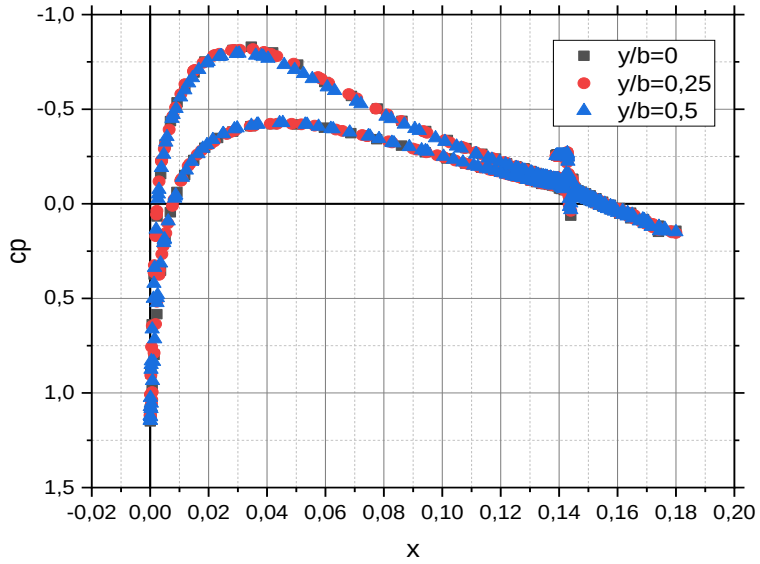

Figure IV-38 Pressure Coefficient Distribution over the Wing of NACA0012 airfoil with aileron at 0%, 25%, and 50% of wing span using the Spalart-Almaras turbulence model at $\delta_A = 0°$***, M=0.73, and AOA=1.5°.***

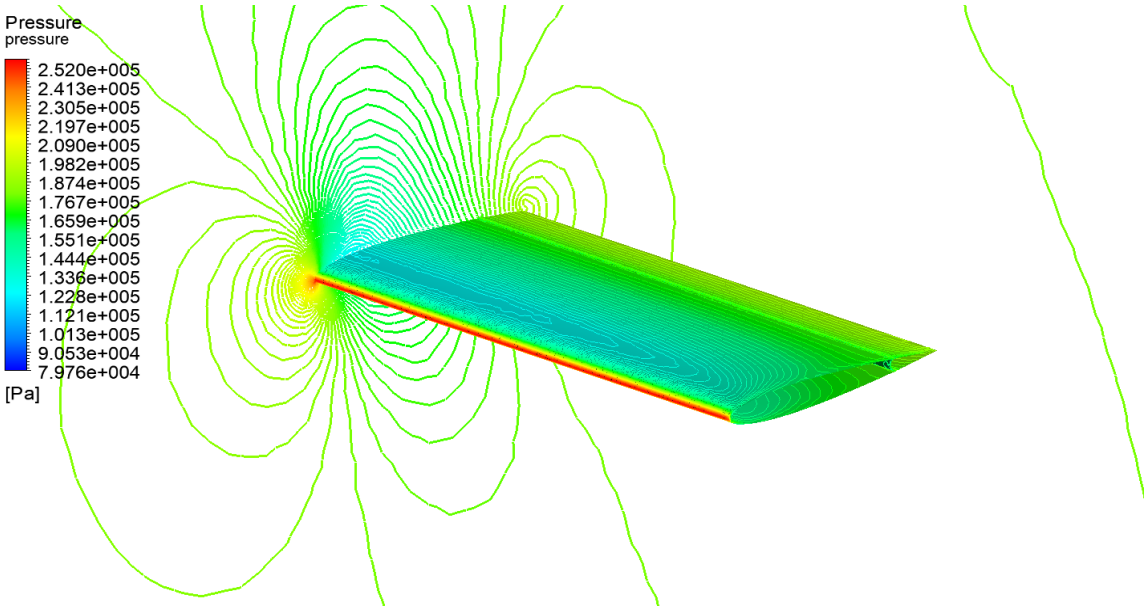

Pressure Contour Over the Wing of NACA0012 airfoil with aileron at 25% and 50% of wing span using the Spalart-Almaras turbulence model at $\delta_A = 0°$***, M=0.73, and AOA=1.5°.***

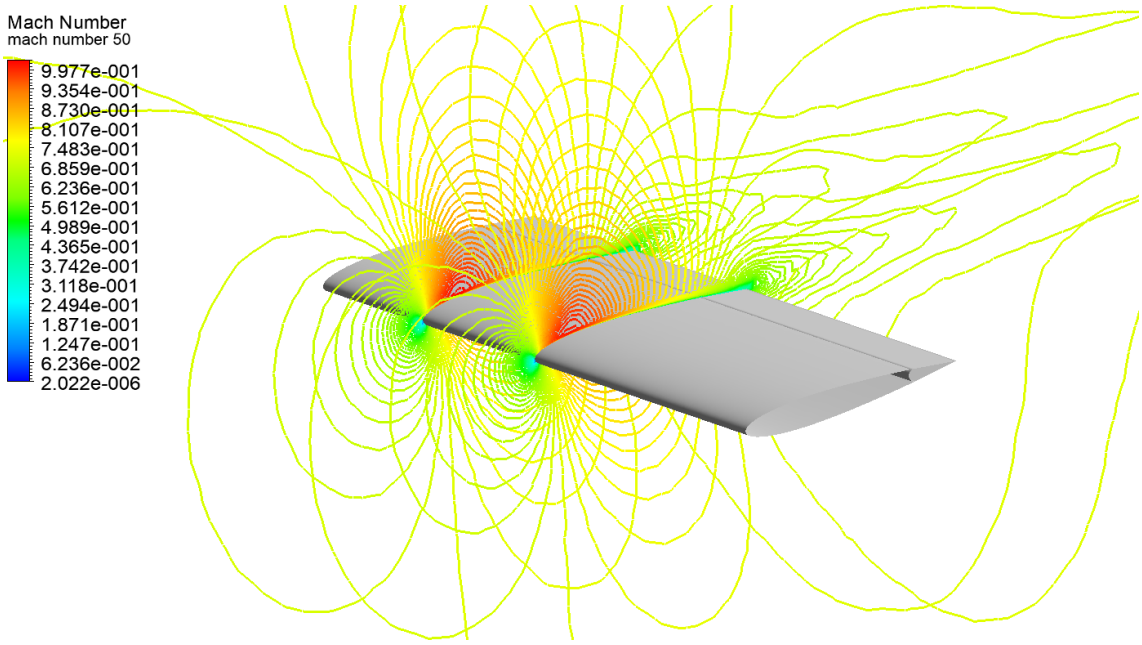

Figure IV-39 Mach Number Contour over the Wing of NACA0012 airfoil with aileron at 25% and 50% of wing span using the Spalart-Almaras turbulence model at $\delta_A = 0°$, ***M=0.73, and AOA=1.5°.***

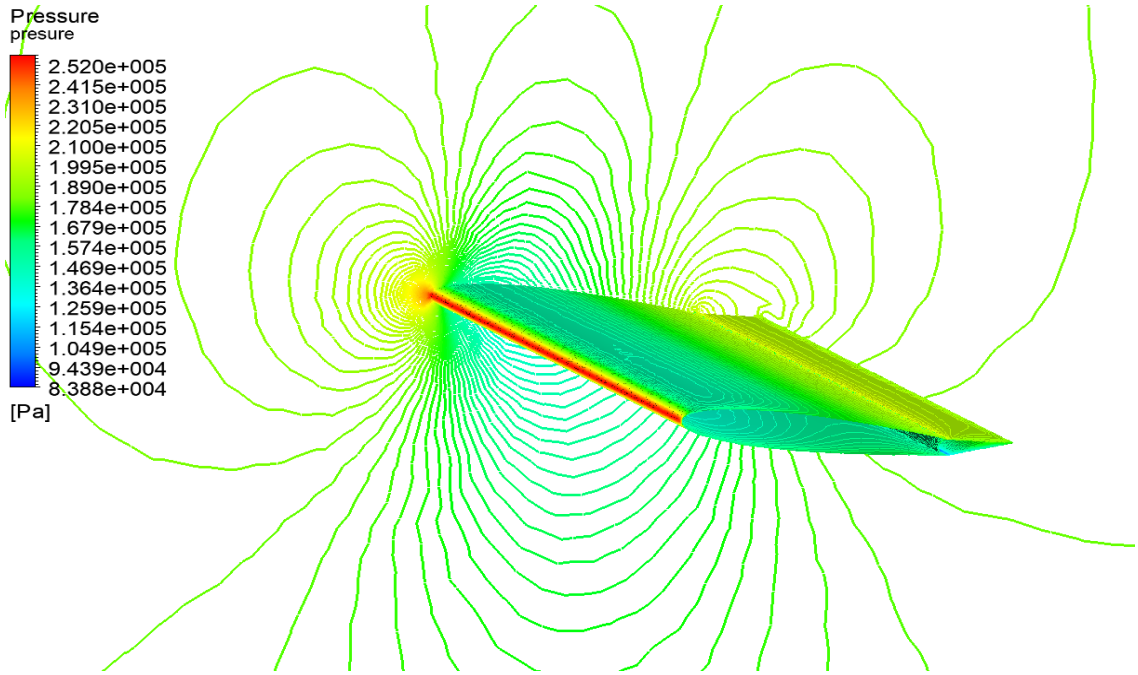

Figure IV-40 Pressure Contour Over the Wing of NACA0012 airfoil with aileron at 25% and 50% of wing span using the Spalart-Almaras turbulence model at $\delta_A = -10°$, ***M=0.73, and AOA=1.5°.***

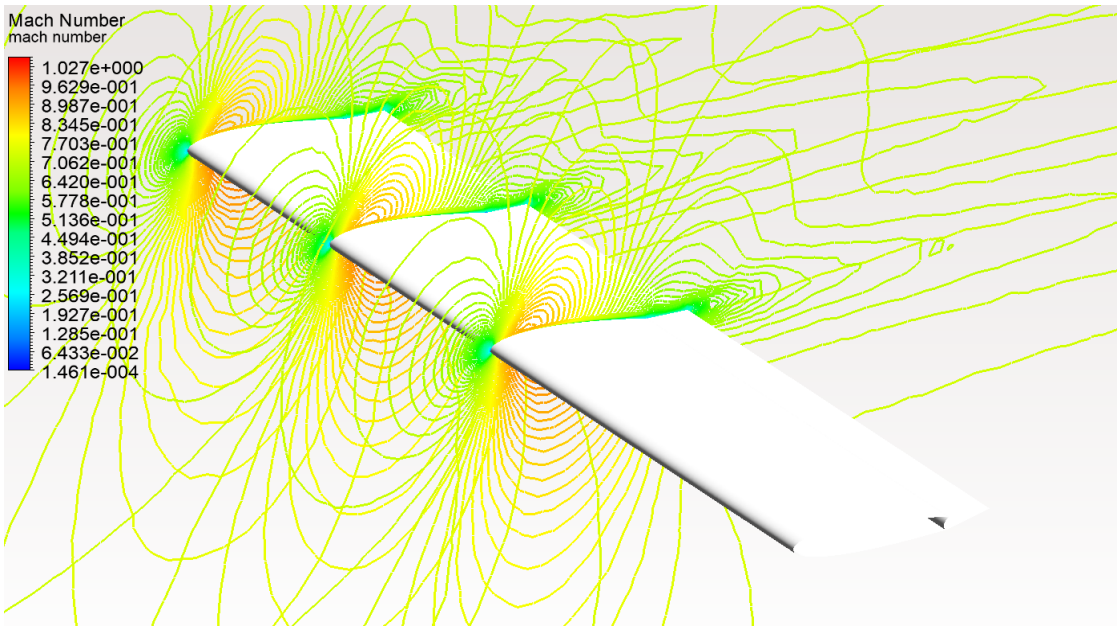

Figure IV-41 Mach number Contour Over the Wing of NACA0012 airfoil with aileron at 0%, 25%, and 50% of wing span using the Spalart-Almaras turbulence model at $\delta_A = -10°$, M=0.73, and AOA=1.5°.

The aerodynamic effect of the ailerons is presented for deflection angles. When making a comparison with the result of the baseline simulation with no deflection, the influence of the ailerons is apparent.

IV.7.2. Wing of OAT15A airfoil:

The results of surface pressure coefficient distribution and the contours of pressure and Mach number over the wing of OAT15A airfoil under conditions of a Mach number M=0.73, AOA=1.5, and deflection angles of 10° are shown in the following figures.

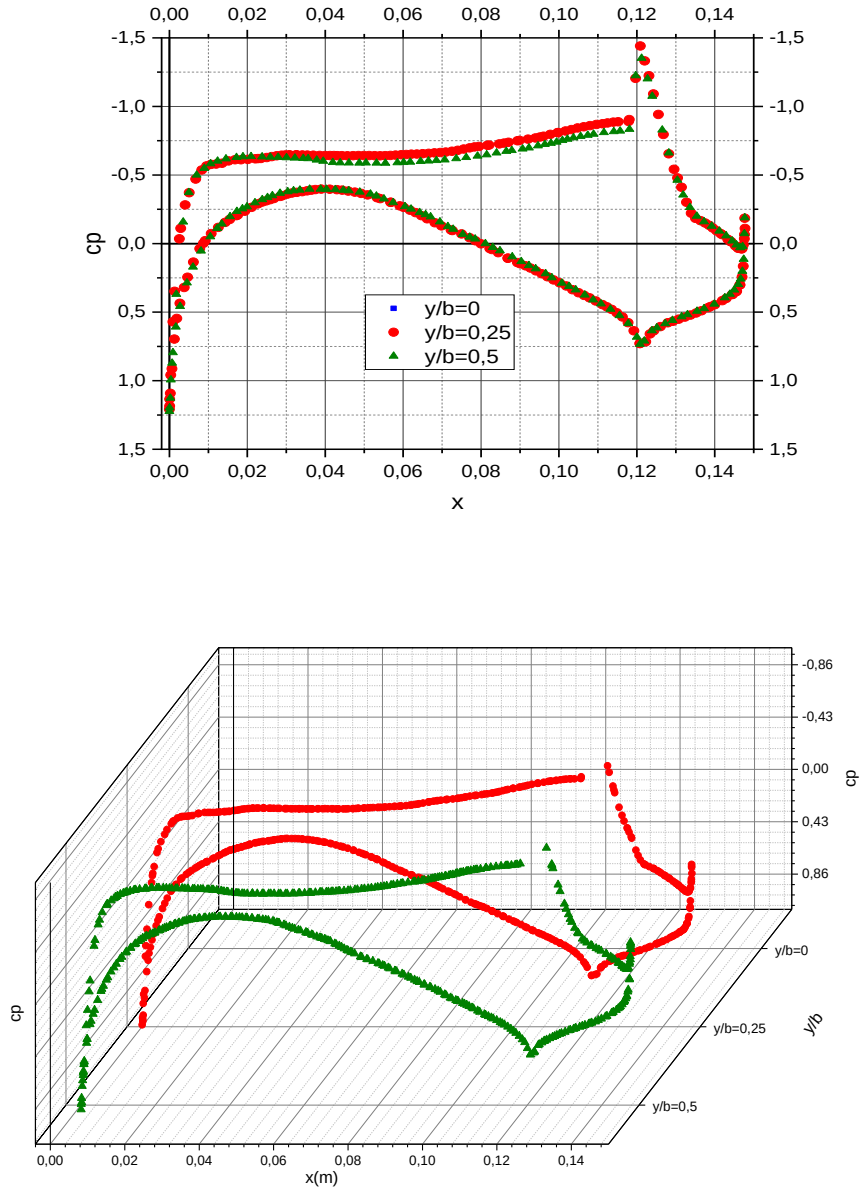

Figure IV-42 2D and 3D Illustration of Pressure Coefficient Distribution over the Wing of OAT15A airfoil equipped with aileron 10° of deflection angle at 2 sections of wing span using the Spalart-Almaras turbulence model at M=0.73 and AOA=1.5°.

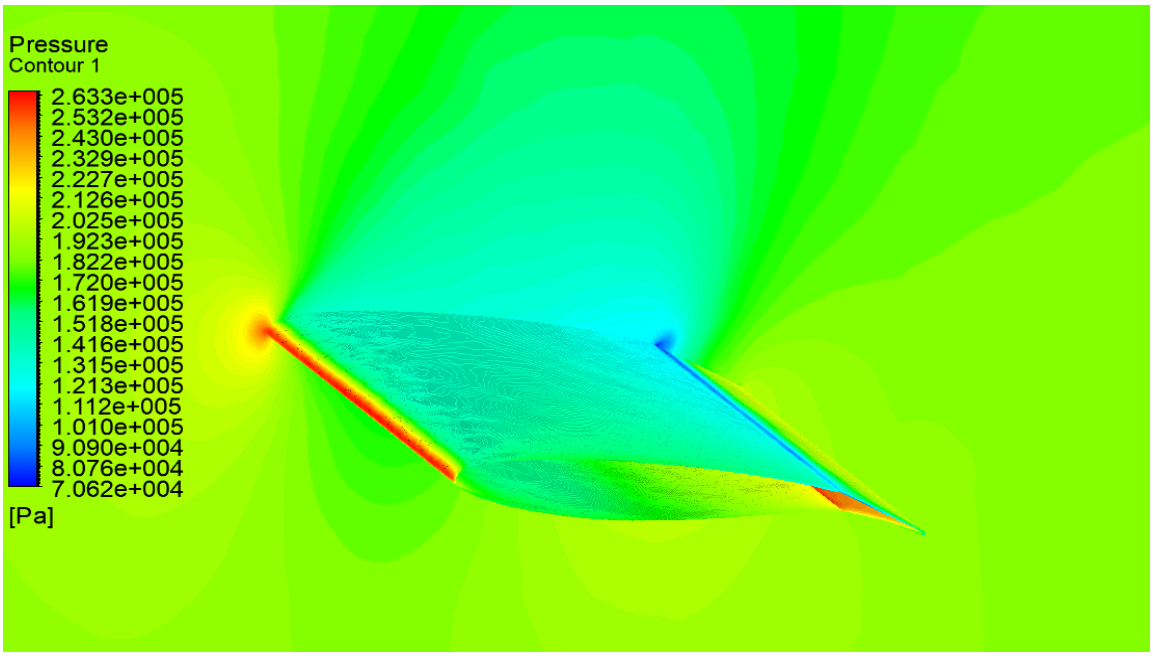

Figure IV-43 Pressure Contour Over the Wing of OAT15A airfoil with aileron at 2 sections of wing span using the Spalart-Almaras turbulence model at $\delta_A = 10°$***, M=0.73, and AOA=1.5°*** .

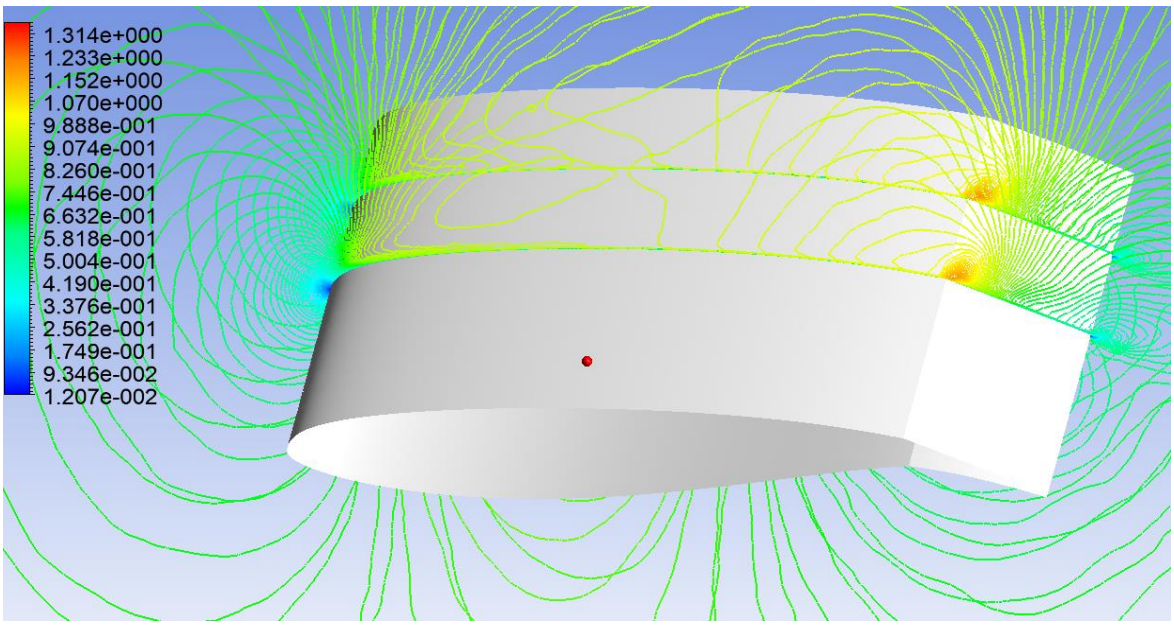

Figure IV-44 Mach number Contour Over the Wing of OAT15A airfoil with aileron at 2 sections of wing span using the Spalart-Almaras turbulence model at $\delta_A = 10°$***, M=0.73, and AOA=1.5°***

IV.7.3. ONERA M6 Wing:

The primary objective of the following was to illustrate the pressure distribution on the upper and lower surface at determined sections of wingspan, as shown in Figure below. A violent shock was observed near the fixed end of the leading edge, and this obtained shock weakens near the trailing edge of the wing.

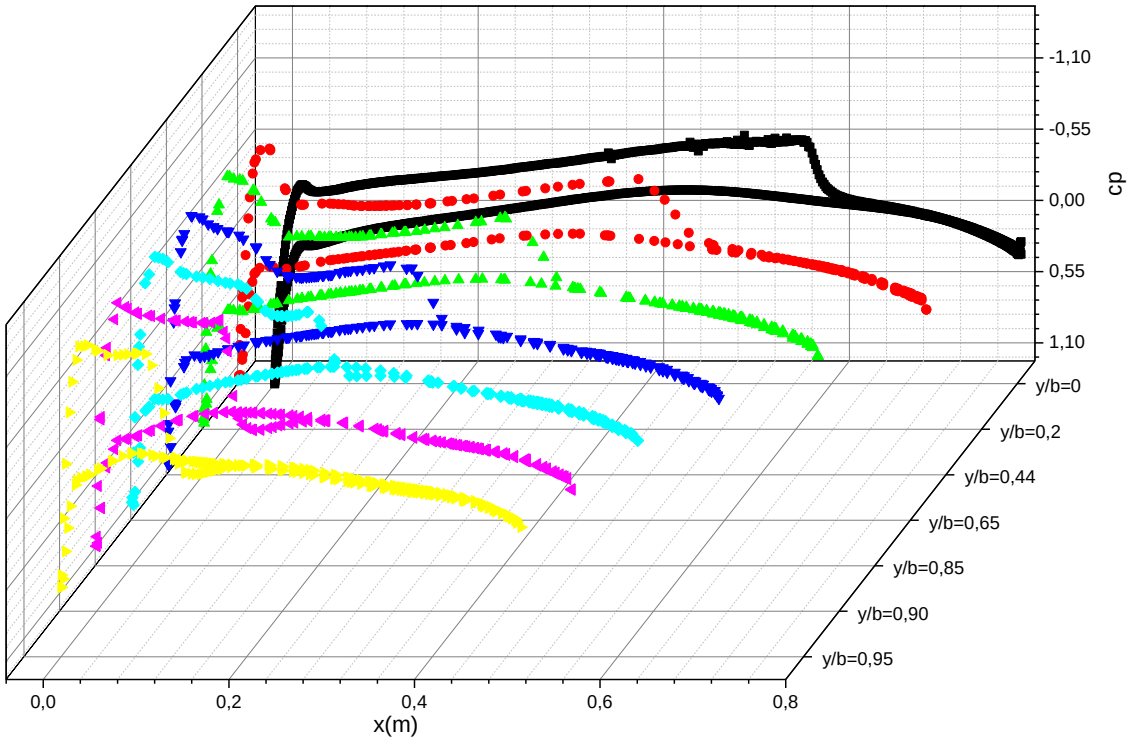

Figure IV-45 Pressure Coefficient Distribution over Onera M6 Wing at 6 sections using the Spalart-allmaras turbulence model.

IV.8 Conclusion:

The results of numerical simulations were presented for a flow around airfoils and wings in the transonic regime using a finite volume calculation code with a comparative study between the computed and experimental results, of both a conventional and supercritical profile with and without control surface, and the impact of the angle of attack and aspect ratio on different wing configurations. Furthermore, the flow description over an OAT15A airfoil connected to a Spoiler at an angle of deflection of 30 deg was also investigated. The numerical results are compatible with those of experimental measurements, this confirms the validity of using CFD as a reliable alternative to experimental procedures and the accuracy of the rest of the simulations.

Conclusion

Conclusion

The aeronautics industry has been known as a very special field in which advanced technologies are developed. Manufacturers now have a variety of numerical simulation techniques available in the form of calculation codes. However, understanding how these methods are developed is essential in order to avoid blindly applying the calculation codes and making serious interpreting errors.

The focus of this research was to analyze and comprehend "The Impact of Control Surface on Transonic Flow Mechanism and Aerodynamic Performances." As a first step toward establishing a strong bibliographic foundation for my work, I provided a literature review of previous studies (experimental and numerical) on the subject of movable control surface efficiency, as well as a general overview of the physics and behavior of transonic flows around aerodynamic profiles. The functionality and application of aircraft ailerons and spoilers, including the major physical phenomena involved in obtaining the aerodynamic performance of two types of airfoils (the NACA0012 conventional airfoil and OAT15A, RAE2822 supercritical airfoils) with and without those control surfaces, whether in two or three dimensions, have both been discussed.

To govern this type of flow, turbulence models (Spallart Almaras, K epsilon, and K Omega SST) are used, as well as a set of equations and mathematical modeling, specifically the Averaged-Navier stocks equations based on the Reynolds decomposition (RANS). These equations are supplemented by the case's initial conditions of the topic under study. This contribution was made with the ANSYS 2021 R2 software, and the simulations were focused on the evaluation of the steady-state for compressible flows around the aerodynamic profiles addressed in the previous paragraph. Furthermore, the ONERA M6 Swept wing, as well as the wings with NACA0012 and OAT15A as base profiles, are relatively complex research cases due to the presence of shock waves that interact with the boundary layer.

The edition of CFD Code Ansys 2021 R2 chosen was a compromise between calculation time and precision and has an ability to adapt to complex geometries, such as those with control surfaces, that necessitate a powerful

calculating system, and also to facilitate the application of boundary conditions. The numerical results agree with the experimental measurements, this validates the use of CFD as a reliable alternative to experimental procedures, as well as the accuracy of the rest simulations. The present project concentrated on comparative research and observing the contours of Mach number and pressure of the aerodynamic characteristics: the lift coefficient (C_l) and the drag coefficient (C_d) for the above-noted configurations. And based on the results, we can conclude the following:

- The results are highly dependent on the freestream Mach number, pressure, temperature, and applied Reynolds number.
- The critical Mach number depends on the angle of attack as well as the airfoil's geometry.
- The camber of the airfoil greatly intensifies the pressure gradient between the upper and lower surfaces, whereas the Mach number has little effect on this distribution.
- The Pressure and velocity Contours are found to be appropriate for corresponding Mach inputs and angles of attack.
- The numerical results, as well as Harris's experiment [96], indicate that the drag coefficient is not particularly sensitive to Mach variations in low transonic regimes. The transonic flow becomes very intense as the Mach number increases, and the drag coefficient rapidly increases.
- From the results discussed in chapter four, it can be concluded that the numerical results of the OAT15A supercritical airfoil having aileron on different angles of deflection show that beyond a certain deflection angle, detachments will appear on the upper surface ($\boldsymbol{\delta_A > 0}$) or on the lower surface ($\delta_A < 0$) and the return of the shock wave by increasing the aileron deflection.
- The Lift Coefficient is increasing with the increase of angle of attack and decreases with the increase in Mach speed due to a rise in drag coefficient in the transonic region and this is accurate with airfoil theory.
- The graphs of "Angle Of Attack Effect On OAT15A airfoil with Aileron at different deflection angles" show that as the angle of attack increases, so does the lift coefficient. However, increasing the angle of attack has a

limitation in that the airfoil appears to stall at angles of attack greater than those that provide the most lift.

- The lift, drag, and surface pressure characteristics observed for a steady flow field around OAT15A with the spoiler at 30 degrees of deflection angle agree with previous research. Lift is reduced while drag is increased, demonstrating the common nature of spoilers. A spoiler, also known as a lift dumper, is a device designed to reduce lift in an aircraft by forming a significant recirculation zone by connecting its trailing edge to that of the profile.
- Despite the complexity of the geometries' 3D configuration, the Spallart Almaras model provides good accuracy of results when compared to experiments such as capturing the violent shock near the fixed end of the leading edge of the ONERA M6 Wing, and this resulted in shock weakening near the trailing edge.

Recommendations for Future Studies:

The current study was exploratory in nature, and more research is needed to develop a complete understanding of the aerodynamic features of the Flight Control Surface. As a result, running a methodical series of tests and simulations on one configuration of a chosen control surface at various Reynolds numbers, for different angles of deflection at the same time at different angles of attack, and attempting to reach the limitations for several other types of airfoils would be extremely informative.


APPENDEXES

THEORETICAL BACKGROUND

❖ How do wings work?

Aircraft wings are designed to move air faster over the top of the wing. The cross-sectional shape obtained by the intersection of the wing with the perpendicular plane is called an airfoil **[91].**

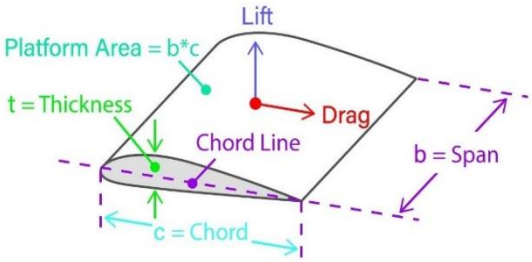

FIGURE A.1. Wing geometry definitions [92].

The pressure of the air decreases as it goes faster, as a result, the pressure on the top of the wing is less than the pressure on the bottom.

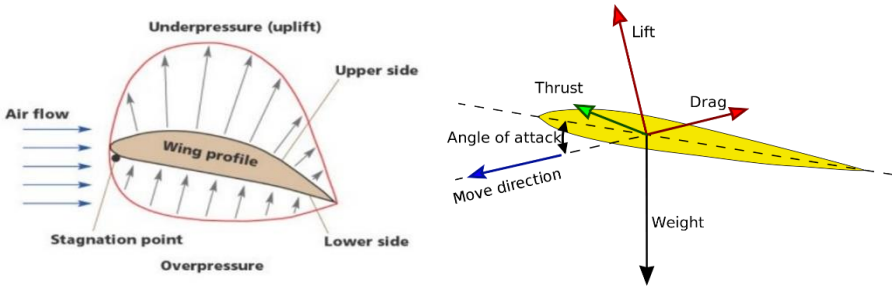

Figure A.2. Aerodynamic forces and Pressure distribution around wing profile [93].

An aerodynamic force is created by the pressure and shear stress distributions over the wing surface. This resultant aerodynamic force can be resolved into two forces, parallel and perpendicular to the relative wind. The direction of free stream velocity is defined as the relative wind. The two forces are known as lift and drag. Drag is always defined as the component of the aerodynamic force that is perpendicular to the relative wind. The component of the aerodynamic force perpendicular to the relative wind is defined as lift.

❖ **2D Profiles:**

- **Chord:** the distance from the leading edge to the trailing edge.
- **Thickness:** is the distance between the upper surface and the lower surface.
- **Mean chord:** is the curve equal distance from the upper surface to the lower surface.

❖ **3D Wing:** The plane shape and aerodynamic profile of the wing are fundamental geometry properties. The plan shape of aircraft wings can be classified as rectangular, elliptical, swept, triangular (or delta).

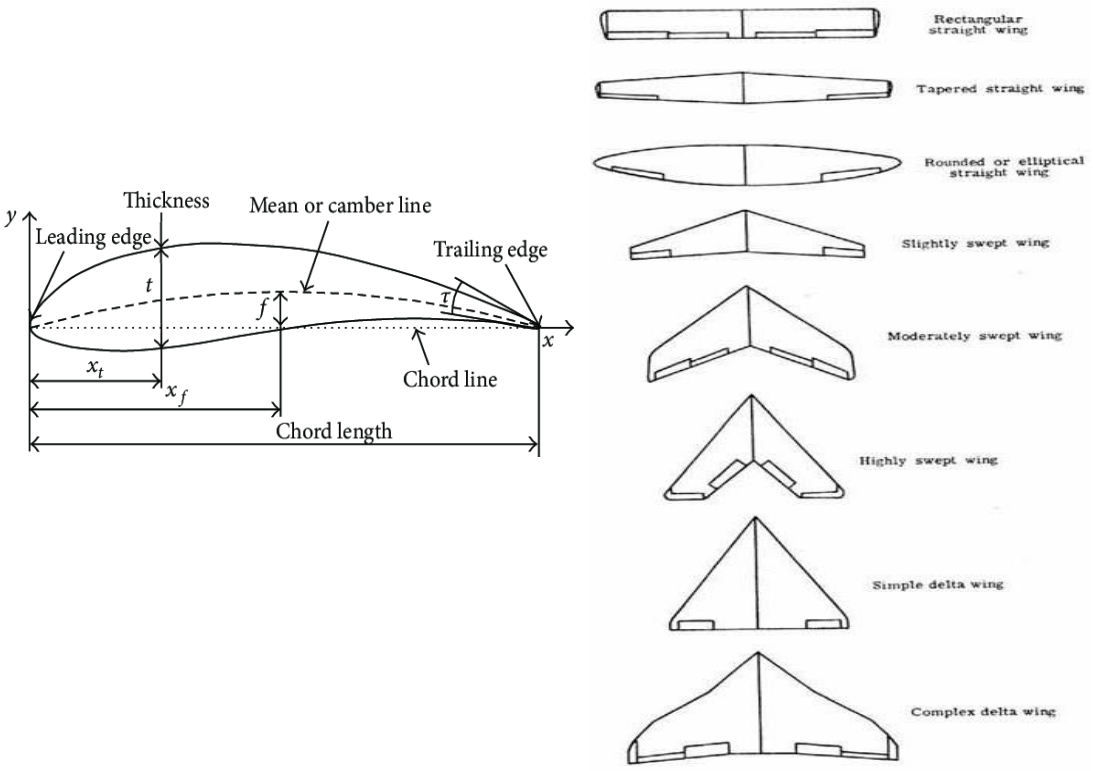

Figure A.3. Wing shapes [94], [95]

A. Features of NACA airfoils:

The **NACA profiles** are aerodynamic forms developed by the National Advisory for Aeronautics (USA), this organization has studied different families of profiles for various applications (aircraft, axial machines, wind turbines...). Among these families, we can distinguish profiles of four-digit, five-digit, six-digit and laminar profiles.

1. **Laminar Profiles:**

In order to minimize the friction drag, NACA has also explored a variety of profiles to maintain a laminar boundary layer across a substantial section of its chord. The lack of peak depression and over speed decreases the appearance of supersonic speeds (critical Mach) in this ideal range, but beyond the critical Mach, the shock is highly strong. NACA has designated them by a significant number of digits.

- The first digit represents the designation of the series of laminar profiles.
- The second represents the position of the minimum pressure.
- The index is the limit above and below the lift coefficient.
- The fourth represents the characteristic lift coefficient.
- The last two represent the maximum relative thickness.

2. **NACA 4-digit series:**

- The magnitude of maximum camber as the percentage of chord length.
- The second indicates the position of this camber as a percentage of the chord.
- The last two digits represent the maximum relative thickness, as a percentage of the chord.

3. **NACA 5 digits series:**

- The first digit defines the camber and when multiplied by 3/2, puts in the design lift coefficient ($\boldsymbol{C_l}$) in tenths.
- The next two digits, when divided by 2, give the position of the maximum camber in tenths of the chord.

The final two digits again indicate the maximum thickness (t) in the percentage of the chord.

4. **NACA 6 digits series:**

- The first digit denotes laminar profiles.
- The second digit indicates the position of the minimum pressure.
- The third digit indicates the maximum lift coefficient that can be reached under conditions of a desired pressure gradient ($\boldsymbol{C_l}$).
- The fourth digit indicates the lift coefficient for a flow at an angle of incidence $\boldsymbol{\alpha = 0°}$.

B. Features of supercritical airfoils :

Engineers thought of developing an aerofoil, which can increase the critical Mach number so that the formation of shockwaves can be delayed without loss in lift and increase in drag.

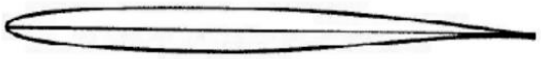

Figure A.4. Typical supercritical airfoil sketch [96].

They increased the thickness of the leading edge and made the upper surface flat so that there is no formation of the strong shockwave, and curved trailing edge lower surface which increases the pressure at the lower surface and account's for lift **[97]**.

1. Trailing edge thickness:

The design philosophy of the supercritical aerofoil required that the trailing-edge slopes of the upper and lower surfaces be equal. This requirement served to retard flow separation by reducing the pressure recovery gradient on the upper surface so that the pressure coefficients recovered to only slightly positive values at the trailing edge. Increasing the trailing-edge thickness of an interim 11-percent-thick supercritical aerofoil from 0 to 1.0 percent of the chord resulted in a significant decrease in wave drag at transonic Mach numbers **[98].**

2. Maximum thickness:

For the thinner aerofoil, the onset of trailing-edge separation began at an approximately 0.1 higher normal-force coefficient at the higher test Mach numbers, and drag divergence Mach number at a normal-force coefficient of 0.7 was 0.01 higher **[98].**

3. **Aft upper surface curvature**:

The rear upper surface of the supercritical aerofoil is shaped to accelerate the flow following the shock wave in order to produce a near-sonic plateau at design conditions **[99].**

❖ The aerodynamic forces:

1. **Lift:** To overcome the weight force, airplanes generate an opposing force called lift. The magnitude of the coefficient depends on the shape of the body and its angle of attack **[100]**. Now, **Lift force:** $\boldsymbol{L = \frac{1}{2}\rho S V^2 C_L}$
   - **L** is the lift force,
   - $\boldsymbol{\rho}$is air density,
   - $\boldsymbol{V}$ is the velocity of air,
   - $\boldsymbol{S}$ is planform area,
   - $\boldsymbol{C_L}$ is the lift coefficient.

   a. Lift coefficient: $\boldsymbol{C_L}$ depends on the shape of the profile, surface condition, angle of attack, and freestream speed.

2. **Drag:** As the airplane moves through the air, there is another aerodynamic force present. The air resists the motion of the aircraft and the resistance force is called drag **[101]**. **Drag force**: $\boldsymbol{D = \frac{1}{2}\rho S V^2 C_d}$
   - **D** is the lift force
   - $\boldsymbol{\rho}$is air density
   - $\boldsymbol{V}$ is the velocity of air
   - $\boldsymbol{S}$ is planform area
   - $\boldsymbol{C_d}$ is the drag coefficient

   b. Drag coefficient: $\boldsymbol{C_d}$ is a unit less number, which indicates a body's ability to generate fluid resistance and also depends on the shape of the profile, surface condition, angle of attack and, freestream speed.

   c. Pressure coefficient: $\boldsymbol{C_P}$ The pressure is non-dimensional thanks to the following formula **[102]**: $\boldsymbol{C_P = \frac{P - P_{ref}}{\frac{1}{2}\rho V_{ref}^2}}$

The reference pressure chosen in practice is often the upstream static pressure, and the reference speed chosen is that of the beyond boundary layer flow.

The center of pressure is the point at which the resulting aerodynamic forces are applied, and it moves according to the incidence. For common angles of incidence, the center is often positioned on the profile chord between $\boldsymbol{30\%}$ and $\boldsymbol{50\%}$ of the front half of the profile and is determined by this formula **[102]**: $\boldsymbol{\frac{x_p}{l} = 0,25 - \frac{C_m}{C_L}}$

❖ Airfoil Data:

There are three airfoils chosen for this analysis, two Supercritical airfoils which are **OAT15A** and **RAE2822** and the third is **NACA 0012** that is a conventional airfoil. In this APPENDIX, their specification (Cordinates) are shown. In addition, those airfoils are also attached to a certain control surface.

The profile drawings of **NACA0012** and **RAE2822** given here have been taken directly from "nasa airfoil generator". **OAT15A** airfoil's cordinate has been taken from **[103]**. The Main with Aileron Cordinates are shown in APPENDIX C.

A. OAT15A Airfoil Cordinates:

Table 19.OAT15A Airfoil Cordinates.

#	x	Y	#	x	Y	#	x	Y	#	x	Y	#	x	Y
1	1.5000e-01	-3.7450e-04	31	1.09183e-01	-1.0264e-03	61	5.42011e-02	-8.2622e-03	91	1.929820e-02	-6.9753e-03	121	4.4145e-03	-3.4259e-03
2	1.495823e-01	-3.2670e-04	32	1.072254e-01	-1.3149e-03	62	5.2659e-02	-8.3428e-03	92	1.852380e-02	-6.8587e-03	122	4.1563e-03	-3.3229e-03
3	1.492485e-01	-2.8930e-04	33	1.052626e-01	-1.6136e-03	63	5.11423e-02	-8.4110e-03	93	1.777190e-02	-6.7407e-03	123	3.9091e-03	-3.2219e-03
4	1.488110e-01	-2.4140e-04	34	1.032969e-01	-1.9200e-03	64	4.96513e-02	-8.4672e-03	94	1.704220e-02	-6.6216e-03	124	3.6725e-03	-3.1226e-03
5	1.482651e-01	-1.8330e-04	35	1.013301e-01	-2.2317e-03	65	4.81862e-02	-8.5117e-03	95	1.633440e-02	-6.5015e-03	125	3.4462e-03	-3.0252e-03
6	1.476113e-01	-1.1610e-04	36	9.936390e-02	-2.5466e-03	66	4.67473e-02	-8.5449e-03	96	1.564800e-02	-6.3807e-03	126	3.2298e-03	-2.9295e-03
7	1.468538e-01	-4.1400e-05	37	9.740010e-02	-2.8630e-03	67	4.53348e-02	-8.5673e-03	97	1.498290e-02	-6.2592e-03	127	3.0229e-03	-2.8355e-03
8	1.459973e-01	3.9400e-05	38	9.544020e-02	-3.1792e-03	68	4.39487e-02	-8.5793e-03	98	1.433850e-02	-6.1373e-03	128	2.8252e-03	-2.7430e-03
9	1.450466e-01	1.2440e-04	39	9.348570e-02	-3.4937e-03	69	4.25893e-02	-8.5814e-03	99	1.371470e-02	-6.0149e-03	129	2.6363e-03	-2.6520e-03
10	1.440066e-01	2.1200e-04	40	9.153830e-02	-3.8052e-03	70	4.12565e-02	-8.5740e-03	100	1.311090e-02	-5.8923e-03	130	2.4558e-03	-2.5623e-03
11	1.428819e-01	3.0030e-04	41	8.959920e-02	-4.1124e-03	71	3.99504e-02	-8.5578e-03	101	1.252690e-02	-5.7696e-03	131	2.2834e-03	-2.4739e-03
12	1.416772e-01	3.8730e-04	42	8.766980e-02	-4.4143e-03	72	3.86711e-02	-8.5330e-03	102	1.196230e-02	-5.6467e-03	132	2.1188e-03	-2.3867e-03
13	1.403970e-01	4.7120e-04	43	8.575130e-02	-4.7098e-03	73	3.74185e-02	-8.5002e-03	103	1.141670e-02	-5.5237e-03	133	1.9615e-03	-2.3004e-03
14	1.390458e-01	5.4970e-04	44	8.384500e-02	-4.9981e-03	74	3.61926e-02	-8.4600e-03	104	1.088980e-02	-5.4009e-03	134	1.8114e-03	-2.2149e-03
15	1.376280e-01	6.2050e-04	45	8.195200e-02	-5.2782e-03	75	3.49933e-02	-8.4126e-03	105	1.038120e-02	-5.2781e-03	135	1.6680e-03	-2.1302e-03
16	1.361479e-01	6.8110e-04	46	8.007340e-02	-5.5495e-03	76	3.38205e-02	-8.3586e-03	106	9.890600e-03	-5.1556e-03	136	1.5312e-03	-2.0460e-03
17	1.346096e-01	7.2890e-04	47	7.821020e-02	-5.8113e-03	77	3.26742e-02	-8.2982e-03	107	9.417600e-03	-5.0333e-03	137	1.4005e-03	-1.9621e-03
18	1.330175e-01	7.6080e-04	48	7.636340e-02	-6.0631e-03	78	3.15542e-02	-8.2320e-03	108	8.961700e-03	-4.9115e-03	138	1.2758e-03	-1.8783e-03
19	1.313756e-01	7.7420e-04	49	7.453400e-02	-6.3042e-03	79	3.04604e-02	-8.1602e-03	109	8.522700e-03	-4.7903e-03	139	1.1567e-03	-1.7945e-03
20	1.296879e-01	7.6620e-04	50	7.272270e-02	-6.5344e-03	80	2.93925e-02	-8.0832e-03	110	8.100000e-03	-4.6697e-03	140	1.0431e-03	-1.7104e-03
21	1.279586e-01	7.3420e-04	51	7.093050e-02	-6.7532e-03	81	2.83504e-02	-8.0012e-03	111	7.693300e-03	-4.5499e-03	141	9.3470e-04	-1.6257e-03
22	1.261917e-01	6.7620e-04	52	6.915810e-02	-6.9603e-03	82	2.7334e-02	-7.9145e-03	112	7.302200e-03	-4.4310e-03	142	8.3150e-04	-1.5402e-03
23	1.243910e-01	5.9060e-04	53	6.740620e-02	-7.1555e-03	83	2.63429e-02	-7.8236e-03	113	6.926300e-03	-4.3133e-03	143	7.3320e-04	-1.4536e-03
24	1.225602e-01	4.7680e-04	54	6.567550e-02	-7.3385e-03	84	2.5377e-02	-7.7285e-03	114	6.565100e-03	-4.1968e-03	144	6.3990e-04	-1.3655e-03
25	1.207031e-01	3.3470e-04	55	6.396660e-02	-7.5089e-03	85	2.4436e-02	-7.6298e-03	115	6.218200e-03	-4.0817e-03	145	5.5160e-04	-1.2756e-03
26	1.188231e-01	1.6500e-04	56	6.228010e-02	-7.6668e-03	86	2.35197e-02	-7.5275e-03	116	5.885300e-03	-3.9681e-03	146	4.6840e-04	-1.1836e-03
27	1.169233e-01	-3.0500e-05	57	6.061650e-02	-7.8118e-03	87	2.26278e-02	-7.4221e-03	117	5.565800e-03	-3.8561e-03	147	3.9040e-04	-1.0889e-03
28	1.150068e-01	-2.5010e-04	58	5.897640e-02	-7.9438e-03	88	2.1760e-02	-7.3139e-03	118	5.259400e-03	-3.7458e-03	148	3.1810e-04	-9.9140e-04
29	1.130763e-01	-4.9110e-04	59	5.736020e-02	-8.0629e-03	89	2.0916e-02	-7.2032e-03	119	4.965700e-03	-3.6373e-03	149	2.5180e-04	-8.9050e-04
30	1.111344e-01	-7.5090e-04	60	5.576820e-02	-8.1690e-03	90	2.00955e-02	-7.0902e-03	120	4.684200e-03	-3.5307e-03	150	1.9200e-04	-7.8610e-04

Table 20.OAT15A Airfoil Cordinates.

#	X	Y	#	x	Y	#	X	Y	#	X	Y	#	X	Y
151	1.394e-04	-6.7790e-04	181	2.5863e-03	3.6065e-03	211	1.81514e-02	7.6223e-03	241	5.43913e-02	1.0078e-02	271	1.1102e-01	7.2821e-03
152	9.45e-05	-5.6580e-04	182	2.8507e-03	3.7637e-03	212	1.89869e-02	7.7352e-03	242	5.60118e-02	1.01072e-02	272	1.129889e-01	6.9955e-03
153	5.8e-05	-4.4990e-04	183	3.1305e-03	3.9190e-03	213	1.9846e-02	7.8469e-03	243	5.7658e-02	1.01313e-02	273	1.149419e-01	6.6961e-03
154	3.03e-05	-3.3030e-04	184	3.4257e-03	4.0725e-03	214	2.07292e-02	7.9571e-03	244	5.93294e-02	1.01499e-02	274	1.168764e-01	6.3863e-03
155	1.16e-05	-2.0710e-04	185	3.7366e-03	4.2241e-03	215	2.16366e-02	8.0659e-03	245	6.10257e-02	1.01629e-02	275	1.187901e-01	6.0690e-03
156	1.70e-06	-8.0800e-05	186	4.0634e-03	4.3739e-03	216	2.25686e-02	8.1732e-03	246	6.27463e-02	1.01698e-02	276	1.206802e-01	5.7471e-03
157	0.00e+00	0.0000e+00	187	4.4062e-03	4.5217e-03	217	2.35254e-02	8.2790e-03	247	6.44907e-02	1.01705e-02	277	1.225442e-01	5.4233e-03
158	6.00e-07	4.8500e-05	188	4.7653e-03	4.6678e-03	218	2.45072e-02	8.3831e-03	248	6.62585e-02	1.01646e-02	278	1.243791e-01	5.1000e-03
159	7.90e-06	1.8060e-04	189	5.1409e-03	4.8120e-03	219	2.55143e-02	8.4855e-03	249	6.80489e-02	1.01519e-02	279	1.26182e-01	4.77890e-03
160	2.33e-05	3.15400e-04	190	5.5333e-03	4.9545e-03	220	2.6547e-02	8.5861e-03	250	6.98613e-02	1.01318e-02	280	1.279495e-01	4.4617e-03
161	4.65e-05	4.52800e-04	191	5.9427e-03	5.0954e-03	221	2.76055e-02	8.6847e-03	251	7.16950e-02	1.01042e-02	281	1.296783e-01	4.1496e-03
162	7.75e-05	5.9300e-04	192	6.3693e-03	5.2346e-03	222	2.8690e-02	8.7814e-03	252	7.35490e-02	1.00685e-02	282	1.313649e-01	3.8440e-03
163	1.16e-04	7.3580e-04	193	6.8135e-03	5.3722e-03	223	2.98007e-02	8.8760e-03	253	7.54227e-02	1.00244e-02	283	1.330057e-01	3.5457e-03
164	1.623e-04	8.8140e-04	194	7.2755e-03	5.5084e-03	224	3.09377e-02	8.9684e-03	254	7.73150e-02	9.97150e-03	284	1.345967e-01	3.2558e-03
165	2.167e-04	1.0299e-03	195	7.7556e-03	5.6430e-03	225	3.21012e-02	9.0585e-03	255	7.92248e-02	9.90940e-03	285	1.361342e-01	2.9752e-03
166	2.794e-04	1.1811e-03	196	8.2540e-03	5.7763e-03	226	3.32915e-02	9.1463e-03	256	8.11512e-02	9.83750e-03	286	1.376139e-01	2.7047e-03
167	3.51e-04	1.3350e-03	197	8.7712e-03	5.9082e-03	227	3.45086e-02	9.23140e-03	257	8.30930e-02	9.75550e-03	287	1.390317e-01	2.445e-03
168	4.319e-04	1.4914e-03	198	9.3074e-03	6.0387e-03	228	3.57527e-02	9.3139e-03	258	8.50488e-02	9.66290e-03	288	1.403834e-01	2.1967e-03
169	5.228e-04	1.6502e-03	199	9.8629e-03	6.1679e-03	229	3.70238e-02	9.3936e-03	259	8.70174e-02	9.55920e-03	289	1.416643e-01	1.9605e-03
170	6.242e-04	1.8110e-03	200	1.0438e-02	6.2959e-03	230	3.83221e-02	9.4704e-03	260	8.89973e-02	9.44400e-03	290	1.42870e-01	1.737e-03
171	7.368e-04	1.9736e-03	201	1.10331e-02	6.4227e-03	231	3.96475e-02	9.5441e-03	261	9.09871e-02	9.31680e-03	291	1.439959e-01	1.5269e-03
172	8.612e-04	2.1375e-03	202	1.16485e-02	6.5482e-03	232	4.10002e-02	9.6146e-03	262	9.29851e-02	9.17710e-03	292	1.450372e-01	1.3312e-03
173	9.98e-04	2.3022e-03	203	1.22844e-02	6.6726e-03	233	4.23801e-02	9.6817e-03	263	9.49896e-02	9.02440e-03	293	1.459891e-01	1.1509e-03
174	1.1476e-03	2.4675e-03	204	1.29412e-02	6.7957e-03	234	4.37872e-02	9.7452e-03	264	9.69988e-02	8.85830e-03	294	1.468469e-01	9.8710e-04
175	1.3105e-03	2.6327e-03	205	1.36193e-02	6.9176e-03	235	4.52215e-02	9.8052e-03	265	9.90107e-02	8.67840e-03	295	1.476057e-01	8.4120e-04
176	1.4872e-03	2.7977e-03	506	1.43189e-02	7.0383e-03	236	4.66829e-02	9.8612e-03	266	1.010235e-01	8.48410e-03	296	1.482606e-01	7.1440e-04
177	1.6779e-03	2.9619e-03	207	1.50404e-02	7.1576e-03	237	4.81712e-02	9.9133e-03	267	1.030349e-01	8.275e-03	297	1.488075e-01	6.0800e-04
178	1.883e-03	3.1251e-03	208	1.57841e-02	7.2757e-03	238	4.96865e-02	9.9612e-03	268	1.050426e-01	8.0505e-03	298	1.492459e-01	5.2250e-04
179	2.1026e-03	3.2871e-03	209	1.65503e-02	7.3926e-03	239	5.12283e-02	1.00047e-02	269	1.070444e-01	7.8103e-03	299	1.495804e-01	4.5710e-04
180	2.3370e-03	3.4476e-03	210	1.73393e-02	7.5081e-03	240	5.27967e-02	1.00437e-02	270	1.090377e-01	7.554e-03	300	1.50e-01	3.7500e-04

B. RAE2822 Airfoil Cordinates:

Table 21.RAE2822 Airfoil Cordinates.

#	x	Y	#	x	Y	#	x	Y	#	x	Y
1	1	0	33	0,5	0,062029	65	0	0	97	0,5	-0,050563
2	0,999398	0,000128	34	0,475466	0,06253	66	0,000602	-0,00316	98	0,524534	-0,047719
3	0,997592	0,00051	35	0,450991	0,062774	67	0,002408	-0,006308	99	0,549009	-0,044642
4	0,994588	0,001137	36	0,426635	0,062779	68	0,005412	-0,009443	100	0,573365	-0,041397
5	0,990393	0,002001	37	0,402455	0,062562	69	0,009607	-0,012559	101	0,597545	-0,038043
6	0,985016	0,003092	38	0,37851	0,062133	70	0,014984	-0,015649	102	0,62149	-0,034631
7	0,97847	0,004401	39	0,354858	0,061497	71	0,02153	-0,018707	103	0,645142	-0,031207
8	0,970772	0,005915	40	0,331555	0,06066	72	0,029228	-0,021722	104	0,668445	-0,027814
9	0,96194	0,007622	41	0,308658	0,059629	73	0,03806	-0,024685	105	0,691342	-0,024495
10	0,951995	0,009508	42	0,286222	0,058414	74	0,048005	-0,027586	106	0,713778	-0,021289
11	0,940961	0,011562	43	0,264302	0,057026	75	0,059039	-0,030416	107	0,735698	-0,018232
12	0,928864	0,013769	44	0,242949	0,05547	76	0,071136	-0,03317	108	0,757051	-0,015357
13	0,915735	0,016113	45	0,222215	0,053753	77	0,084265	-0,035843	109	0,777785	-0,01269
14	0,901604	0,01858	46	0,20215	0,051885	78	0,098396	-0,038431	110	0,79785	-0,010244
15	0,886505	0,021153	47	0,182803	0,049874	79	0,113495	-0,040929	111	0,817197	-0,008027
16	0,870476	0,023817	48	0,164221	0,047729	80	0,129524	-0,043326	112	0,835779	-0,006048
17	0,853553	0,026554	49	0,146447	0,045457	81	0,146447	-0,04561	113	0,853553	-0,004314
18	0,835779	0,029347	50	0,129524	0,043071	82	0,164221	-0,047773	114	0,870476	-0,002829
19	0,817197	0,032176	51	0,113495	0,040585	83	0,182803	-0,049805	115	0,886505	-0,001592
20	0,79785	0,035017	52	0,098396	0,038011	84	0,20215	-0,051694	116	0,901604	-0,0006
21	0,777785	0,037847	53	0,084265	0,03536	85	0,222215	-0,053427	117	0,915735	0,000157
22	0,757051	0,040641	54	0,071136	0,032644	86	0,242949	-0,054994	118	0,928864	0,000694
23	0,735698	0,043377	55	0,059039	0,029874	87	0,264302	-0,056376	119	0,940961	0,001033
24	0,713778	0,046029	56	0,048005	0,027062	88	0,286222	-0,057547	120	0,951995	0,001197
25	0,691342	0,048575	57	0,03806	0,024219	89	0,308658	-0,058459	121	0,96194	0,001212
26	0,668445	0,050993	58	0,029228	0,021348	90	0,331555	-0,059046	122	0,970772	0,001112
27	0,645142	0,053258	59	0,02153	0,018441	91	0,354858	-0,059236	123	0,97847	0,000935
28	0,62149	0,055344	60	0,014984	0,015489	92	0,37851	-0,058974	124	0,985016	0,000719
29	0,597545	0,057218	61	0,009607	0,01248	93	0,402455	-0,058224	125	0,990393	0,000497
30	0,573365	0,058845	62	0,005412	0,009416	94	0,426635	-0,056979	126	0,994588	0,000296
31	0,549009	0,060194	63	0,002408	0,006306	95	0,450991	-0,055257	127	0,997592	0,000137
32	0,524534	0,061254	64	0,000602	0,003165	96	0,475466	-0,053099	128	0,999398	0,000035

C. NACA0012 Airfoil Cordinates:

Table 22.NACA0012 Airfoil Cordinates.

#	X (mm)	Y (mm)	#	x (mm)	Y (mm)	#	X (mm)	Y (mm)	#	X (mm)	Y (mm)	#	X (mm)	Y (mm)
1	1000	0.000	41	654.508	40.686	81	95.492	46.049	121	95.492	-46.049	161	654.508	-40.686
2	999.753	0.036	42	639.496	42.052	82	86.460	44.374	122	104.922	-47.638	162	669.369	-39.300
3	999.013	0.143	43	624.345	43.394	83	77.836	42.615	123	114.743	-49.138	163	684.062	-37.896
4	997.781	0.322	44	609.072	44.708	84	69.629	40.776	124	124.944	-50.546	164	698.574	-36.478
5	996.057	0.572	45	593.691	45.992	85	61.847	38.859	125	135.516	-51.862	165	712.890	-35.048
6	993.844	0.891	46	578.217	47.242	86	54.497	36.867	126	146.447	-53.083	166	726.995	-33.610
7	991.144	1.280	47	562.667	48.455	87	47.586	34.803	127	157.726	-54.206	167	740.877	-32.168
8	987.958	1.737	48	547.054	49.626	88	41.123	32.671	128	169.344	-55.232	168	754.521	-30.723
9	984.292	2.260	49	531.395	50.754	89	35.112	30.473	129	181.288	-56.159	169	767.913	-29.279
10	980.147000	2.849	50	515.705	51.833	90	29.560	28.213	130	193.546	-56.986	170	781.042	-27.838
11	975.528000	3.501	51	500.000	52.862	91	24.472	25.893	131	206.107	-57.712	171	793.893	-26.405
12	970.440000	4.2160	52	484.295	53.835	92	19.853	23.517	132	218.958	-58.338	172	806.454	-24.981
13	964.888000	4.990	53	468.605	54.749	93	15.708	21.088	133	232.087	-58.863	173	818.712	-23.569
14	958.877000	5.822	54	452.946	55.602	94	12.042	18.607	134	245.479	-59.288	174	830.656	-22.173
15	952.414000	6.710	55	437.333	56.390	95	8.856	16.078	135	259.123	-59.614	175	842.274	-20.795
16	945.503000	7.651	56	421.783	57.108	96	6.156	13.503	136	273.005	-59.841	176	853.553	-19.438
17	938.153000	8.643	57	406.309	57.755	97	3.943	10.884	137	287.110	-59.971	177	864.484	-18.106
18	930.371	9.684	58	390.928	58.326	98	2.219	8.223	138	301.426	-60.006	178	875.056	-16.800
19	922.164	10.770	59	375.655	58.819	99	0.987	5.521	139	315.938	-59.947	179	885.257	-15.523
20	913.540	11.900	60	360.504	59.230	100	0.247	2.779	140	330.631	-59.797	180	895.0780	-14.280
21	904.508	13.071	61	345.492	59.557	101	0.000	0.000	141	345.492	-59.557	181	904.508	-13.071
22	895.078	14.280	62	330.631	59.797	102	0.247	-2.779	142	360.504	-59.230	182	913.540	-11.900
23	885.257	15.523	63	315.938	59.947	103	0.987	-5.521	143	375.655	-58.819	183	922.164	-10.770
24	875.056	16.800	64	301.426	60.006	104	2.219	-8.223	144	390.928	-58.326	184	930.371	-9.684
25	864.484	18.106	65	287.110	59.971	105	3.943	-10.884	145	406.309	-57.755	185	938.153	-8.643
26	853.553	19.438	66	273.005	59.841	106	6.156	-13.503	146	421.783	-57.108	186	945.503	-7.651
27	842.274	20.795	67	259.123	59.614	107	8.856	-16.078	147	437.333	-56.390	187	952.414000	-6.710
28	830.656	22.173	68	245.479	59.288	108	12.042	-18.607	148	452.946	-55.602	188	958.877	-5.822
29	818.712	23.569	69	232.087	58.863	109	15.708	-21.088	149	468.605	-54.749	189	964.8880	-4.990
30	806.454	24.981	70	218.958	58.338	110	19.853	-23.517	150	484.295	-53.835	190	970.4400	-4.216
31	793.893	26.405	71	206.107	57.712	111	24.472	-25.893	151	500.000	-52.862	191	975.5280	-3.5010
32	781.042	27.838	72	193.546	56.986	112	29.560	-28.213	152	515.705	-51.833	192	980.147	-2.8490
33	767.913	29.279	73	181.288	56.159	113	35.112	-30.473	153	531.395	-50.754	193	984.292	-2.260
34	754.521	30.723	74	169.344	55.232	114	41.123	-32.671	154	547.054	-49.626	194	987.958	-1.737
35	740.877	32.168	75	157.726	54.206	115	47.586	-34.803	155	562.667	-48.455	195	991.144	-1.280
36	726.995	33.610	76	146.447	53.083	116	54.497	-36.867	156	578.217	-47.242	196	993.844	-0.891
37	712.890	35.048	77	135.516	51.862	117	61.847	-38.859	157	593.691	-45.992	197	996.057	-0.572
38	698.574	36.478	78	124.944	50.546	118	69.629	-40.776	158	609.072	-44.708	198	997.781	-0.322
39	684.062	37.896	79	114.743	49.138	119	77.836	-42.615	159	624.345	-43.394	199	999.013	-0.143
40	669.369	39.30	80	104.922	47.638	120	86.460	-44.374	160	639.496000	-42.052	200	999.753	-0.036

References

[1] https://murtiedjokobayu.medium.com/devices-mounted-on-wings-what-are-they-26c6534aef56

[2] Yu, Cunming, et al. "Bio-inspired drag reduction: from nature organisms to artificial functional surfaces." *Giant* 2 (**2020**): 100017.

[3] Baals, Donald D. *Wind tunnels of NASA*. Vol. 440. Scientific and Technical Information Branch, National Aeronautics and Space Administration, **1981**.

[4] Paula, Adson Agrico de. *The airfoil thickness effects on wavy leading edge phenomena at low Reynolds number regime*. Diss. Universidade de São Paulo, **2016**.

[5] Lee, John D. *Boundary Layers on Airfoils in Transonic Flow and the Control of Shock-Induced Separation*. OHIO STATE UNIV RESEARCH FOUNDATION COLUMBUS, **1971**.

[6] Zohuri, B. (**2017**). Compressible Flow. In: Thermal-Hydraulic Analysis of Nuclear Reactors. Springer, Cham. https://doi.org/10.1007/978-3-319-53829-7_7

[7] https://www.aircraftsystemstech.com/2021/04/high-speed-aerodynamics-aircraft-theory.html

[8] *TF-8A Crusader* with *Supercritical Wing*. *Justin Murtha*, *John Stephens*,. *Mike Weronski*. NASA Conference Publication 3256

[9] Anderson, J. D., Jr. (**2000**). “Introduction to Flight,” 4th ed., McGraw-Hill, New York.

[10]https://www.centennialofflight.net/essay/Theories_of_Flight/Transonic_Wings/TH20G7.htm

[11] J.-P. Dussauge and S. Piponniau. Shock/boundary-layer interactions: Possible sources of unsteadiness. Journal of Fluids and Structures, 24:1166–1175, **2008**.

[12] Christopher S. Combs, Phillip A. Kreth, John D. Schmisseur and E. Lara Lash. Image-based analysis of shock-wave/boundary-layer interaction unsteadiness. AIAA Journal, 56(3):1288–1293, March **2018**.

[13] Kianoosh Yousefi, Reza Saleh, Peyman Zahedi. Numerical study of blowing and suction slot geometry optimization on NACA 0012 airfoil. Journal of Mechanical Science and Technology, 2014, 28 (4), pp.1297-1310. Ff10.1007/s12206-014-0119-1ff. ffhal-01590680f

[14] https://www.studyaircrafts.com/aircraft-control-surfaces.

[15] https://www.boldmethod.com/learn-to-fly/aerodynamics/how-adverse-yaw-affects-your-plane-during-a-roll-left-and-right/

[16] https://altairuniversity.com/44499-control-aircraft-pitch-angle-in-frequency-domain/

[17] Hawley, Arthur V. “Ten Years of Flight Service with DC-10 Composite Rudders — A Backward Glance.” *SAE Transactions*, vol. 95, 1986, pp. 678–85, http://www.jstor.org/stable/44470582. Accessed 12 May 2022.

[18] Hawley, Arthur V. "Ten years of flight service with DC-10 composite rudders—a backward glance." *SAE Transactions* (**1986**): 678-685.

[19] Understanding Secondary Control Surfaces. Flaps, Slats –Slots, SPOILERS, Balance Tabs & Trim Tabs, JxJ AVIATION, Apr 28, **2020.**

[20] - , "Aerodynamic Characteristics of Controls," AGARD C.P. No. 262, **1979**.

[21] https://www.boldmethod.com/learn-to-fly/aircraft-systems/spoilers/

[22] Spoiler - CFD-Wiki, the free CFD reference.

[23] https://www.boldmethod.com/learn-to-fly/aircraft-systems/leading-edge-slat-lift-device

[24] Zerihan, Jonathan, and Xin Zhang. "Aerodynamics of Gurney flaps on a wing in ground effect." *AIAA journal* 39.5 (**2001**): 772-780.

[25] https://skybrary.aero/articles/krueger-flaps

[26] STORMS, B.L., “Lift enhancement of an aerofoil using a gurney flaps and vortex generators”, J Aircr, 1994, 31, (3), PP 542-547.

[27] Frank K. Lu and Adam J. Pierce, January **2011** “Review of Micro Vortex Generators in High Speed flow”, 49th AIAA Aerospace Sciences meeting including the New Horizons forum and Aerospace Exposition.

[28] Caldwell, Frank W., and Elisha Noel Fales. *Wind tunnel studies in aerodynamic phenomena at high speed*. No. NACA-TR-83. **1921.**

[29] Fullmer, Felicien F. *Two-dimensional Wind-tunnel Investigation of the NACA 64 (sub 1)-012 Airfoil Equipped with Two Types of Leading-edge Flap*. No. NACA-TN-1277. **1947.**

[30] Sleeman Jr, William C., Paul L. Klevatt, and Edward L. Linsley. *Comparison of Transonic Characteristics of Lifting Wings from Experiments in a Small Slotted Tunnel and the Langley High-speed 7-by 10-foot Tunnel*. No. NACA-RM-L51F14. **1951.**

[31] Ladson, Charles L., and S. Acquilla Hill. *High Reynolds number transonic tests on a NACA 0012 airfoil in the Langley 0.3-meter transonic cryogenic tunnel*. No. NASA-TM-100527. **1987.**

[32] Anderson Jr, John D. "Research in Supersonic Flight and the Breaking of the Sound Barrier--Chapter 3." *history. nasa. gov*: 65.

[33] Bryan, G. H. "The Effect of Compressibility on Stream Line Motions. R. & M. No. 555." *British ACA* (**1918**).

[34] Mathews, Charles W., and Jim Rogers Thompson. *Drag Measurements at Transonic Speeds of NACA 65-009 Airfoils Mounted on a Freely Falling Body to Determine the Effects of Sweepback and Aspect Ratio*. No. NACA-RM-L6K08c. **1947**.

[35] Chapman, Dean R., Donald M. Kuehn, and Howard K. Larson. *Investigation of separated flows in supersonic and subsonic streams with emphasis on the effect of transition*. No. NACA-TR-1356**. 1958.**

[36] Corrsin, Stanley. "Turbulent flow." *American Scientist* 49.3 (**1961**): 300-325.

[37] Tijdeman, Hendrik. "Investigations of the transonic flow around oscillating airfoils." *NLR-TR 77090 U* (**1977**).

[38] Rogallo, Robert S., and Parviz Moin. "Numerical simulation of turbulent flows." *Annual review of fluid mechanics* 16 (**1984**): 99-137.

[39] Raghunathan, S. "Passive control of shock-boundary layer interaction." *Progress in Aerospace Sciences* 25.3 (**1988**): 271-296.

[40] Stanewsky, E., Délery, J., Fulker, J., Geissler, W. (eds.): EUROSHOCK—Drag Reduction by Passive Shock Control. Results of the Project EUROSHOCK, AER2-CT92-0049, supported by the European Union, 1993–1995. Notes on Numerical Fluid Mechanics, Vol. 56. Vieweg, Braunschweig Wiesbaden (**1997**).

[41] Wells, Adam Joseph. *Experimental Investigation of an Airfoil with Co-Flow Jet Flow Control*. Diss. University of Florida, **2005**.

[42] High-Reynolds-Number Design of a Wing Section Including Control of Boundary Layer Properties K. Richter, S. Koch, H. Rosemann DLR AS-HK, Bunsenstr. 10, D-37073 Göttingen, Germany (**2006**).

[43] A Review on Active and Passive Flow Control Techniques April **2016**, Available @ http://www.ijrmee.org.

[44] Gorrell, Edgar S., and H. S. Martin. Aerofoils and aerofoil structural combinations. MS thesis. Massachusetts Institute of Technology, Dept. of Aeronautical Engineering, **1917**.

[45] Briggs, Lyman James, and Hugh L. Dryden. *Pressure distribution over airfoils at high speeds*. No. NACA-TR-255. **1927**.

[46] Hallion, Richard P. "The NACA, NASA, and the Supersonic-Hypersonic Frontier." *NASA's First* 50 (**2010**): 223-274.

[47] Furlong, G. Chester, and James E. Fitzpatrick. *Effects of mach number and reynolds number on the maximum lift coefficient of a wing of NACA 230-Series airfoil sections*. No. NACA-TN-1299. **1947**.

[48] McDevitt, John B. *A correlation by means of the transonic similarity rules of the experimentally determined characteristics of 22 rectangular wings of symmetrical profile*. No. NACA-RM-A51L17b. **1952**.

[49] Wood, N. J., and L. Roberts. "Control of vortical lift on delta wings by tangential leading-edge blowing." *Journal of Aircraft* 25.3 (**1988**): 236-243.

[50] Jacquin, Laurent, et al. "Experimental study of shock oscillation over a transonic supercritical profile." *AIAA journal* 47.9 (**2009**): **1985-1994**.

[51] Huang, JingBo, et al. "Simulation of shock wave buffet and its suppression on an OAT15A supercritical airfoil by IDDES." *Science China Physics, Mechanics and Astronomy* 55.2 (**2012**): 260-271.

[52] Jain, Shubham, Nekkanti Sitaram, and Sriram Krishnaswamy. "Effect of Reynolds number on aerodynamics of airfoil with Gurney flap." *International Journal of Rotating Machinery* 2015 (**2015**).

[53] Kumar, K. Harish, C. K. Kumar, and T. Naveen Kumar. "Cfd analysis of rae 2822 supercritical airfoil at transonic mach speeds." *International Journal of Research in Engineering and Technology* 4.9 (**2015**): 256-262.

[54] Sohail, Muhammad Umer, and Asad Islam. "Verification and validation of flow over a 3D ONERA wing using CFD approach." *Journal of Space Technology* 7.1 (**2017**).

[55] Koti, Dhruva, and A. Khan. "Numerical Analysis of Transonic Airfoil." *International Journal of Engineering Research & Technology (IJERT) ISSN*: 2278-0181.

[56] Cook, P.H., M.A. McDonald, M.C.P. Firmin, Aerofoil RAE 2822-Pressure Distributions, and Boundary Layer and Wake Measurements, Experimental Data Base for Computer Program Assessment, AGARD Report AR 138, (**1979**).

[57] Valentin Bonnifet. Prédiction du phénomène de tremblement sur un profil d'aile avec une approche LES de type PANS-RSM. Mécanique des fluides [physics.class-ph]. Sorbonne Université, **2018**. Français. ffNNT : 2018SORUS389ff. fftel-02612234v2.

[58] Gerolymos, G. A., and Vallet, I. Influence of temporal integration and spatial discretization on hybrid rsm–les computations. In 18th AIAA Computational Fluid Dynamics Conference (**2007**), no. 4094, AIAA, pp. 1–18

[59] Gerolymos, G. A., Lo, C., Vallet, I., and Younis, B. A. Term-by-term Analysis of Near-Wall Second-Moment Closures. AIAA J. 50, 12 (Dec. **2012**), 2848–2864.

[60] Girimaji, S. S., Jeong, E. J., and Srinivasan, R. Partially Averaged Navier-Stokes Method for Turbulence: Fixed Point Analysis and Comparison With Unsteady Partially Averaged Navier-Stokes. J. Appl. Mech. 73, 3 (**2006**), 422–429.

[61] Eftekhari S, Al-Obaidi ASM (**2019**) Investigation of a NACA0012 Finite Wing Aerodynamics at Low Reynold's Numbers and 0° to 90° Angle of Attack. J Aerosp Technol Manag, 11: e1519. https://doi.org/10.5028/jatm.v11.1023.

[62] Aggarwal, Arpit, et al. "Steady-State Flow Solutions for Delta Wing Configurations at High Angle of Attack Using Implicit Schemes." *STAB/DGLR Symposium*. Springer, Cham, **2020**.

[63] Wang, Y.; Liu, D.; Xu, X.; Li, G. Investigation of Reynolds Number Effects on Aerodynamic Characteristics of a Transport Aircraft. Aerospace **2021**, 8, 177. https:// doi.org/10.3390/aerospace8070177.

[64] Vinayaka, N., et al. "Study of Supercritical Airfoil Aerodynamics at various Turbulence Intensities and Mach Numbers in Transonic Regime." *High Technology Letters* 27.8 (**2021**): 1-11.

[65] Han, Bing, et al. "Numerical investigation of transonic buffet on a prescribed-pitching OAT15A airfoil." *AIP Advances* 12.3 (**2022**): 035301.

[66] Prandtl, Ludwig. Theory of lifting surfaces. No. NACA-TN-10-Pt-2. **1920**.

[67] Racisz, Stanley F. Investigation of NACA 65 (112) A111 (approx.) Airfoil with 0.35-chord Slotted Flap at Reynolds Numbers up to 25 Million. No. NACA-TN-1463. **1947**.

[68] Erickson, Albert L Stephenson, Jack D; A suggested method of analyzing for transonic flutter of control surfaces based on available experimental evidence; naca-rm-a7f30; December 16, **1947.**

[69] Strass, H. Kurt. *The Effect of Spanwise Aileron Location on the Rolling Effectiveness of Wings with 0 Degree and 45 Degree Sweep at Subsonic, Transonic, and Supersonic Speeds*. No. NACA-RM-L50A27. **1950**.

[70] Wood, George P. *Experiments on Transonic Flow Around Wedges*. NATIONAL AERONAUTICS AND SPACE ADMINISTRATION HAMPTON VA LANGLEY RESEARCH CENTER, **1952**.

[71] Lovell, D. A. *A wind-tunnel investigation of the effects of flap span and deflection angle, wing planform and a body on the high-lift performance of a 28° swept wing*. HM Stationery Office, **1977**.

[72] Consigny, H., A. Gravelle, and R. Molinaro. "Aerodynamic characteristics of a two-dimensional moving spoiler in subsonic and transonic flow." *Journal of Aircraft* 21.9 (**1984**): 687-693.

[73] Storms, Bruce L., and Cory S. Jang. "Lift enhancement of an airfoil using a Gurney flap and vortex generators." Journal of Aircraft 31.3 (**1994**): 542-547.

[74] Jeffrey D, Zhang X, Hurst DW. Aerodynamics of Gurney flaps on a single-element high-lift wing, AIAA J. Aircraft **2000**; 37(2):295–301.

[75] Heller, G., P. Kreuzer, and S. Dirmeier. "Development and integration of a new high performance wingtip device for transonic aircraft." Proceedings of the ICAS 2002 Congress, Toronto, ON, Canada. **2002**.

[76] Fillola, Guillaume. *Étude expérimentale et simulations numériques d'écoulements autour des surfaces mobiles de voilure*. Diss. Toulouse, ENSAE, **2006**.

[77] Ragheb, Adam, and Michael Selig. "Multi-element airfoil configurations for wind turbines." *29th AIAA Applied aerodynamics conference*. **2011**.

[78] Hossain, Md Amzad, Mohammad Mashud, and Khondakar Wahida Taskin. "Effect of spoiler angle on aerodynamic characteristics of an airfoil." (**2014**).

[79] Leong, Chia Min, et al. "Interactions of a dynamic vortex generator with a cross-flow: An experimental study." *45th AIAA Fluid Dynamics Conference*. **2015**.

[80] Cummings, Reed, Dan Clingman, and Onkar Sahni. "Interactions of a dynamic vortex generator with a cross-flow: A numerical study." *45th AIAA Fluid Dynamics Conference*. **2015**.

[81] Rice, Thomas, et al. "Experimental and numerical investigation of static and dynamic vortex generators on an airfoil with a deflected flap." *8th AIAA Flow Control Conference*. **2016**.

[82] Xiong, Juntao, Nhan T. Nguyen, and Robert E. Bartels. "Aerodynamic Optimization of Mach 0.8 Transonic Truss-Braced Wing Aircraft Using Variable Camber Continuous Trailing Edge Flap." *AIAA SCITECH 2022 Forum*. **2022**.

[83] Mayergoyz, Isaak D., and Patrick McAvoy. *Fundamentals of Electric Power Engineering*. World Scientific, **2014**.

[84] Richardson, Lewis Fry. *Weather prediction by numerical process*. Cambridge university press, **2007**.

[85] Poradowski, W. "Turbulence modeling introduction to ANSYS Fluent." **(2020).**

[86] FLUENT 12.0: Theory Guide. ANSYS, inc, **2009**.

[87] M. Heniche, P. A. Tanguy «A New Element-by-Element Method for Trajectory Calculations with Tetrahedral Finite Element Meshes". International Journal for Numerical Methods in Engineering, 67(9), pp. 1290-1317, **2006**.

[88] Salim, Salim Mohamed, and AMIMechE BEng. *Computational study of wind flow and pollutant dispersion near tree canopies*. Diss. University of Nottingham, **2011**.

[89] S.V. Patankar "Numerical heat transfer and fluid flow". Hemisphere publishing corporation, États-Unis d'Amérique, **1980**.

[90] Fluent, A. N. S. Y. S. "ANSYS Fluent 12.0 user's guide." *Ansys Inc* 15317 (**2009**): 1-2498.

[91] Airfoil - CFD-Wiki, the free CFD reference.

[92] Introductory Fluid Mechanics L21 p5-Lift Force-Youtube- Ron Hugo, 11 Aug **2015.**

[93] https://www.esa.int/ESA_Multimedia/images/2002/09/Dynamic_Lift_Pressure_distribution.

[94] Liang, Y. Bin, et al. "Design considerations of rotor configuration for straight-bladed vertical axis wind turbines." *Advances in Mechanical Engineering* 6 (**2014**).

[95] https://www.quora.com/What-is-the-main-purpose-of-an-aircrafts-wings-How-many-types-of-wings-are-there

[96] Hamel, Peter G., and Ravindra V. Jategaonkar. "Evolution of flight vehicle system identification." *Journal of aircraft* 33.1 (**1996**): 9-28.

[97] Jenkins et al., NASA SC (2)-07 14 Airfoil Data Corrected for Sidewall Boundary-Layer Effects in the Langley 0.3-Meter Transonic Cryogenic Tunnel,**1989**.

[98] Ravikumar T et al., Aerodynamic analysis of supercritical NACA sc (2)-0714 airfoil using CFD, IJATES.

[99] Michael Iovnovich et al., Shock-buffet Instability of 3D Wings, Technion, IIT **2013**.

[100] Santiago Giraldo, Manuel J. Garcia, Pierre Boulanger - "CFD Based Wing Shape Optimization Through Gradient-Based Method " EAFIT University, No 7 Sur 50, Medellin, Colombia University Of Alberta, 2-21 Athabasca Hall, T6G 2E8, Canada.

[101] Halliday, David, Resnich, Robert - "How do wings work".

[102] Harris, C.D.: Two-dimensional aerodynamic characteristics of the NACA0012 airfoil. In the Langley 8-foot transonic pressure tunnel. NASA Technical Memorandum 81927 (**1981**).

[103] Beck, Paulo Arthur. "Análise metodológica de simulações de escoamentos turbulentos sobre seções de perfis aerodinâmicos." (**2010**).

[104] Ahn, Jaekwon, et al. "Response surface method for airfoil design in transonic flow." *Journal of aircraft* 38.2 (2001): 231-238.

[105] Choi, Seong-Wook, Keun-Shik Chang, and Honam Ok. "Parametric study of transient spoiler aerodynamics with two-equation turbulence models." *Journal of aircraft* 38.5 (2001): 888-894.

[106] Schmitt, V. and F. Charpin, "Pressure Distributions on the ONERA-M6-Wing at Transonic Mach Numbers," *Experimental Data Base for Computer Program Assessment.* Report of the Fluid Dynamics Panel Working Group 04, AGARD AR 138, May **1979**.

[107] Fatchurrohman, N., and S. T. Chia. "Performance of hybrid nano-micro reinforced mg metal matrix composites brake calliper: simulation approach." *IOP Conference Series: Materials Science and Engineering*. Vol. 257. No. 1. IOP Publishing, 2017.

[108] Barbut, Guillaume, et al. "Prédiction du tremblement transsonique autour d'une aile avec aileron par modélisation de la turbulence hybride et statistique." *CFM 2009-19ème Congrès Français de Mécanique*. AFM, Maison de la Mécanique, 39/41 rue Louis Blanc-92400 Courbevoie, 2009